Determination of Optical Scattering Properties of Tissues Using Reflectance-mode Confocal Microscopy

Ravikant, Samatham Venkata

Dissertation

Presented to the Department of Biomedical Engineering
and the Oregon Health & Science University
School of Medicine
in partial fulfillment of
the requirements for the degree of
Doctor of Philosophy
in
Biomedical Engineering

September 2012

Department of Biomedical Engineering
School of Medicine
Oregon Health & Science University

CERTIFICATE OF APPROVAL

This is to certify that the Ph.D. dissertation of

Ravikant, Samatham Venkata

has been approved

Dr. Steven L. Jacques, Thesis Advisor
Professor, Departments of Dermatology and Biomedical Engineering,
Oregon Health & Science University

Dr. Monica T. Hinds, Committee Chair
Associate Professor, Department of Biomedical Engineering,
Oregon Health & Science University

Dr. Sandra Rugonyi
Associate Professor, Department of Biomedical Engineering,
Oregon Health & Science University

Dr. Donald D. Duncan
Professor, Department of Electrical and Computer Engineering,
Portland State University

Dr. Philippe Thuillier
Assistant Professor, Department of Public Health, and Preventive Medicine,
Oregon Health & Science University

Dedication

to my family
Father, Mother, Sister and Wife Haripriya.

and to my friends,
Subba Reddy, Kishore Kumar, Mallikarjuna, Seshu and others,
for their unwavering support

Contents

List of Figures

8.5 The effect of tissue variation on analysis. (A) Experimental data, showing the scattering coefficient, $\mu_s[cm^{-1}]$, anisotropy of scattering, g [dimensionless], and the reduced scattering coefficient, $\mu_s(1-g)[cm^{-1}]$, plotted versus the reflectivity ρ. The mutant (red squares) and oim data (blue circles) were sampled from figure 8.4. The central black circle in each data set is the approximate peak of distributed data. (B) Simulated data centered around the same peaks in the data but with random ± 40 % variation introduced into the function $\log[R(z)]$ prior to analysis, to simulate the fluctuation in optical density of the skin. The spread of the simulated and experimental data is similar, suggesting that the apparent coordinate variation in the μ and ρ data in figure 8.4 is the expected response to local fluctuations in the optical density of the tissue. 121

List of Tables

List of Abbreviations and Symbols

Δz	Axial resolution of confocal system
λ	Wavelength
μ	Attenuation
μ_a	Absorption coefficient
μ_s	Scattering coefficient
μ_s'	Reduced scattering coefficient
ρ	Reflectivity
$a(g)$	Scattering efficiency factor: determines ability of photon to reach the focus despite scattering
$b(g, NA)$	Scatter collection efficiency: fraction of light backscattered into the NA of the objective lens
g	Anisotropy of scattering
$G(g, NA)$	Pathlength augmentation factor: describes the factor that augments the average pathlength of photon
mfp	Mean free path
n	Refractive index
$p(\theta)$	Scattering phase function
R_{ph}	Radius of the pinhole
V_{wg}	Signal from water-glass interface
CM	Confocal microscopy
derm	Dermis

DMSO	Dimethyl sulphoxide
epi	Epidermis
FL	Focal length
GFP	Green fluorescent protein
HeNe	Helium-Neon laser
HG	Henyey-Greenstein scattering phase function
MC	Monte Carlo
NA	Numerical aperture of a objective lens; measures its ability to gather light and resolve sample details.
OCA	Optical clearing agent
OCM	Optical coherence microscopy
OCT	Optical coherence tomography
oim or OI	Osteogenesis imperfecta
PBS	Phosphate buffered saline
PDT	Photodynamic therapy
PMT	Photo-multiplier tubes
rCSLM	Reflectance-mode confocal Scanning laser microscopy
sc	Stratum corneum

ACKNOWLEDGEMENTS

I would like to express my gratitude to so many people who have encouraged and supported through this endeavor. First, I like to thank my advisor Dr. Steven Jacques for his support and guidance. He taught me how to focus on minute details while not losing sight of the big picture, when conducting research. As his student, I learned many lessons that will guide my future. I learned how to communicate my ideas clearly and effectively. In his laboratory, I had the unique opportunity to work in variety of projects that enriched my understanding of many subjects of biomedical engineering.

I like to thank the biomedical optics faculty for their guidance and feedback over the years. I like to thank Dr. Scott Prahl for his suggestions in the optics group talks. I like to thank Dr. Don Duncan for being in my thesis committee. His comments and suggestions were invaluable in making this dissertation what it is. I like to thank Dr. Sean Kirkpatrick and Dr. Ricky Wang for their feedback and their guidance. I like to thank my thesis advisory committee members: Dr. Monica Hinds, Dr. Sandra Rugonyi and Dr. Phillippe Thuillier for their guidance. Last but not the least, I have to thank graduate student director of the Biomedical Engineering Department, Dr. Owen McCarthy, and coordinator, Janet Itami, for guiding me through the graduation process.

I like to thank my friends and colleagues, who made my life as a graduate student bearable and fun. I could not keep my sanity without their support and encouragement. I like thank past and present members of Jacques' lab: Niloy Choudhury, David Levitz, Yongji Fu, and Kevin Phillips. Niloy Choudhury is a good friend and a mentor. I would like to especially thank Kevin Phillips. I

would not have completed this thesis without his help. I worked with David Levitz and Yongji Fu in calibration of confocal system used for this dissertation work. I would like to also thank my classmates in the biomedical optics program: Elaine, Amanda, and Jimmy. I was able to survive the graduate school only with the support and company of my friends.

I like to thank Dr. Molly Kulesz-Martin and Dr. Missy Wong at the Dermatology Research Lab for their feedback in the Dermatology Lab meetings. I appreciate the opportunity to be present and attend those meetings. Trevor and Aaron are good friends and without their help, chapter 6 and chapter 7 of this thesis would not have been possible. I had an opportunity to work with many more people that I am not able to thank individually. I like to express my sincere gratitude to everyone.

Lastly, I would not have reached this point in my life without the love, support, and guidance of my family and my friends Subba Reddy, Kishore Kumar, Malli, Seshu and many more. I am lucky to have them in my life.

ABSTRACT

Optical techniques represent a non-invasive strategy to monitor normal and pathological tissue function in both diagnostic and therapeutic applications. Central to the utility of optical methods in medicine is the determination of how light propagates in tissues. This requires a knowledge of light-tissue interactions which are determined by scattering and absorption. Scattering is dependent on the nanoscale organization of the tissue: given by the size, shape and density of the tissue constituents. Scattering is quantified by two properties: the number of scattering events encountered by photons per unit distance, termed the scattering coefficient, denoted μ_s $[cm^{-1}]$; and the cosine of the average scattering angle during each scattering event, termed the anisotropy factor, denoted g $[dimensionless]$.

For a fixed wavelength of light, the μ_s is sensitive to both the density, shape and size of the constituents of the tissue, while the g is most sensitive to constituent size. A complete knowledge of tissue structure requires the simultaneous knowledge of both these optical properties. Unfortunately, current techniques available to measure the scattering properties of a tissue report a quantity that couples these parameters, termed the reduced scattering coefficient, denoted $\mu_s\prime$ and equal to $\mu_s(1-g)$. Hence, constituent size and density of a tissue cannot be inferred through such measurements.

This thesis presents a technique to simultaneously estimate the scattering coefficient and anisotropy of tissues using a reflectance-mode confocal scanning laser microscope (rCSLM). The rCSLM signal is fit to a two parameter decaying exponential to yield two empirically fit parameters: the attenuation $\mu[cm^{-1}]$, and reflectivity $\rho[-]$. A theoretical model was developed to map these empirical fit

parameters to the optical properties of the scattering media: μ_s and g.

This model was validated on microsphere suspensions, whose optical properties are calculable from first principles using well established electromagnetic scattering calculations, known as Mie theory. Variable concentrations and sizes of microspheres were tested. The optical properties of the sphere suspensions determined from the rCSLM data were found to agree with the corresponding Mie theoretic values. The model is used to estimate optical properties of different types of mouse tissue.

Next, to demonstrate the utility of the technique, the optical clearing effect in dermal tissue was investigated. Optical clearing consists of exposing tissues to chemical agents, such as glycerin, that make tissues appear semi-transparent. Whether the increased transparency is due to increases in scattering anisotropy or a reduction in the scattering coefficient has been ill-defined. Our simultaneous measurement of both the scattering coefficient and anisotropy factor using rCSLM data revealed that glycerin significantly increased the g of the dermis from 0.7 to 0.99, with little change in μ_s of the dermis. These results indicate that glycerin increases the size of the scattering constituents in the dermis resulting in increased transparency of the tissue.

Lastly, the method was employed in a pilot study to characterize the structural consequences of *osteogenesis imperfecta* (oim), a genetic disorder that affects the ability of collagen fibers to organize into fiber bundles within the dermis. Mice with and without the oim mutation were investigated. The scattering anisotropy g decreased from 0.81±0.1 in wild type mice to 0.46±0.2 in mice with the mutation. The scattering coefficient was determined to be 70±20 cm^{-1} in wild type mice and 90±30 cm^{-1} in oim mutated mice. The decrease in g, provides an optically derived indication of the failure of the mutant collagen fibrils to assemble into larger collagen fiber bundles present in the dermis of wild type mice. While preliminary,

these results demonstrate the potential of the rCSLM based method to identify structural changes in tissues due to pathological conditions.

Together, these studies indicate the unique utility of rCSLM to perform non-invasive measurements of tissue structure through the simultaneous measurement of the scattering coefficient and scattering anisotropy factor using the model presented in this thesis. Development of pathology in tissues is associated with structural changes that can be monitored non-invasively by tracking the changes in optical properties of tissue.

Chapter 1

Introduction

The ability of light to penetrate into and out of tissue allows optical methods to both interrogate tissues for diagnostic purposes and to deliver energy for therapeutic or surgical purposes. Therefore, both diagnostics and therapy depend on light penetration into a tissue. However, penetration of light into tissue depends on optical properties of tissue (chapter 2), which determine the propagation and deposition of light energy in tissue.

This dissertation presents a novel noninvasive experimental method and the associated theoretical analysis for specifying the optical scattering properties of biological tissues. Such information enables noninvasive monitoring of changes in the nanoscale structure of cells and tissues.

A known optical method, reflectance-mode confocal scanning laser microscopy (rCSLM), was used to specify two optical scattering properties of a tissue,

- the scattering coefficient, μ_s $[cm^{-1}]$, and
- the anisotropy coefficient, g [dimensionless].

in a non-invasive manner on intact tissue. This method improves on current methods which either measure only the lumped parameter, reduced scattering coefficient $\mu'_s = \mu_s(1-g)$ $[cm^{-1}]$, or require excising tissue samples to prepare thin sections for measuring μ_s and g separately.

The motivation for separately measuring μ_s and g is to achieve a diagnostic characterization of tissue ultrastructure. The factor g in particular is sensitive to the size distribution of cellular and tissue structures, such as the nucleus, mitochondria, lysosomes, cytoskeleton, membranes, and extracellular fibers like collagen and actin-myosin filaments. Non-invasive measurements of g can follow changes in the nanoscale and microscale architecture of a tissue. Examples of such monitoring include:

1. Detecting subtle differences in the nanoarchitecture of mouse tissues (brain, skin, liver, muscle)

2. Detecting a single gene change in mouse skin, affecting collagen structure

3. Detecting the changes that yield optical clearing when mouse dermis is soaked in glycerin and is clarified

4. Detecting the nanoscale TiO_2 particulates in optical phantoms

5. Detecting the degradation of collagen fiber bundles by cellular Matrix metalloproteinase (MMP)

6. Detecting changes in structure of lymph node metastases of human breast cancer.

This thesis presents items 1-4 from the experiments conducted by the author. Others who used methods developed in our lab [3, 4] implemented item 5-6.

The author's role has been central to the development of this method. Gareau and Jacques built an rCSLM system and first developed the basic method of measuring μ_s and g separately, published in the Gareau *et al.* [1]. The optical system, electronics and the software, were rebuilt by the author, improving the performance of the rCSLM. The author conducted calibration experiments using polystyrene microspheres, which has been perhaps the most difficult aspect of this entire project.

The author conducted the first survey of mouse tissues optical properties using the method, and published the first paper on the method [5], describing the detection of changes due to a single gene change in mouse skin.

The method developed in this dissertation, is described briefly in the next section. Later the relevance of optical properties to characterize tissue is explored using Mie theory of light scattering from a sphere, where as a first approximation the tissue is represented by a distribution of spheres of different sizes.

The optical properties of scattering of a tissue, are specified by fitting the depth-dependent decay of the rCSLM signal with an exponential function given by equation 1.1(figure 1.1). The function is dependent on two parameters: attenuation (μ) and reflectivity (ρ) that correspond to slope and intercept of the natural log of the rCSLM signal (1.1). A model was developed to map these two fit parameters are mapped to optical scattering properties: scattering coefficient (μ_s) and scattering anisotropy (g). The model is described in chapter 3.

$$R(z) = \rho e^{-\mu z} \tag{1.1}$$

where $R(z)$ is the rCSLM signal as a function of depth (z), μ is attenuation and ρ is the reflectivity.

The theory is used to plot a grid of iso-μ_s and iso-g lines in the (μ, ρ) space (described in chapter 3). Figure 1.2A shows the grid with the red circle representing typical value of optical properties of mouse tissue (chapter 5). Figure 1.2B shows the inverse mapping of optical properties (μ_s, g) into fit parameters, (μ, ρ). The rectangle in figure 1.2B shows the typical range of the optical properties of tissues.

The model to map experimental parameters, (μ, ρ), to optical properties: (μ_s, g) was developed using Monte Carlo simulations of light transport of focused beam into tissue. The tissue is a complex structure comprised of various constituents

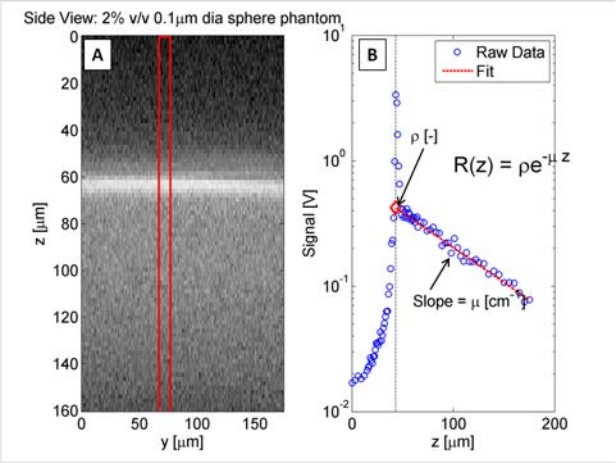

Figure 1.1: An example rCSLM image of the tissue phantom made with 0.1 μm diameter polystyrene spheres at 2% v/v concentration is plotted on a log scale. (A) Side view of the sphere phantom data as $\log_{10}$ of the signal (V) is displayed. (B) Shows the data from the red-box in (A) is displayed along with the result of the fitting the data with equation 1.1. The fit parameter ρ is the intercept of the fit at the surface of the sample represented by the maximum signal from the glass-sphere solution interface, and the μ is the slope the decaying exponential as a function of depth (z). This dissertation describes a model to map (μ, ρ) to scattering properties of the sample (μ_s, g).

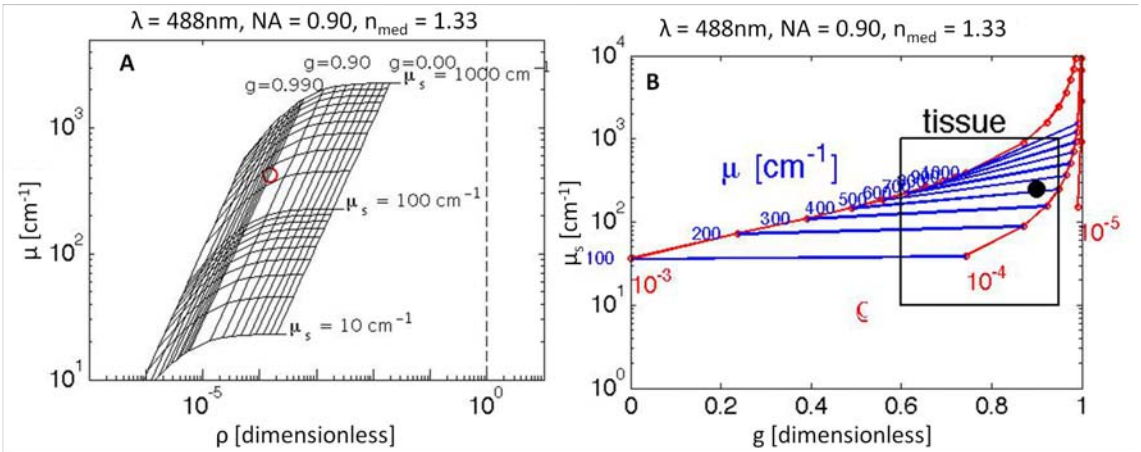

Figure 1.2: (A). The plot shows a representative analysis grid with the iso-μ_s lines and iso-g lines is plotted in the (μ, ρ) space. (B) The plot shows the inverse of (A), where a grid of iso-μ lines and iso-ρ lines are plotted in the (μ_s, g) space. The black rectangle in (B) represents the typical values for optical properties of mouse tissues.

like mitochondria, nuclei, and extra cellular matrix made of collagen, and elastin fibers. These constituents present various scales of scatterer sizes. The optical properties provide a fingerprint of the tissue ultrastructure that can be monitored by tracking changes in the optical properties.

Mie theory provides analytical solution to the scattering of light by spheres within a homogeneous background medium [6]. As a first-order approximation Mie scattering has been used to interpret scattering from tissue [7]. Tissue can be modeled as a collection of spheres of various sizes on the nm to μm size scale. The application of the Mie theory is only an approximate description that characterizes a tissue, but ignores the reality of the tissue architecture comprised of cells, cell organelles (mitochondria, nuclei), and extracellular matrix forming a complex structure. However, Mie theory provides a descriptive"fingerprint" for characterization of a tissue in terms of optical properties..

Figure 1.3A is a plot of the scattering coefficient (μ_s) and scattering anisotropy (g) calculated for range of sphere sizes and density. The scattering properties were calculated for each sphere size at different concentrations. The iso-density lines are presented in red color and the iso-diameter lines are presented in blue color. The black box in the plot presents the range of optical properties typically presented by tissues. Figure 1.3B shows the close-up of the region with the black box. The black dot in figure 1.3B represents an example of the optical properties of tissue with μ_s of 250 cm^{-1} (chapter 5) and a g of 0.9, which correspond to the sphere diameter of 430 nm and density of 2 μm^{-3}. The above grid can map the optical properties of tissues to a representative sphere size and concentration.

Tissue presents a complex structure of constituents of different sizes. In spite of the complex structure of the tissue, a distribution of spheres of different sizes, can provide a framework to interpret optical properties of tissues [7, 8] in terms their constituents (like mitochondria, nucleus and cell membranes). Representing

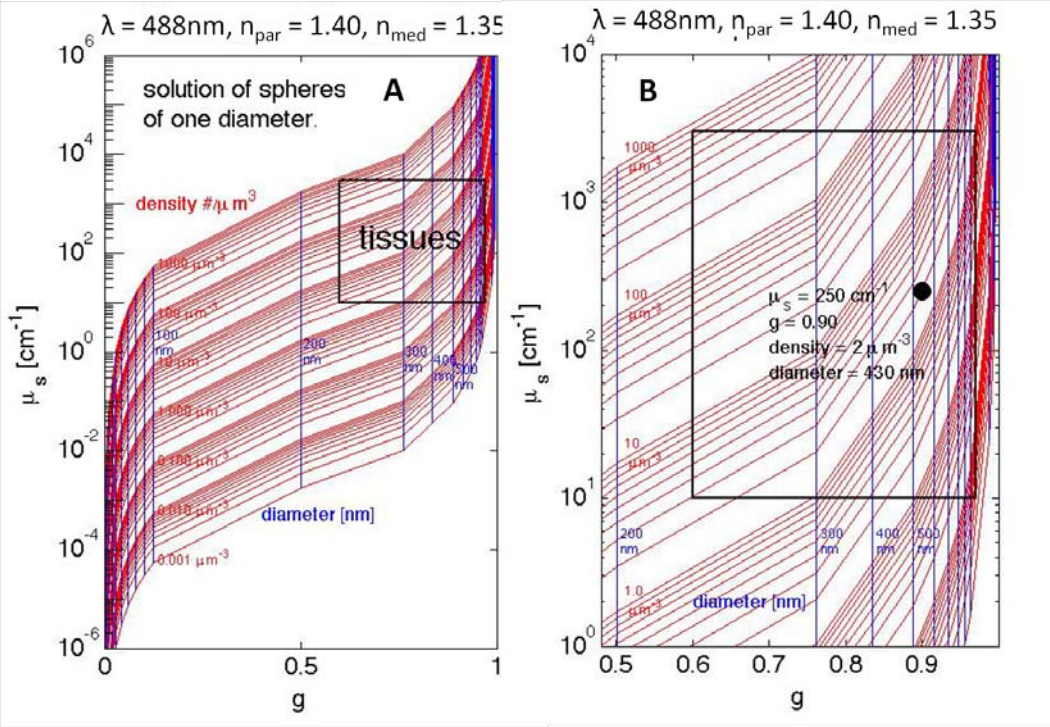

Figure 1.3: (A) plots the iso-density and iso-diameter lines for spheres in (μ_s, g) space. Mie theory was used to calculate μ_s and g for homogeneous samples made of single size spheres at different concentrations. Different size of spheres were used to generate the vertical blue lines. The typical range of μ_s and g values for tissue is represented by the black box in the plot. (B) shows the close-up of the region representing typical optical properties of tissues. Size of the sphere corresponding to $\mu_s = 250\ cm^{-1}$ and $g = 0.9$ is displayed which corresponds to a sphere size of 200 nm at a particle density of 2 μm^{-2} calculated by Mie theory. This plot shows that Mie theory can be used to represent optical properties of tissue in terms of size and number density of single spheres suspensions.

the tissue as collection of spheres is only an approximation, to provide a framework to relate optical properties measured from tissue to its constituents size using Mie theory. The tissue is represented by spheres with size distribution following a power law [9] given by (figure 1.4):

$$\eta(d) = A\left(\frac{d}{1nm}\right)^{-B} \tag{1.2}$$

where $\eta(d)$ is the probability density function for the size $d(nm)$ of particles. And

A is the normalization factor.

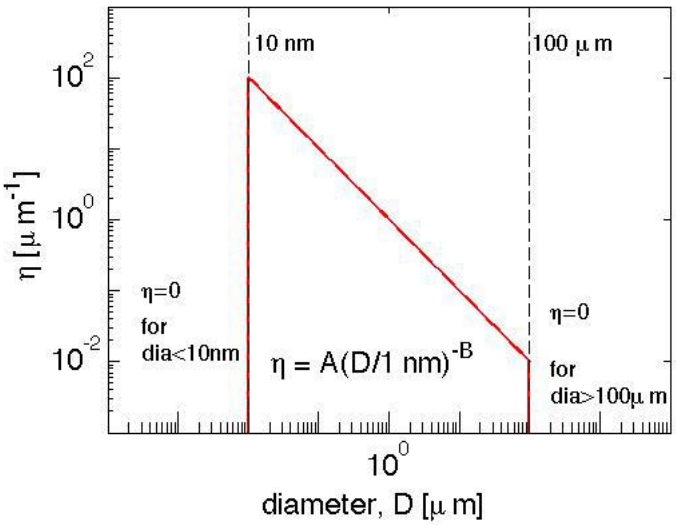

Figure 1.4: The plot shows the probability density function of the power law function that describes the size $d(nm)$ distribution of spheres used to model a tissue. The factor B specifies the shape of the distribution in terms of the exponent.

Factor B specifies the shape of the distribution. Change in the size distribution of the spheres manifests as the change in factor B. Figure 1.5A shows the optical properties μ_s and g for various values of factor B and volume fraction (vf) of spheres to background medium. Figure 1.5B shows the close-up of figure 1.5A, where the dotted lines represent a tissue with μ_s of 250 cm^{-1} and g of 0.9 for a volume fraction of spheres 0.3 with factor B equal to 4.55. Figure 1.5B shows that the change in B (size distribution) presents as the change in anisotropy (g) and change in the volume fraction of spheres presents as change in scattering coefficient (μ_s).

Mie theory describes the scattering of light by a sphere in homogeneous background medium. The above analysis is presented to illustrate that the Mie theory can be used to describe tissues modeled as distribution of spheres of different sizes. While this is only an approximate description of tissue, it can provide a frame-

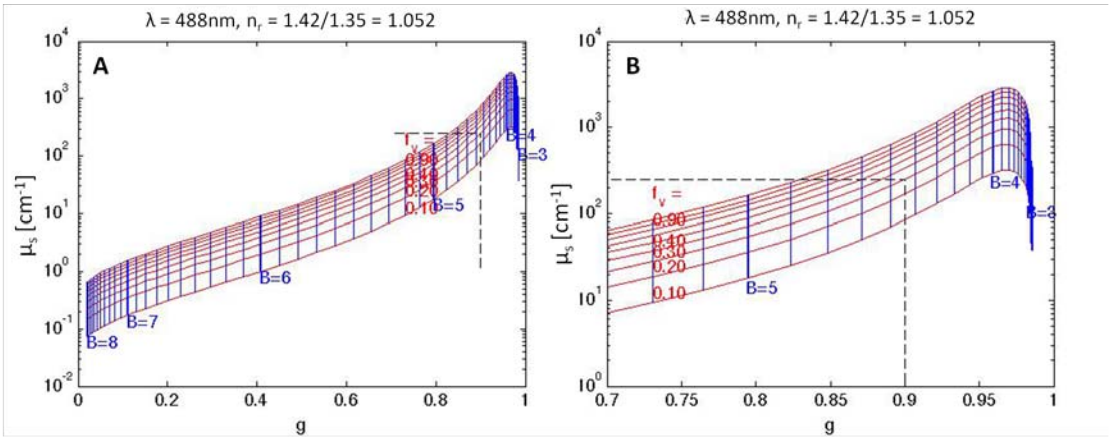

Figure 1.5: (A) plots the parameter B in equation 1.2 and volume fraction of the spheres in (μ_s, g) space. The iso-B lines are blue and the iso-volume fraction curves are red in color. (B) The plot shows the close up (A). The dotted lines show the location of a typical tissue with $\mu_s = 250\ cm^{-1}$ and $g = 0.9$. The map of iso-B lines and iso-volume fraction to estimate the size-distribution of spheres representing the tissue. The change in the size distribution affects the value parameter B which manifests as changes in g and μ_s. Even though tissue is a complex structure, the tissue can be modeled as a distribution of sphere sizes following power law and estimate the size distribution from optical properties using Mie theory.

work to interpret optical properties of tissues using Mie Theory. The change in the distribution of spheres (size and volume fraction) affects the optical scattering properties. The change in distribution of spheres as described can be related to changes in tissue composition due to pathology. Development of cancer in epithelial tissue is associated with increase in the size and number of nuclei that affects the size distribution of tissue constituents that can be monitored by changes in g and μ_s. Hence, optical properties of scattering: μ_s and g provides a fingerprint to the structure of the tissue. Estimation of the optical properties of scattering enables monitoring of changes in tissue ultrastructure for diagnostic proposes.

The significance of optical scattering properties to characterize tissue structure is described using Mie theory. To the first approximation the scattering properties can of the tissues can be described in terms of the distribution of spheres that act as a fingerprint to relate changes in optical properties to the structure of the tissue.

While tissues have complex structure, they can be approximately interpreted as a collection spheres of different sizes as described in this chapter, and the optical properties can be used to describe light-tissue interaction. Monte Carlo simulations were used to develop the theoretical model to estimate optical properties of tissues from rCSLM signal, that is presented in this thesis. A brief overview of the method to estimate the optical properties of tissues by fitting rCSLM signal was presented in this chapter. A background of tissue optics is the topic of next chapter (chapter 2). The optical properties of tissues and current methods used to measure optical properties is also presented. Confocal microscopy and a review of current literature on characterization of tissues using confocal signal is described.

Chapter 2

Background

There is growing interest in the extraction of quantitative information from optical measurements for biomedical applications [10–12]. Optical technologies provide multiple advantages as they are non-invasive, non-toxic and inexpensive [1, 13–15]. Biologists are interested in many parameters that include the assessment of the composition of the tissues. These parameters include the size, shape, and type of cells for diagnostic purposes [16–18] and the presence of chromophores in the tissue for therapeutic applications [19, 20]

Light-tissue interaction can be characterized either by empirical parameters [21, 22] or by optical properties of tissue [3, 5, 23]. Empirical parameters are dependent on the instrumentation and experimental parameters (which can be normalized). But, the optical properties are independent of instrumentation and experimental parameters and depend on the material. The optical properties of the tissue that affect light-tissue interactions are: scattering coefficient (μ_s), absorption coefficient (μ_a), scattering anisotropy (g), refractive index (n $[dimensionless]$) and reduced scattering coefficient (μ_s'). Characterizing tissue based on optical properties allows comparison of samples across multiple optical imaging technologies and multiple research groups, independent of instrumentation.

This chapter provides background information on the tissue optics. Definition of optical properties and the techniques to measure these optical properties is

presented here. The principle of confocal microscopy and the review of the current literature on the use of rCSLM to characterize tissue is presented.

Several optical techniques have been developed to determine optical properties: diffuse reflectance [24–27], oblique illumination [28, 29], and reflectance spectroscopy [30, 31]. These techniques were used to determine absorption coefficient, μ_a and reduced scattering coefficient, $\mu_s' = \mu_s(1-g)$. Where μ_s' is the lumped parameter used to describe light transport by diffusion theory. The absorption coefficient (μ_a) is a function of the chromophores in the tissue, which is used in various optical diagnostic and therapeutic application such as in photodynamic therapy (PDT) [32]. These optical properties are used in dosimetry, to determine the distribution of light energy in tissues for optical therapies involving diffuse light.

The reduced scattering coefficient (μ_s') describes scattering characteristics of the tissue. However, knowledge of the individual properties, μ_s and g can provide insight into tissue structure. The optical properties of scattering: scattering coefficient (μ_s) and scattering anisotropy (g) are dependent on the tissue ultrastructure i.e., size, shape and number density of the scatterers like nuclei, mitochondria, extracellular matrix and membrane proteins [33, 34]. Considering a fixed wavelength of irradiation, μ_s, is dependent on the size and number density of the scattering particles while g, is primarily dependent on the size of the particles relative to the wavelength of irradiation. Scattering anisotropy (g), encodes the average angular dependence of scattering while μ_s encodes the strength of scattering. Transition from dysplacia to carcinoma is associated with structural changes in the tissue that include: increased nucleus size, pleomorphism (changes in shape of nuclei), nuclear-to-cytoplasmic ratio, and decreased structural protein density. These changes alter the scattering properties of the tissue. Epithelial tissue scattering coefficients have been determined and used to differentiate normal versus cervical

cancer tissue [22, 35]. Optical properties of scattering provide an insight into the tissue morphology, which can be used for monitor pathological changes in tissue.

2.1 Tissue Optics

2.1.1 Light transport in Tissue

When light is propagating in tissue, it is either scattered or absorbed depending on the optical properties of the tissue. This dissertation describes the a technique to estimate optical scattering properties using reflectance-mode confocal scanning laser microscope (rCSLM) data. Optical properties are introduced and defined in this section. Common measurement techniques are discussed, while a detailed review can be found in Welch *et al.* [36]. The optical properties are defined in the following section.

2.1.2 Optical Properties

Determination of optical properties is necessary for the effective use of light energy in therapeutic and diagnostic applications. Among the many of such applications, PDT [19, 32], dosimetry [37, 38], and optical cancer diagnostics [39] are made possible or improved by the knowledge of the optical properties of tissue.

Depending on the characteristics of the scattering particle and incident photon, the light is scattered differently in different directions. The direction of scatter which guides the light transport in tissue depends on the scattering particle size, shape and the refractive index mismatch between the scattering particle and the surrounding medium. Along with scattering, light traveling through the tissue can be absorbed by chromophores in the tissue. Absorption by chromophores depends on the molecular structure of the chromophore and wavelength of the incident

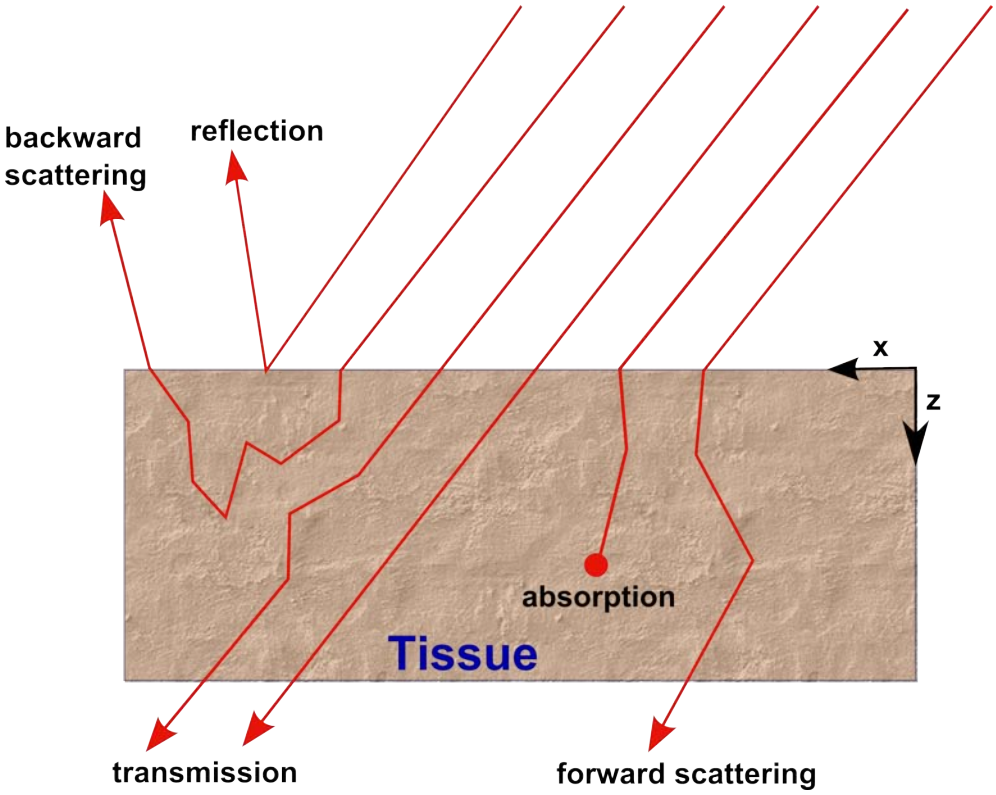

Figure 2.1: Interaction of light incident with a tissue. Light is absorbed by chromophores or scattered by tissue constituents. Light is scattered backward, forward or transmitted through depending on the scattering properties of the tissue. Fraction of light is specularly reflected from the surface.

light.

When light is incident on a tissue it is either reflected, transmitted, scattered or absorbed as shown in figure 2.1. Scattering is the change in the direction of light due to the interaction of light with the tissue. Reflection and transmission are scattering in backwards and forwards respectively. Scattering is caused by the local fluctuations of refractive index by various biological constituents in the tissue. Biological scattering particles in tissue include cells, organelles (mitochondria, nuclei, cell membranes) and extracellular matrix components like collagen fibers. Table 2.1 provides a summary of the optical properties.

The absorption coefficient (μ_a), describes the effectiveness of tissue structures

Table 2.1: Summary of tissue optical properties

Name	**Symbol**	**Units**	**Description**
Absorption Coefficient	μ_a	cm^{-1}	Absorption coefficient is defined as the number of absorption events per unit length. It is analogous to μ_s, but different phenomenon. Tissues are dominated by scattering, $\mu_s >> \mu_a$.
Scattering Coefficient	μ_s	cm^{-1}	The scattering coefficient is defined as the number of scattering events per unit length. It is the inverse of the average distance between scattering events. It is directly related to the density of the scatterers.
Scattering phase function	$p(\theta)$	-	Scattering phase function describes the angular dependence of scattering, can be interpreted as the probability density function defined along polar angles (θ). It is dependent on the relative size of the scattering particle and wavelength of light.
Anisotropy of scattering	g	-	Anisotropy of scattering is the forward component retained after the scattering event. It is defined as the expected value of the cosine of the polar angle of the scattered light, i.e., g = $\langle cos(\theta) \rangle$. g $\approx$ 1 for forward scattering, g = 0 for isotropic scattering and g $\approx$ -1 for backward scattering.

to absorb photons. Absorption coefficient is the inverse of the average distance between successive absorption events with units of inverse centimeters (cm^{-1}). The predominant chromophores in tissue are, hemoglobin, melanin, and bilirubin.

The scattering coefficient (μ_s), describes the effectiveness of the tissue structures to scatter photons. The scattering coefficient is the inverse of the average distance between successive scattering events, with units of units of inverse centimeters (cm^{-1}). The average distance between scattering events called the mean free path (mfp $[cm]$) is the inverse of scattering coefficient: $mfp = \frac{1}{\mu_s}$ $[cm]$.

When the photon is scattered, the energy is distributed in all directions, and it is not distributed uniformly as illustrated in figure 2.2. The angular dependence of scattering is called scattering phase function $p(\theta)$, that describes the probability of photon scattering into a unit solid angle relative to the original photon trajectory, with units of inverse steradians $[sr^{-1}]$. While light is scattered in all three-dimensions, the scattering phase functions describes the probability of scattering in polar deflection angle (θ), assuming uniform distribution in azimuthal angles. Scattering azimuthal angles is generally assumed symmetric. Light is scattered in a three-dimensional space (ψ). Turbid media have been shown to scatter non-uniformly in azimuthal direction. But, $p(\theta)$ is generally used to describe light transport in tissues assuming uniform distribution in azimuthal direction.

Figure 2.2, illustrates the concept of anisotropy (g) along with $p(\theta)$. Photons are deflected in different trajectories when scattered. The forward component of each of these trajectories is given by $cos(\theta)$. Anisotropy factor (g) [dimensionless] is defined as the mean value of the $cos(\theta)$ and this gives an average angle of deflection due to the scattering event. On average there is a deflection angle θ and the mean value of $cos(\theta)$ is defined as the anisotropy factor (g). It describes the amount of

forward scattering (red arrow in figure 2.2) retained after the scattering event.

$$g = \langle cos(\theta) \rangle = \int_0^{\pi} p(\theta) cos(\theta) 2\pi sin(\theta) d\theta \tag{2.1}$$

By definition, g varies between -1 (backward scattered) and 1 (forward scattered). Isotropic scattering deflects light into all possible directions with equal efficiency; this leads to $g = 0$.

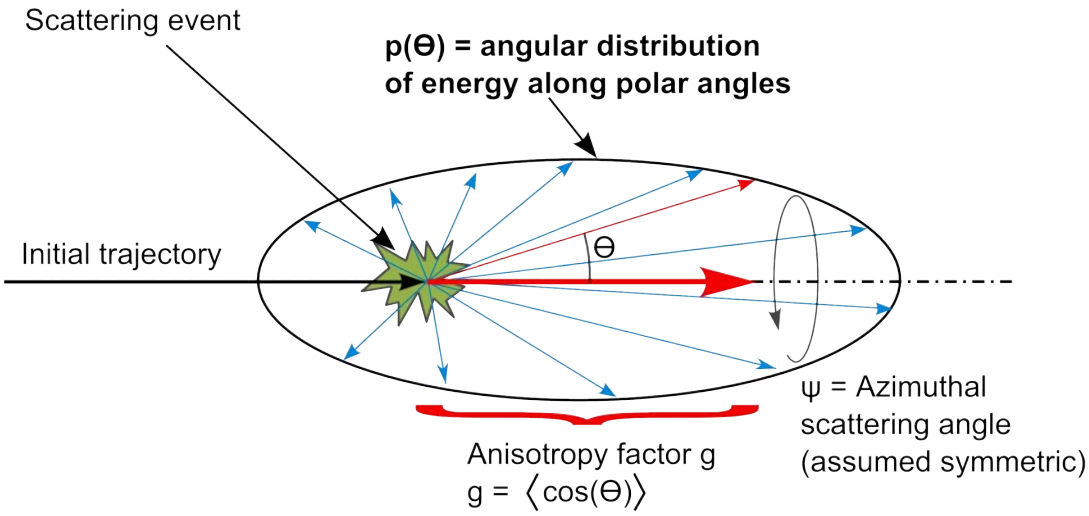

Figure 2.2: Scattering anisotropy factor, g, and scattering phase function, $p(\theta)$. Incident light (black) from the light undergoes scattering. The scattered light trajectories are represented by blue arrows and predominantly forward directed. An average forward component, defined anisotropy factor, g, is shown by a red arrow.

The scattering phase function is dependent on the size and shape of the particle relative to the wavelength of the photon, and the refractive index mismatch between the particle and the medium. Different scattering phase functions are described in the literature like the Mie theory [6], Henyey-Greenstein (HG) phase function [40, 41] and Multi-Gaussian [42]. There are analytical expressions to calculate $p(\theta)$ only for spheres and infinitely long cylinders developed by Gustav

Mie [6]. This is the Mie solution (referred to as Mie theory in the rest of the thesis) of Maxwell's equation that describes the scattering of electromagnetic radiation by a sphere in homogeneous background medium. According to Mie theory, spheres with diameter small compared to wavelength of light scatter isotropically with $g \approx 0$, where as larger spheres scatter forwards with $g \approx 1$.

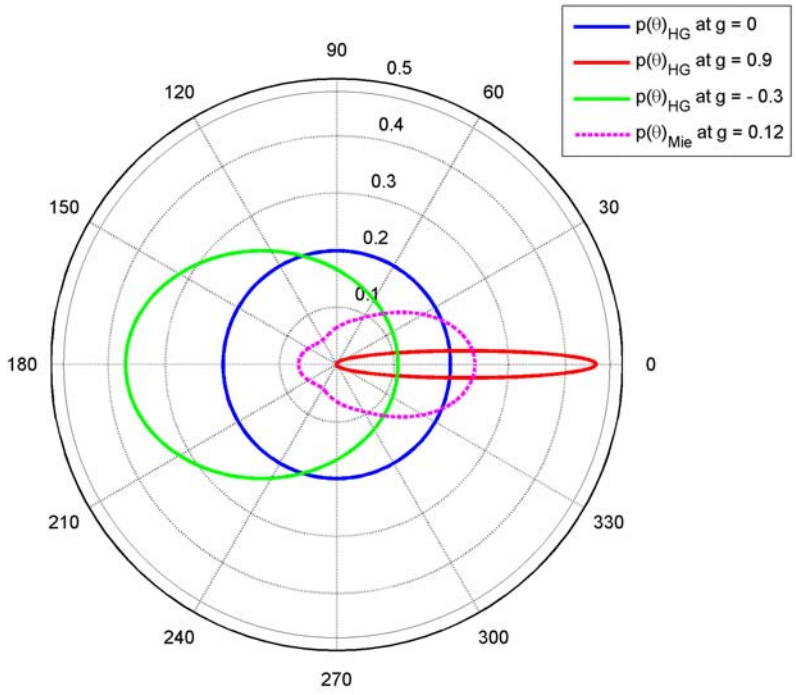

Figure 2.3: Henyey-Greenstein phase function ($p(\theta)_{HG}$ at different values of scattering anisotropy, g, and scattering phase function ($p(\theta)_{Mie}$) of spheres determined by Mie theory. While $p(\theta)_{HG}$ is smooth along the scattering angles, the $p(\theta)_{Mie}$ has a lobe.

However for tissues, the Henyey-Greenstein (HG) scattering phase function has proven to be useful in approximating the angular scattering dependence of single scattering events [40]. HG $p(\theta)$ is smooth, where as the presence of spherical harmonics and Bessel functions in the Mie solution, results in multiple lobes (figure 2.3). Figure 2.3 shows Henyey-Greenstein phase function calculated for

different values of g (g = 0, 0.9, -0.3). The figure also shows the phase function calculated by Mie theory for a sphere with $g = 0.12$.

The Henyey-Greenstein phase function is given by:

$$p_{HG}(\theta) = \frac{1}{4\pi} \frac{1 - g^2}{(1 + g^2 - 2gcos\theta)^{3/2}} \tag{2.2}$$

Figure 2.4 depicts different scattering regimes in the tissue. The most common regime is the diffusion regime that occurs at optical depth $\mu_s z \geq 10$, where large number of scattering events due to which the directionality of the scattering depicted in figure 2.3 is lost. Hence, it can be assumed that light diffuses down the concentration gradient of optical or radiant energy. In the diffusion regime, the scattering is characterized by a single lumped parameter, the reduced scattering coefficient, $\mu_s'[cm^{-1}]$, defined as $\mu_s' = \mu_s(1-g)$. So, as most of the indirect methods to determine optical properties use diffusion theory, the scattering coefficient (μ_s) and anisotropy (g) are lumped in μ_s', hence can be separated without additional information.

The single scattering regime ($\mu_s z \leq 1$) is assumed when the light enters the tissue and escapes after undergoing a single scattering event. The multiple scattering regime is somewhere between single scattering and diffusion regimes with optical depths ($\mu_s z$) between 1 to 10. The light is assumed to maintain some of its properties in the multiple-scattering regime. Imaging techniques in confocal configuration (confocal microscopy and focus-tracked OCT) do not operate in the diffusion regime. Reflectance-mode confocal imaging operates mostly in the single scattering regime, where light transport is dependent both on scattering coefficient (μ_s) and scattering anisotropy (g) whereas OCT operates in the single and multiple scattering regimes because of the large penetration depths compared to confocal microscopy. Hence, measurements by confocal microscopy can separate

μ_s and g. There are no techniques currently available that can measure μ_s and g simultaenously.

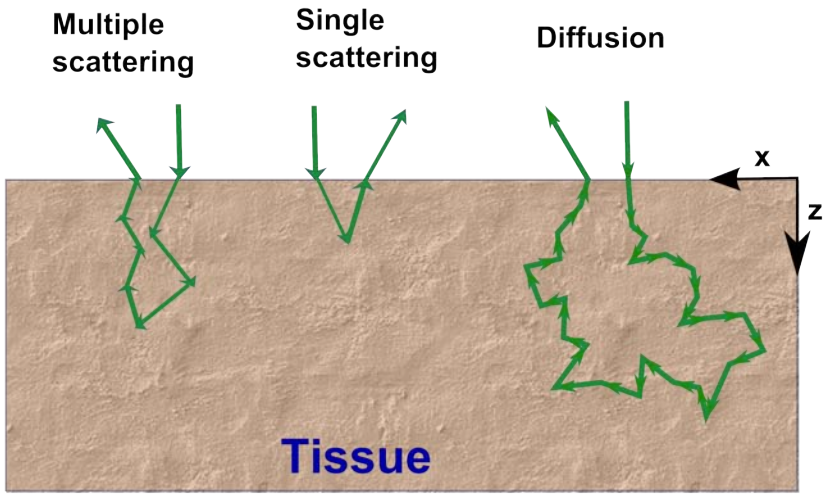

Figure 2.4: Scattering regimes of light propagation in tissue. Single scattering ($\mu_s z \approx 1$), multiple scattering ($\mu_s z < 10$) and diffusion ($\mu_s z \geq 10$)

2.1.3 Measurement of Optical Properties

Several methods are used to determine optical properties of tissues. A summary of the methods that are not used in this thesis are given below. A detailed review of the optical properties and measurement techniques can be found in Welch *et al.* [36].

Determination of optical properties can be characterized to two ways, direct methods and indirect methods. Direct methods involves measurement of optical properties by directly measuring the light absorbed or scattered from optically thin tissue sections. Direct methods involve measurement of microscopic coefficient (absorption coefficient, attenuation coefficient) without the need of a model of light

propagation. Direct methods are used to measure μ_s, μ_a, $p(\theta)$ and g. Direct methods include, collimated transmission experiment, integrating sphere [43, 44], and goniometric measurements [40] with optically thin tissue sections to have only a single scattering event during light transmission. Indirect methods involve deriving optical properties from macroscopic measurements of diffuse reflectance and transmittance or added absorber method [45] by solving the inverse problem. Forward problems determine the distribution of radiant energy in a tissue for given optical properties, whereas inverse problems derive the optical properties of the tissue from measurement the interaction of light with tissue.

Integrating sphere measurement is the most common method used to find optical properties of tissue. In this method a hollow sphere coated with diffuse reflective material is used. The sphere has entrance and exit ports where thin tissue samples are placed depending on reflectance mode (exit port) or transmission mode (entrance port) measurement. Light entering the spheres undergoes multiple reflections due to the diffuse reflective coating on the inside the sphere and loose original incident light direction. The fraction of the total diffuse light in the sphere escaping through the detector port is measured by the detector on the surface of the sphere. The light is detected through the detector port on the sphere. Reflectance mode and transmission mode measurements are made. These two measurements can be mapped to optical properties μ_s' and μ_a using inverse adding doubling theory [46, 47] or inverse Monte Carlo [48]. The collimated transmission technique is used to determine μ_s, which can be substituted in μ_s' to calculate g. Implementation of the integrating sphere method has several limitations. With high scattering coefficients of tissue, extremely thin sections ($\approx \mu m$) of tissues are needed to avoid multiple scattering. Tissues have typical scattering coefficient in the range of 100 - 1000 cm^{-1}. Thus, the sample thickness should be around 10 μm. Moreover, using thin samples is complicated by rapid dehydration and shrinking of the tissue

sections. Sample preparation involved to make such thin sections can alter optical properties and introduce artifacts. In order to make thin sections, tissue are fixed in paraffin or frozen. Freezing or fixing tissue using Formalin alters tissue structure that changes the optical properties of the tissue.

The scattering phase function $p(\theta)$ can be measured using another common technique called goniometry. In this method, the fraction of incident light scattered from a thin tissue sample at different angles is measured. This technique is similar to collimated transmission. In collimated transmission only the light transmitted collinear to incident light is measured, where as in goniometry the detector is placed on a rotating arm to record the fraction of scattered light at different angles. An alternative method is to project and record all the scattered light on a screen. The xy space is mapped into angle space [49]. Goniometry needs thin tissue sections similar to collimated transmission method, hence suffers from limitations presented in previous paragraph.

Indirect methods include diffuse reflectance methods, photo-acoustic methods and the added-absorber method. Generally optical properties used in diffusion theory, absorption coefficient (μ_a) and reduced scattering coefficient (μ_s'), are determined by these methods. These properties can be used to study energy deposition involving optical techniques that rely on diffuse light transport like the PDT [19], Diffuse reflectance [24–27], Oblique-incidence reflectance method [29] were developed to measure optical properties of tissues *in vivo*.

Different indirect methods available to measure optical properties of thick tissue sections and *in vivo* is summarized in the literature [36]. All the techniques use the diffusion approximation of light transport in tissue to provide only μ_a and μ_s'. These techniques can not measure the scattering coefficient (μ_s) and scattering anisotropy (g) individually. A technique based on reflectance mode confocal microscopy or OCT to determine optical properties of scattering (μ_s and g) is de-

veloped in this thesis. Scattering of light by tissue depends on the ultrastructure which can be characterized in terms of μ_s and g. Pathological changes like cancer induce structural changes in tissue, such as change in nuclear size, pleomorphism (change in shape of nuclei), number of nuclei and changes in extra-cellular matrix proteins like collagen. These structural changes affect the scattering properties, which can be monitored to differentiate normal tissue and neoplastic tissue.

This thesis describes a method to measure scattering coefficient (μ_s) and anisotropy factor (g) from a reflectance-mode confocal scanning laser microscope (rCSLM) signal. The concept of confocal microscopy is described in the following sections.

2.2 Confocal Microscopy

The concept of confocal microscopy was first described by Minsky [50] in 1957. A incoherent light source was used to image neurons in the transmission mode. Figure 2.5 shows the concept of confocal system compared to the conventional optical microscope. In a conventional optical microscope the image is projected on the detection plane from the sections of tissue, fixed on a glass slide. The image generated by an optical microscope is formed by the integration of the light transmitted through the whole sample thickness. The optical microscope image is formed both by the signal in focus and the signal from above and below the focus (out-of-focus signal), figure 2.5. This out-of-focus signal affects the signal to noise ratio of the image and decreases the contrast in the image.

Confocal microscopes mitigate this by adding a spatial filter at the detection plane. This spatial filter is at the focus of the tube lens projecting image onto the detector. The spatial filter is aligned such that only the light from the focus of the objective lens in the sample can pass through the spatial filter and reach the detector. The focal plane of the objective lens and the focal plane of the tube

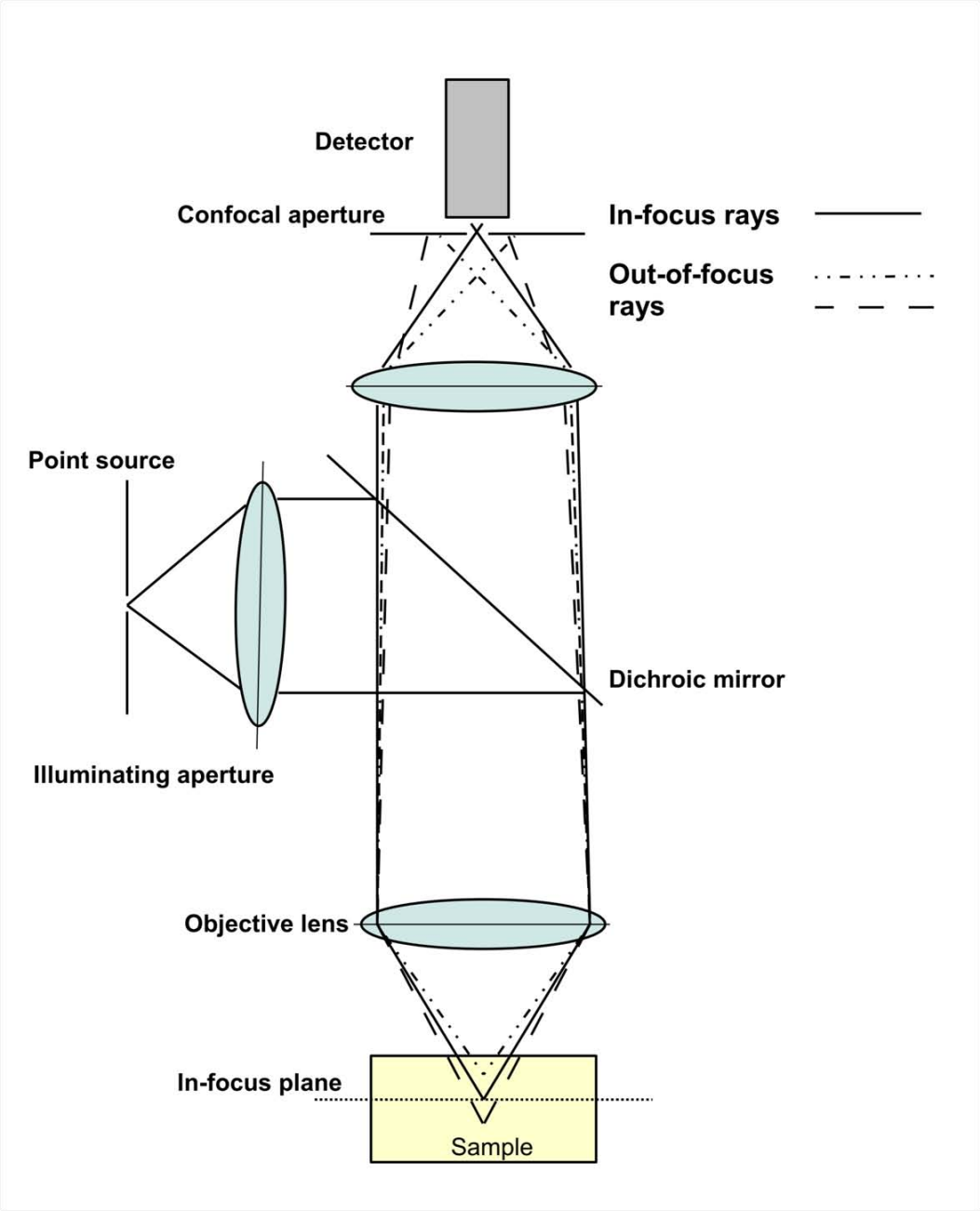

Figure 2.5: Schematic of the confocal microscopy concept. Signal from above and below the In-focus plane (dotted lines) is blocked by the confocal aperture (pinhole). Rejection of the background signal enhances the contrast and resolution of the confocal system. The dichroic mirror reflects the excitation to the sample and transmits the fluorescence from the sample to the detector. The dichroic mirror is replaced by a beam-splitter to configure the system for reflectance-mode confocal imaging.

lens are called **con**jugate **focal** planes, hence the name "Confocal" microscope. The effect of the pinhole is to selectively detect the light scattered from the point of geometric focus of the objective lens within the tissue. As a result, the data acquired are sensitive to the light scattered from in-focus and less sensitive to the light scattering from out-of-focus. Blocking the out-of-focus signal improves the contrast and resolution of the confocal microscope.

By scanning the sample point by point, an image can be formed voxel-by-voxel. The ability to reject out-of-focus signal enables imaging only a thin section in a thick sample, which is defined as optical sectioning. Three-dimensional images of a thick sample can be generated by optical sectioning, by moving the sample along the optical axis and capturing an image of the thin section normal to the optical axis.

While the concept of confocal microscopy was known since 1957 [50], it remained unnoticed due to the lack of technology to commercialize it. The development of high-intensity light sources (lasers), digital image manipulation algorithms, light scanning systems, optical filters and highly sensitive detectors led to the resurgence of interest in confocal microscopy. Commercial instruments were introduced in the late 1980s by several companies.

Confocal microscopes are used both in fluorescence mode and reflection mode by appropriately configuring the excitation and emission wavelengths. The ability to generate high resolution and high contrast fluorescent images make confocal microscopes popular with biologists. Development of fluorophores and immunofluorescent techniques contributed to the omnipresence of the confocal microscope in biochemical laboratories around the world [51, 52]. Apart from biomedical research, confocal microscopes are used in medicine in the fields of dermatology [14, 15, 53–57] and ophthalmology [58–60]. The reflectance mode was adopted by the material industry to non-destructive evaluation of microchips [61].

2.2.1 Fluorescence-mode confocal microscopy

Confocal microscopy is widely used to image fluorescence from biological samples. The ability to reject out-of-focus signal, enables rejection of fluorescence from above and below focal plane. The out-of-focus fluorescence degrades contrast in wide-field fluorescence imaging. Development of optical filters with sharp cut-off enabled higher signal-to-noise ratios in fluorescent imaging mode by efficient separation of reflected excitation light from fluorescent signal. Use of biological fluorophores such as green fluorescent protein (GFP) made tremendous contributions to the field of biomedical science.

2.2.2 Reflectance-mode confocal laser scanning microscope

While the fluorescence-mode confocal microscope is more popular, the reflectance-mode confocal microscopy is gaining popularity [13, 16]. Fluorescent-mode imaging involves introduction of exogenous fluorophores into the sample (tissue), while the reflectance-mode utilizes endogenous contrast from the scattering of light by the sample. Since light scattering depends on the ultra-structure of the tissue, the rCSLM technique can be used to characterize tissues, which is the topic of this thesis.

Refractive index fluctuations in tissue causes light scattering. The reflectance from skin is in the order of 10^{-4} times the incident laser power. Rajadhyaksha *et al.* [14] developed a reflectance-mode confocal microscope to image human skin. They introduced an updated system in 1999 with better resolution, contrast, field-of-view and depth of imaging [15]. Rajadhyaksha *et al.* [14] introduced the use of optical contrast from Melanin in skin to increase the depth of imaging to 350 μm. These advancements led to the development of a commercial reflectance-mode confocal imaging system to image skin, Vivascope 1500 (Lucid Technologies).

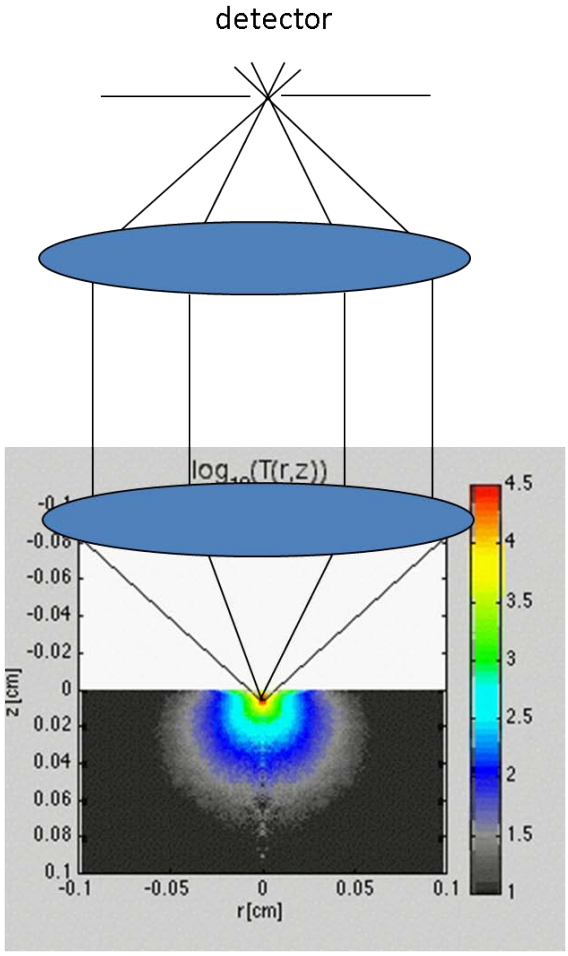

Figure 2.6: Reflectance-mode Confocal Scanning Laser Microscope (rCSLM) configuration. The above illustration shows the photons scattered from focal volume are collected by the objective lens and passed through the pinhole to be detected. The Monte Carlo simulation of the fluence rate in a tissue, due to the launch of a focused beam, is shown.

2.3 Functional confocal microscopy

In the past decade, several groups have developed algorithms to estimate optical properties of tissues using confocal microscopy (CM) [21, 22, 62] and OCT. Faber *et al.* [17] extracted estimates of the attenuation coefficient (μ_t) of weakly scattering ($\mu_s < 6mm^{-1}$) tissue mimicking samples from a dynamic focusing OCT. They used single-scattering model to fit the OCT signal as a function of depth.

Optical coherence microscopy (OCM) which combines the confocal microscopy with optical coherence interferometry can provide enhanced optical sectioning capabilities in the tissues [63]. While confocal microscopy can image up to 5 mean free paths (mfp), theoretically OCM can enable imaging 5-15 mean free paths (mfp) in depth enabling the ability to image many tissue structures that are of interest to histopathology.

Several groups have fit the confocal signal as a function of depth to decaying exponential to determine total attenuation coefficient. Smithpeter *et al.* [62] and Dunn *et al.* [21] have measured total attenuation coefficient of tissues by fitting the confocal signal as a function of depth to a decaying exponential function given by ($S = S_o e^{A\mu_t z}$). Where μ_t is the total attenuation coefficient ($\mu_t = \mu_s + \mu_a$) of the sample and parameter A is a decay constant, which is dependent on the scattering properties of the tissue. The constant A is dependent on the number of scattering events and type of the detected photons, single scattered or multiple scattered photons. They show that the constant A is dependent on the numerical aperture (NA) of the objective lens. Chou *et al.* [64] proposed the decay constant A is a function of NA and μ_t, which has information about the properties of the turbid media. The constant A encodes information on the depth limits of imaging with ballistic, single scattered and multiple scattered photons. They showed that the decay of ballistic photons in confocal system with depth is dependent on NA for NA>0.25. They also showed that the signal decayed faster as the NA increased that they hypothesize to be due to the varying pathlengths of the photons across the angle of acceptance of objective lens.

This chapter background on tissue optics and defined the optical properties of tissues. An overview of the origin of optical properties and techniques to measure them was provided. The concept of reflectance-mode confocal microscopy and its biomedical applications was discussed. The chapter ended with a review

of literature, on the use of the confocal microscopy and OCT for the characterization of tissue structure. This provides the background information on the work described in this dissertation. A novel technique to specify optical properties of tissue non-invasively from rCSLM data is described in the next chapter.

Chapter 3

Theoretical model to estimate optical properties from rCSLM signal

Several techniques have been developed in the past two decades to estimate optical properties including diffuse reflectance, diffuse transmission and reflectance as a function of source-detector distance [25, 29, 47]. A brief overview is provided in the section 2.1.3. These techniques can measure absorption coefficient (μ_a) and reduced scattering coefficient (μ_s'). However, it is specifying scattering properties: μ_s and g separately is difficult, and requires a tissue sample to be removed to allow other measurements, like collimated transmission or goniometry.

In this chapter a novel method to estimate μ_s and g simultaneously from rCSLM signal is described. A theoretical model is developed to map the parameters determined from fitting rCSLM signal to optical properties of tissue. The model links the results from the experiments to the optical scattering properties of the tissue and characteristics of the imaging system used.

3.1 Theoretical Model

A theoretical model was developed to estimate optical properties from the depth-dependent decay of the confocal signal based on inverse Monte Carlo (MC) method. The confocal signal decays exponentially as the focus moves deeper into the tissue (figure 3.1) as:

$$R(z) = \rho\, e^{-\mu z} \tag{3.1}$$

where ρ $[dimensionless]$ is the local reflectivity and μ $[cm^{-1}]$ is the attenuation coefficient.

The two parameters ρ and μ are the dependent on characteristics of the tissue and the imaging system (axial resolution, NA of objective lens etc.). A theoretical model was developed to describe the fitting parameters μ and ρ as a function of scattering properties (μ_s and g) of the tissue and imaging system parameters.

Monte Carlo (MC) methods models light propagation in tissue by using random number generators, to sample probability distributions that represent step size between scattering events and the deflection angle due to scattering. In MC methods light is represented by packet of photons with specific weight, that propagate through the turbid medium. A weight is deposited at a the site of absorption (by chromophores) and the remaining weight is scattered to a different location in the tissue. Monte Carlo simulation of a confocal system of forward problem involves launching a packet of photons as a circular beam towards the focal point in the medium with assigned optical properties. The photons reflected or transmitted from the focus into the NA of the lens are collimated and refocused into a pinhole to mimic confocal arrangement. The simulations are repeated with the focus at different depths and for a range of optical properties. The effect of each optical property on the reflectance measured in the confocal arrangement is analyzed from these simulations. Analysis of the data from the simulations revealed a relationship

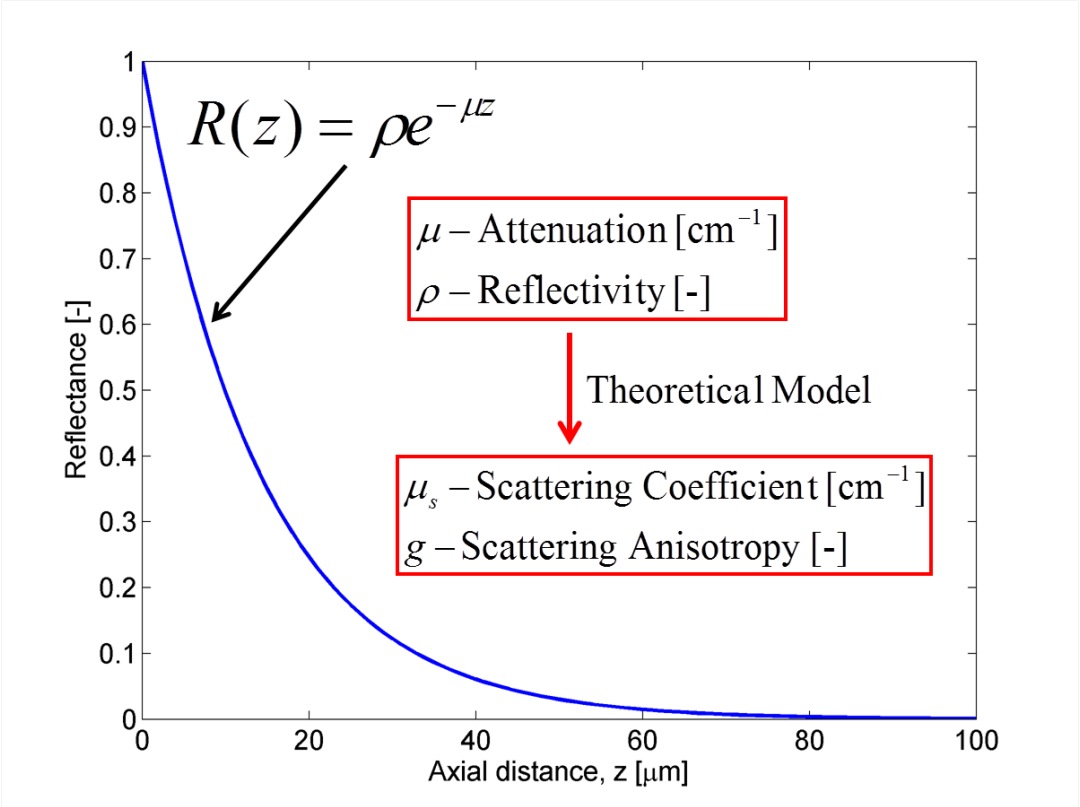

Figure 3.1: The rCSLM signal as a function of depth ($R(z)$) is an exponential that is characterized by local reflectivity (ρ) [dimensionless] and an attenuation coefficient (μ) [cm^{-1}]. The thesis maps the (μ, ρ) to scattering properties of tissues (μ_s, g).

between the optical scattering properties and the confocal signal as a function of depth.

We developed a theoretical model that connects the fit parameters (μ, ρ) to the optical properties (μ_s, g) according to:

$$\mu = (\mu_s \, a(g) + \mu_a) \, 2G(g, NA) \tag{3.2}$$

$$\rho = \mu_s \, \Delta z \, b(g, NA) \tag{3.3}$$

The next sections define and motivate the development of these parameters.

Briefly, scattering efficiency factor, $a(g)$, is a factor that quantifies the ability of the photons to reach the focus despite scattering (determined from Monte Carlo simulation). $a(g)$ drops from 1 to 0 as g increases from 0 to 1. Pathlength augmentation factor, $G(g, NA)$, is a geometry factor that describes the average photon pathlength to and from the focal point in the sample, that depends on the Numerical Aperture (NA) of the lens and on the anisotropy (g). Δz represents the axial resolution of the confocal system. The scatter efficiency factor, $b(g, NA)$, is the fraction of the scattered light at the focus that backscatters into the objective lens NA for detection. Absorption coefficient (μ_a) scales the attenuation coefficient (μ) and is generally small in the turbid media considered in this thesis. This method can be used to measure μ_a non-invasively from the sample as long as the lumped parameter $\mu_s\, a(g)$ is known. If the scattering properties of the sample are known *a priori*, the absorption coefficient of the absorber added to the sample can be measured by this method.

The parameters in equations 3.2 and 3.3 are described in the following sections.

3.1.1 Scatter Collection Efficiency - $b(g, NA)$

The scatter collection efficiency, $b(g, NA)$, is the fraction of light backscattered by the tissue within the focus that reaches the objective lens and can be refocused to pass through pinhole and reach the detector. Figure 3.2 schematically describes the concept of $b(g, NA)$. The angular distribution of the light scattered at focus is dependent on the scattering phase function $p(\theta)$, as shown in the figure 3.2. The figure shows a scattering event (green spot) at the focus and the light scattered in all angles, whose distribution is given by $p(\theta)$. The part of the angular distribution $p(\theta)$ of light that overlaps with collection angle of objective lens contributes to $b(g, NA)$ (shown in blue color) in the figure 3.2. Note the figure 3.2 depicts $b(g, NA)$ in the reflectance-mode imaging configuration, in transmission mode the geometry

of the collecting lens should be considered. $b(g, NA)$ is dependent on the maximum collection angle (α) of the objective lens, which is dependent on the NA and refractive index of the coupling medium (n) given by equation 3.4.

$$\alpha = sin^{-1}\left(\frac{NA}{n}\right) \tag{3.4}$$

$b(g, NA)$ is calculated by integrating the phase function ($p(\theta)$) across the collection geometry of the objective lens (blue region). Mathematically it is defined as:

$$b(g, NA) = \int_{\pi-\alpha}^{\pi} p(\theta)\, 2\pi sin(\theta) d\theta \tag{3.5}$$

Figure 3.2 represents $b(g, NA)$ for the photon launched in optical-axis only, but since the light is focused, the photons are launched towards the focus off-axis too. The effect of off-axis launch and collection on $b(g, NA)$ was analyzed by Truffer *et al.* [65] and found to be insignificant compared to equation 3.5.

We used the Henyey-Greenstein (HG) phase function in our analysis, which is given by equation 2.2. The HG phase function is a function of g only. Figure 3.3 shows the factor $b(g, NA)$ calculated for different values of g and NA. The NA of the water-dipping objective lens used in the confocal system is 0.9 (LUMPlanFL, Olympus America, Melville, New York). The fraction $b(g, NA)$ is a strong function of Numerical Aperture (NA) and a weak function of scattering anisotropy (g).

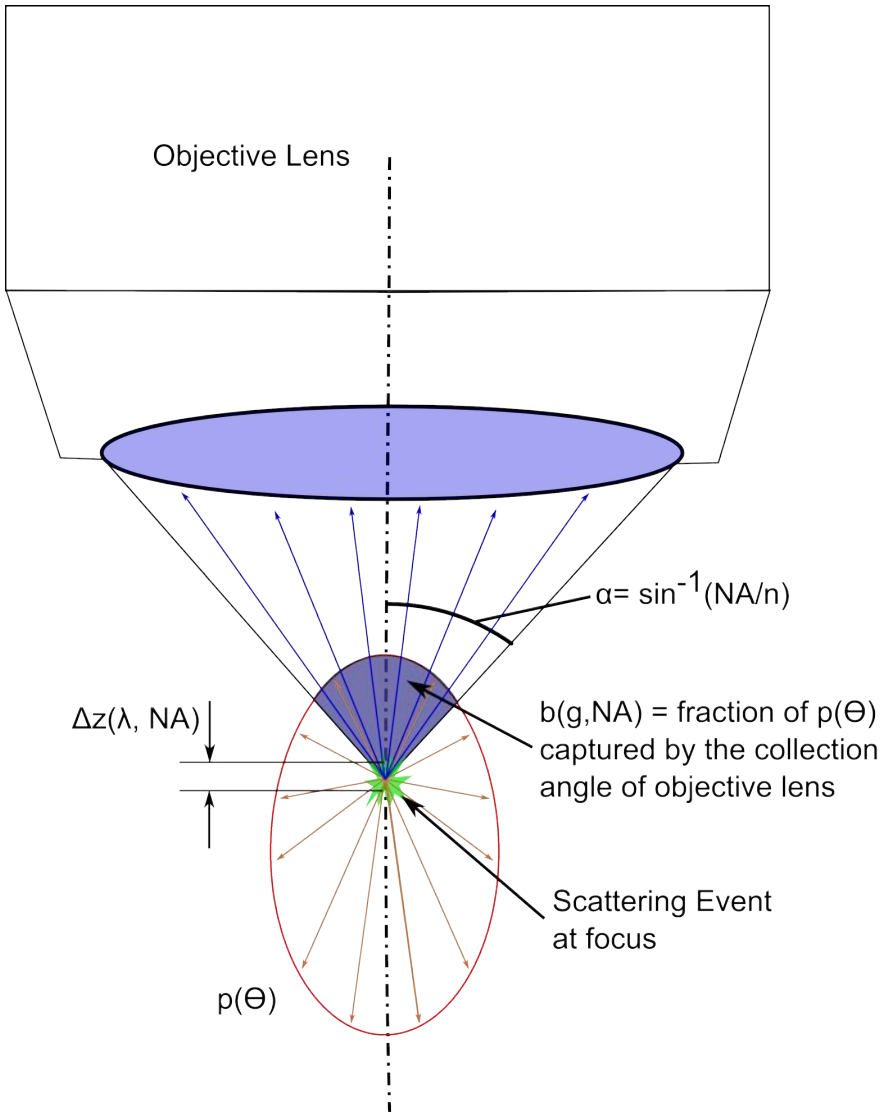

Figure 3.2: Schematic of the $b(g, NA)$. The scattering event at the focus (green), deflecting light according to scattering phase function ($p(\theta)$) is depicted. Only, a small fraction (blue region) of the $p(\theta)$ escapes through the collection cone of the objective lens and contributes to the signal.

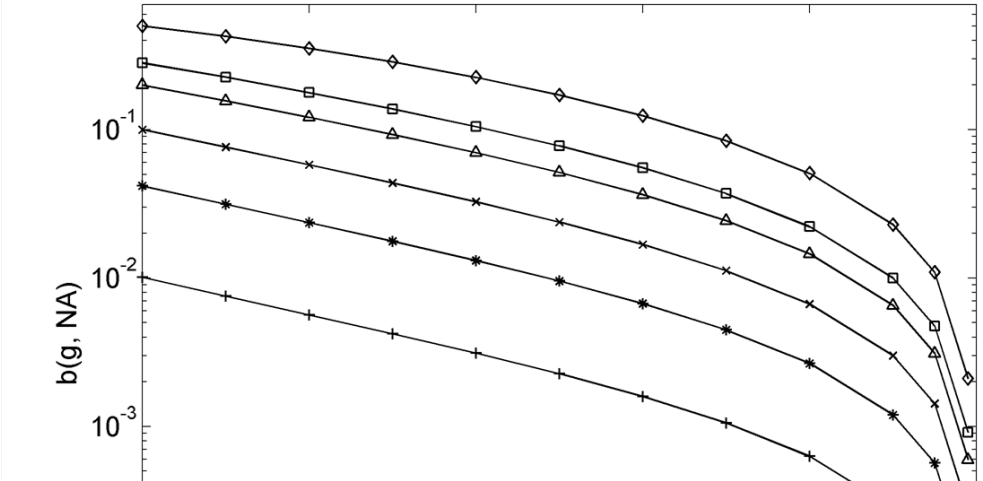

3.1.2 Axial resolution of the imaging system - Δz

Theoretically the axial resolution (Δz [μm]) of the confocal system is given by equation 3.6 [66]. The factor f in equation 3.6 accounts for the difference between the theoretical axial resolution and the apparent axial resolution of the confocal system. The theoretical Δz depends on properties of objective lens and wavelength (λ), however the apparent axial resolution of the system is dependent on the on the optics in the detection arm: tube lens that focus light into the pinhole and alignment of the pinhole, along with objective lens. The factor f, is estimated from calibration experiments done with microspheres optical phantoms (section 4.3.1). Calibration with a microsphere phantom enabled us to estimate the value f from the difference between the (μ, ρ) values calculated from Mie theory and the (μ, ρ) values measured from the confocal system. The value of f is 1.3 for the confocal system. A tissue mimicking phantom made of 2% v/v 0.1-μm diameter microsphere suspensions was used as a standard phantom which is homogeneous and gave consistent results to estimate the value of f.

$$\Delta z = f\frac{1.4\, n\, \lambda}{NA^2} \tag{3.6}$$

where λ is the wavelength of the excitation light.

n is the refractive index of the coupling medium (1.33 for water-dipping objective lens).

f is the axial calibration factor, that accounts for the difference between the theoretical axial resolution and the apparent axial resolution of the confocal system.

Local reflectivity (ρ) defines the amount of light reflected from the focus that reaches the detector. This depends on the scattering properties of the sample, the magnitude and direction of the light scattered at the focus and the fraction

of the scattered light that was able to propagate back from the sample through the imaging system to be detected by the detector, which depends on the optics (objective lens). The factor $\mu_s \, \Delta z$ represent the number of scattering events (on average) that occurred at the focal volume. This factor is typically less than 1 in microscopic imaging system. The factor $\mu_s \, \Delta z$ represents the magnitude of scattering at the focus. The factor $b(g, NA)$ represents the fraction of the scattered light that was directed into the collection angle of the objective lens, which is a function of angular distribution of scattered energy ($p(\theta)$) and the collection efficiency (NA) of the objective lens. So, ρ relates light detected from the focal point in the sample to the optical properties of the sample and parameters of the imaging system.

3.1.3 Pathlength Augmentation Factor - $G(g, NA)$

As the light is focused, photons launched off-axis have to travel further than the on-axis photons to reach the focus and back. The pathlength augmentation factor $G(g, NA)$ accounts for this extra pathlength than the axial distance from the surface of the tissue to the focus, that the photon has to travel. The factor 2 accounts for the propagation of photons into and out of focus.

For low NA objective lens (used in OCT) G is approximately given by:

$$G(g, NA) = \frac{1}{cos(sin^{-1}\frac{NA}{n})} = \frac{1}{\sqrt{1 - (\frac{NA}{n})^2}} \tag{3.7}$$

where $sin^{-1}(\frac{NA}{n})$ is the maximum launch and escape angle from the objective lens.

For a high NA objective lens, the factor G is determined by taking the average of the paths the photons can take to and from the focus, when launched from all the possible positions from the objective lens aperture. This can be represented

by the following equation:

$$G(g, NA) = \frac{\int_{\gamma=0}^{\alpha} \int_{\beta=-\alpha}^{\alpha} \frac{1}{2}\left(\frac{z_f}{cos(\gamma)} + \frac{z_f}{cos(\beta)}\right) p(|\gamma - \beta|) L_{arc}(\beta) d\beta d\gamma}{\int_{\gamma=0}^{\alpha} \int_{\beta=-\alpha}^{\alpha)} p(|\ \gamma - \beta\ |) L_{arc}(\beta) d\beta d\gamma} \tag{3.8}$$

where z_f is the depth of the focal volume, γ is the angle of incidence relative to the z axis, β is the angle of collection, and L_{arc} is the segment of the scattering phase function that falls within the numerical aperture of the lens. The $p(\theta)$, where $\theta = |\gamma - \beta|$, is the Henyey-Greenstein scattering function. The G is only weakly affected by the anisotropy of the scattering function (Figure 3.6C).

3.1.4 Scattering Efficiency Factor - $a(g, NA)$

The scattering efficiency factor $a(g, NA)$ accounts for the ability of the photons to reach the focal point in the sample despite scattering. It affects the effectiveness of scattering coefficient (μ_s) to attenuate the light traveling to the focus. $a(g, NA)$ is predominantly dependent on g and drops from 1 to 0, as the g increases from 0 to 1(Figure 3.6B). This is determined from Monte Carlo simulations, where the photons are launched into the sample towards a focus and the relative fluence rate at the focus F [W/cm^2 per W delivered] is recorded. The simulations were done for range of g and μ_s (details in the following sections) values which gave the equation for $a(g, NA)$, given by:

$$a(g) = 1 - exp\left(\frac{-(1-g)^m}{n}\right) \tag{3.9}$$

where $m = 0.6651$ and $n = 0.1555$. The experiments in this dissertation use equation 3.9 in the analysis.

In section 3.1.3 G, which is the extra pathlength the photon has to travel to

reach the focus, is defined as a function of NA of the objective lens. However, the effective pathlength of the photons from the surface of the tissue to the focal point in the tissue also depend on scattering anisotropy (g). At higher values of g (≈ 1), $a(g, NA)$ approaches 0, which causes more light entering the sample from the edge of the focusing cone to reach the focus, leading to a higher value of G. Conversely, sample with low g value decreases the value of G. The Monte Carlo simulations were updated to determine the effect of g and $a(g, NA)$ on geometry factor (G) which is the extra pathlength the photon has to travel to reach the focus. The following sections describe the updated model that includes the effect of anisotropy (g) on the geometry factor ($G(g, NA)$).

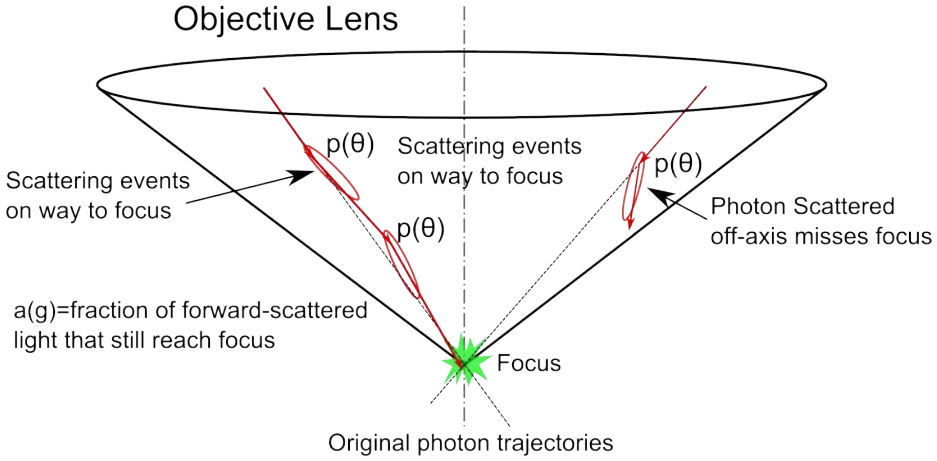

Figure 3.4: Schematic of the $a(g)$ that shows how photon scattering forward on-axis can reach the focus adding to the unscattered light, while the photons scattered off-axis will miss the focus, contributing to the attenuation.

Figure 3.5 shows results from the Monte Carlo simulations of focused light transport into a tissue. The simulations included $g = 0.10$, 0.50, 0.80, 0,90, 0.95 and 0.99, but only 3 examples are shown in figures 3.5A, 3.5B and 3.5C, corresponding to $g = 0.10$, 0.95 and 0.99, respectively. For each g, the curves on the left show the

central axial profile of the relative fluence rate here called transport, $T[1/cm^2]$, as a function of depth z within the tissue. The lens has a numerical aperture (NA) of 1.26 and the tissue has a refractive index of $n = 1.4$, such that the effective NA entering the tissue is $\frac{NA}{n} = 0.90$. The focus of the objective lens is set at a constant depth $z_f = 0.0400$ cm. The family of curves within each figure is for increasing values of optical scattering coefficient, $\mu_s = 1.25$ to 625 cm^{-1}. The profiles $T(z)$ illustrate how more light reaches the focus at z_f when g is large.

In figure 3.5 on the right, the curves show the transport T to the focal volume. The transport to the focus, $T(z_f)$, is plotted versus the optical depth (OD) of the focus, $OD = \mu_s z_f$ [dimensionless]. As the OD increases, the $T(z_f)$ decreases exponentially, until multiply scattered diffuse light causes the curve to bend toward a background value consistent with diffusion theory. The data at low OD were fit with an exponential:

$$T(z_f) = T(0)\, e^{-aG\mu_s z_f} \tag{3.10}$$

This yields the factor aG and a scalar $T(0)$. In the figure 3.5, the data are normalized by $T(0)$, so that the exponential decay extrapolates back to unity at $OD = 0$. In other words, the curves show $T(z_f)/T(0)$ versus $OD = \mu_s z_f$. Figure 3.6A summarizes the values of the product aG as a function of g.

The next step was to separate the factor aG into its two components, a and G, as functions of g, which are plotted in figures 3.6B and 3.6C. The process is illustrated in figure 3.7. An initial value a was assumed, eg., $a = 1$. Then equation 3.12 was used to calculate the normalized transport, $T(z_f)/T(0)$, to the focus:

$$\frac{T(z)}{T(0)} = \frac{\int_{\alpha=\pi}^{\pi-\alpha_{max}} Gauss(\alpha) e^{-a\mu_s z_f/cos(\alpha)} 2\pi sin(\alpha) d\alpha}{\int_{\alpha=\pi}^{\pi-\alpha_{max}} Gauss(\alpha) 2\pi sin(\alpha) d\alpha} \tag{3.11}$$

The denominator of equation 3.11 accounts for all the light delivered to the

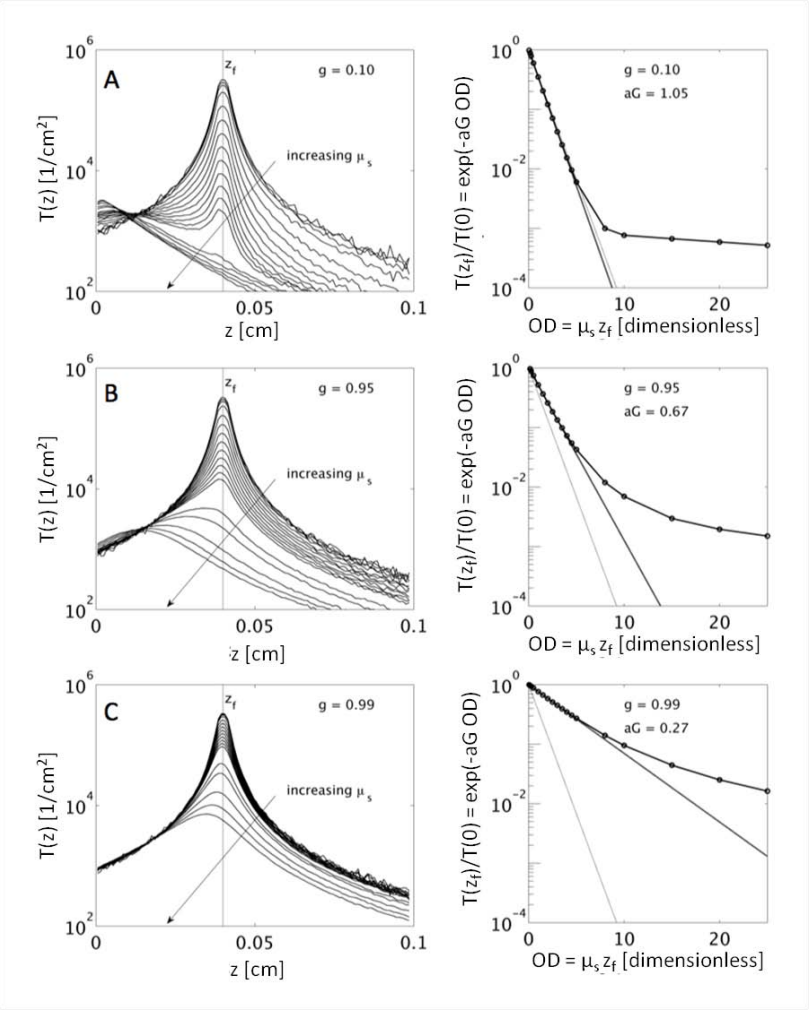

Figure 3.5: Transport ($T(z)[1/cm^2]$) into homogeneous tissue with varying scattering coefficient (μ_s) and anisotropy of scattering (g). (A) $g = 0.10$, broadly scattering. (B) $g = 0.90$, forward-directed scattering. (C) $g = 0.99$, very forward-directed scattering. (Left) $T(z)$ shows the transport versus depth. The focus of the objective lens is constant at $z = 0.0400$ cm (vertical thin line at z_f). (Right) $T(z_f)$ versus $\mu_s z_f$, showing the $T(z)$ at the focus for varying μ_s. Thick solid straight line is exponential fit to the initial attenuation, which specifies a value for the product aG (Equation 3.10). The thin straight line is $exp(-\mu_s z_f)$.

focus in the Monte Carlo simulation for the case of no attenuation. The factor $Gauss(\alpha)$ describes the Gaussian distribution ($Gauss(\alpha) = exp((\alpha/\alpha_{max})^2)$, where $\alpha_{max} = sin^{-1}(NA_{eff})$) of beam entry into the tissue as a function of incident angle α within the tissue. Integrating over all α angles yields the total normalized

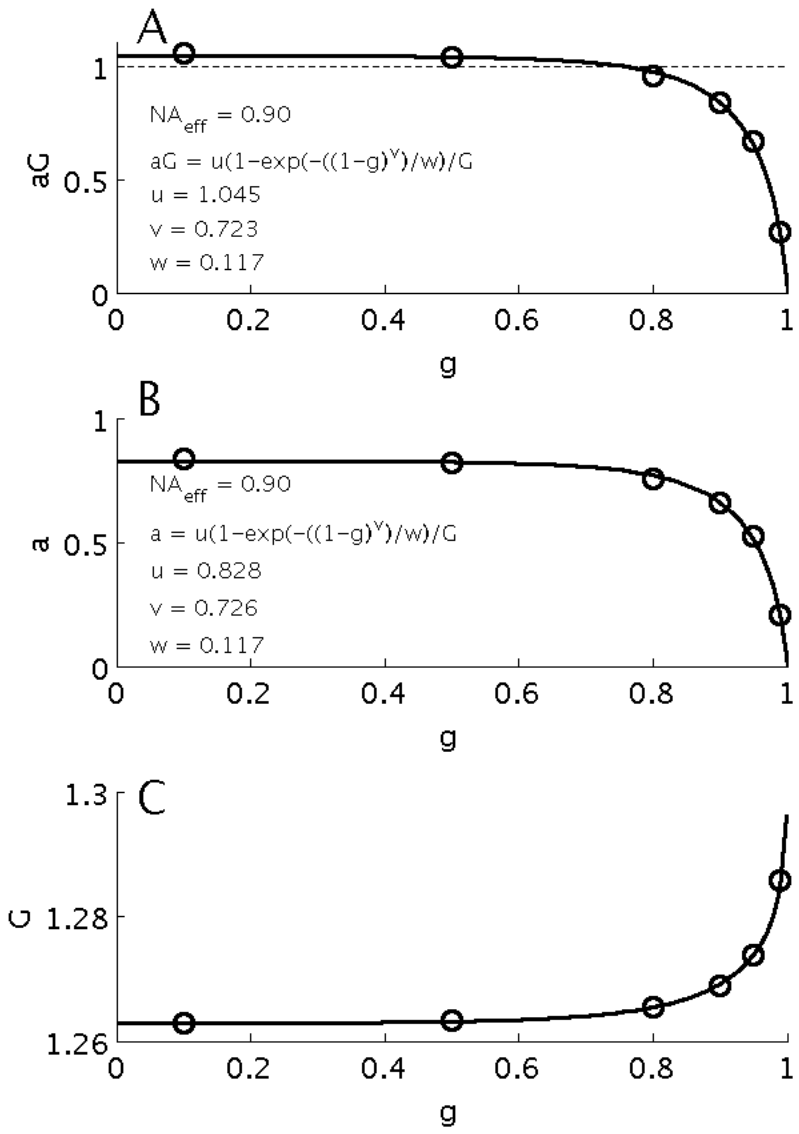

Figure 3.6: The functions aG(g), a(g) and G(g), for $NA_{eff} = 0.90$, based on Monte Carlo simulations.

transport to the focus. The angle π indicates direct backscatter direction of the scattering phase function, and the angle $\pi - \alpha_{max}$ is the angle at the edge of the focused beam (figure 3.2). For the Monte Carlo simulations reported here, the intensity at the edge of the beam was at $1/e$ or 37% of the intensity at the center of the beam. Then the T/A from equation 3.11 was substituted into equation 3.10

and rearranged to specify G:

$$G = \frac{-ln(\frac{T(z)}{T(0)})}{a\mu_s z_f} \tag{3.12}$$

This G divided the factor aG determined from Monte Carlo simulations to yield a:

$$a = \frac{aG}{G} \tag{3.13}$$

The value of a obtained by equation 3.13 was then reinserted into equation 3.11 to recalculate $T(z)/T(0)$, and equation 3.12 and 3.13 were used to recalculate G and a. Iterating equations 3.11 - 3.13 in this manner only 3 times was sufficient to allow a and G to achieve stable values, such that their product matched the original factor aG specified by the Monte Carlo simulations.

Figure 3.6B shows a versus g. The value of a is 0.83 for $g = 0$, in other words, some light multiply scatters in the forward direction and can still reach the focus even when scattering in isotropic. Scattering does not perfectly prevent light from reaching the focus when in this initial range of exponential attenuation where equation 3.10 holds. As g becomes forward directed, more light reaches the focus and hence the value of a drops. In other words, scattering becomes less effective in preventing light from reaching the focus.

Figure 3.6C shows G versus g. The factor G has an initial value of 1.263 at $g = 0$ (for the case of $NA_{eff} = 0.90$), but increases as g becomes forward-directed. At high g, more light from oblique angles reaches the focus, despite the longer oblique-angle photon path to the focus, and consequently the average pathlength of photons reaching the focus increases, so G increases (equation 3.11). The value at $g = 0.999$ is $G = 1.296$. While the value G change with g, the change is not as significant as the change in the value of $a(g)$ figure 3.6.

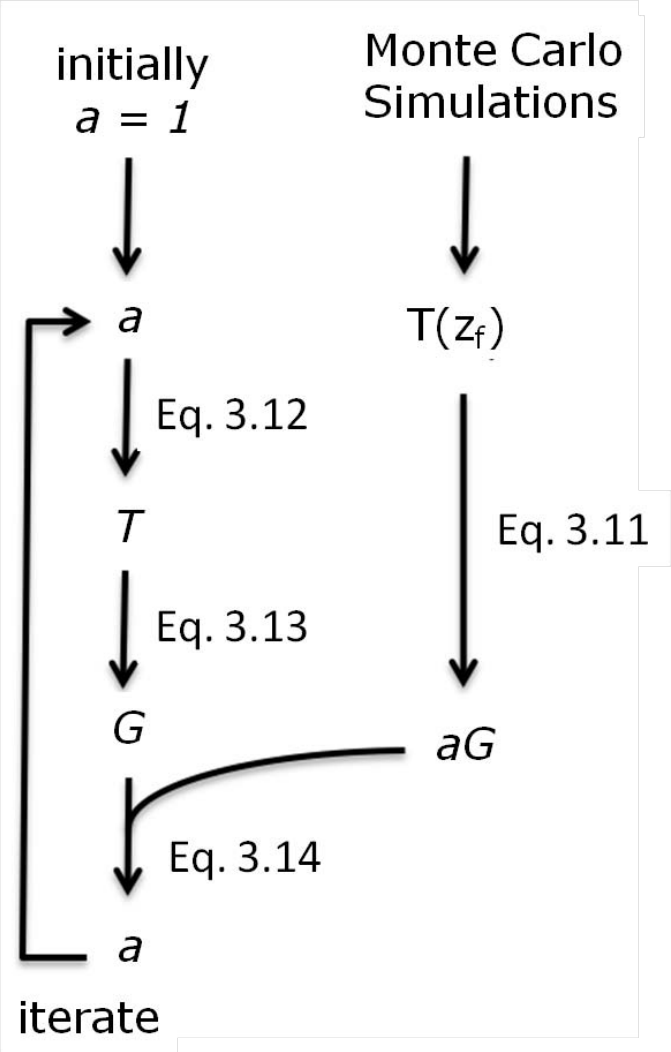

Figure 3.7: Iterative algorithm to separate a and G from the product aG.

3.1.5 Analysis Grid: (μ, ρ) to (μ_s, g) map

Using equations 3.2 and 3.3 empirically measured values of (μ, ρ) can be related to the optical properties of scattering (μ_s, g). The relationship between the variables μ and ρ, and the tissue optical properties μ_s and g, is depicted graphically in figure 3.8. The x and y axes are the specified fit parameters ρ and μ respectively. The (μ, ρ) pairs calculated for a range of optical properties of μ_s and g were plotted which generated a grid of $iso - \mu_s$ and $iso - g$ lines. This grid is addressed as

'analysis grid'. The scattering coefficient: $1 \leq \mu_s \leq 1000\ [cm^{-1}]$ and anisotropy: $0 \leq g \leq 0.99$ values were chosen to cover the typical range of optical properties of the biological samples at visible and near-infrared (NIR) wavelengths. The values of μ and ρ were calculated for a series of μ_s and g values using equations 3.2 and 3.3. The grid is plotted on a log-log scale as the values of μ span 3 orders of magnitude and the values of ρ span 5 orders of magnitude.

The position of the grid in the (μ, ρ) space is a function of the rCSLM system parameters as shown in equations 3.2 and 3.3. The grid shifts left (or right) as the wavelength (λ) decreases (or increases) proportional to λ, as ρ is proportional to Δz and the Δz is proportional to λ (equation 3.6). The grid shifts left (or right) if the NA decreases (or increases) since $b(g, NA)$ increases with NA (equation 3.3) and ρ is proportional to $b(g, NA)$ (equation 3.5). While the relationship between NA and G is complex (section 3.1.4), in general the grid shifts up (or down) as NA increases (or decreases).

Several interesting features can be observed in the grid plotted in figure 3.8. The grid depicts the non-linear relationship between the observed (μ, ρ) values and optical properties (μ_s, g). The $iso - \mu_s$ and $iso - g$ lines forming the grid provide insight into this relationship. For a given value of μ_s, as the value of g(anisotropy) increase, the attenuation decrease slowly for $g \leq 0.9$ and the decrease is sharp for $g \geq 0.9$. The reflectivity changes by three orders of magnitude for a given value of μ_s, which implies that the signal is highly dependent on anisotropy (g). Hence, anisotropy plays a critical role in the contrast of the rCSLM images. The ability to estimate anisotropy (g) provides a greater opportunity to characterize tissues using rCSLM images.

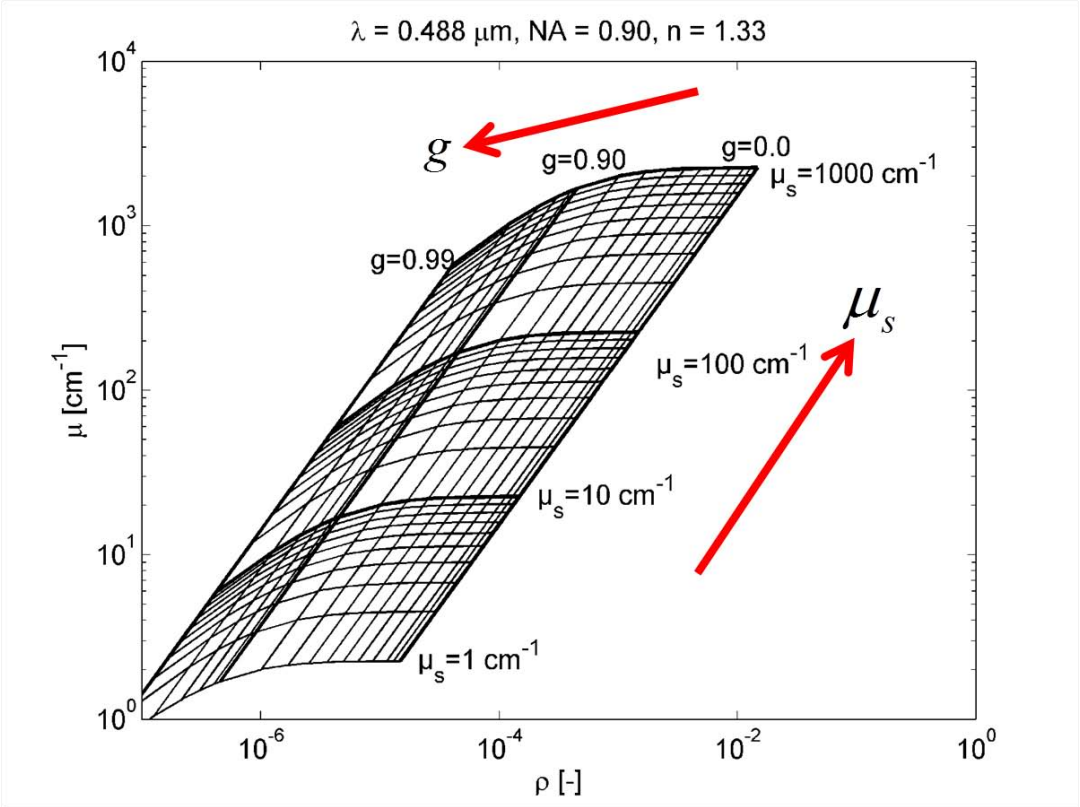

Figure 3.8: Plot of the grid that maps the fit parameters (μ, ρ) to the theoretical scattering properties (μ_s, g) for rCSLM confocal system used in the study. (at λ = 488nm, $NA = 0.9$, $n = 1.33$)

The experiment involves the acquisition of reflectance $(R(x, y, z))$ from the tissue by rCSLM. An axial profile at a particular (x,y) position $R(z)$ is calculated. The $R(z)$ profile is fit by the equation 3.1 to specify μ and ρ. Then the (μ, ρ) pair to mapped to the corresponding optical properties (μ_s, g) using the grid in figure 3.8.

This chapter presented a model to map experimental parameters: attenuation (μ) and reflectivity (ρ), determined by fitting the depth dependent decay of rCSLM signal into optical properties of scattering: scattering coefficient (μ_s) and scattering anisotropy (g). Validation of the model using optical tissue phantoms is described in chapter 4. Subsequent chapters deal with the application of the

model to estimate optical properties of murine tissues (chapter 5).

Chapter 4

Validation of the dependence of attenuation (μ) and reflectivity (ρ) on scattering coefficient (μ_s) and scattering anisotropy (g)

Previous chapter described the model developed to map experimental parameters: attenuation (μ) and reflectivity (ρ), to optical properties of scattering: scattering coefficient (μ_s) and anisotropy of scattering (g), from rCSLM data. The model should be validated with a sample with known optical properties.

This chapter describes the rCSLM used in this thesis and the validation of the theoretical model. Tissue mimicking phantoms were commonly used to validate light transport models [67]. Microsphere suspensions were used as tissue phantoms. Optical properties of dilute microsphere suspensions can be calculated using Mie theory. The ability of the theoretical model to identify changes in μ_s and g was tested using different phantoms. The scattering coefficient of the microsphere phantoms were changed by varying the number density of the microsphere suspensions. The scattering anisotropy of the microsphere phantoms were changed by using spheres of different diameters.

4.1 Confocal Microscope System Description

Figure 4.1 shows the photograph of the rCSLM system built in our laboratory [1]. In the present study the system has been modified and several optical components were changed to improve the system performance and the detector electronics and the operating software was further optimized. For completeness the system layout is described in the following paragraphs.

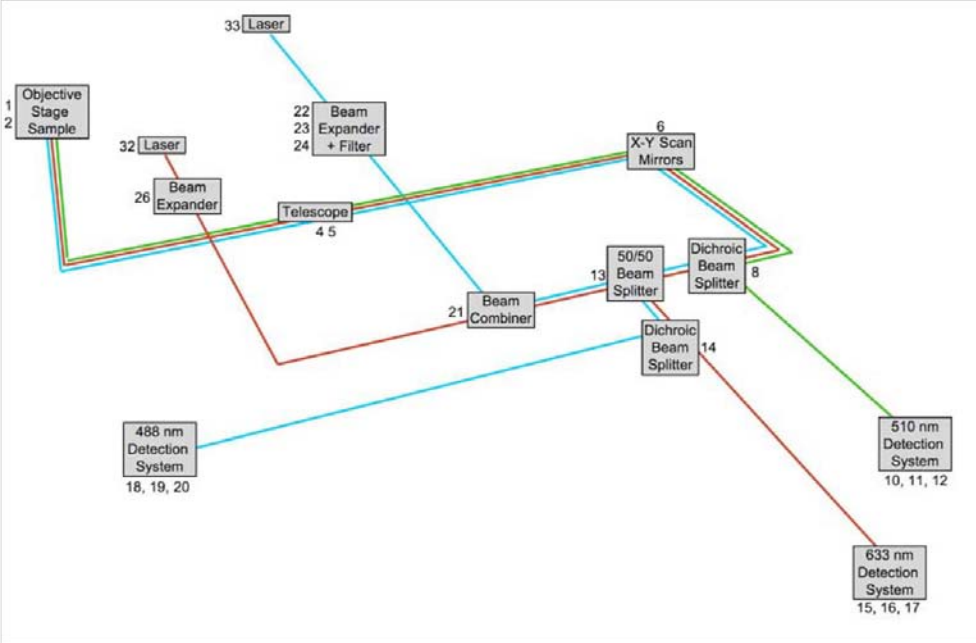

Figure 4.1: Block diagram representing the reflectance-mode confocal scanning laser microscope system. It is a three channel system with two excitation channels and three detection channels. The channels are represented with corresponding color lines in the photo [1]. Numbers are assigned to the optical components for identification in the text.

Excitation light (λ = 488nm and 633nm) is expanded from 1 mm to 1 cm, to the fill back-focal plane of the objective lens (8mm). The confocal system is set-up in the inverted-microscope configuration, where the light focuses upwards into the sample. A water-coupled objective lens (LUMPlanFL, Olympus America, Melville, New York) was used in this work as the refractive index of the tissue

($n \approx 1.37$) is sufficiently close to water ($n \approx 1.33$) that minimize the effect of the refractive index mismatch at the tissue-water boundary. The effect of refractive index mismatch is addressed in chapter 7 where the use of high refractive index optical clearing agents introduce error in the true location of focus compared to the apparent location of the focal point from tissue surface. In the studies with tissues and aqueous microsphere suspension phantoms this is not a problem as the refractive index of the sample and coupling medium are same (Tissue in tissue studies and water in microsphere tissue phantom). The focus is scanned laterally in x- and y-axis using galvo scanning mirrors (RS-15, Nutfield Technology Inc., Windham, New Hampshire). The optical axis (z-axis) scanning was accomplished by moving the sample with respect to the objective lens using a motorized stage (LS50A, Applied Scientific Instrumentation, Eugene, Oregon). All the beam steering hardware and data acquisition was controlled by custom software developed in LabVIEW^{TM} (National Instruments, Austin, TX). The light reflected from the tissue is deflected into corresponding detectors (pinhole/fiber/PMT) to be saved in the computer.

The confocal system is configured for reflectance and fluorescence imaging modes. Only reflectance mode was used in this work. There are three channels, two reflectance imaging channels and one fluorescence channel. Two lasers: blue Argon-ion (Ar) laser (Melles Griot 35LAL-415-220R, 200mW) of 488nm (element number 33 in figure 4.1 and red Helium-Neon (HeNe) laser (Melles-Griot 05-LHP-201, 5.6mW) of 632.8nm wavelength (32) comprise the reflectance channel. The fluorescence channel is configured with Argon laser as the excitation source and the fluorescence signal above the 500nm is detected (except the 632.8nm HeNe excitation is blocked by a chromatic filter). The Ar-laser was used as the fluorescence excitation source as it is optimal for imaging green fluorescent protein (GFP) and also appropriate for reflectance imaging as it provides strong scattering from

tissues.

The Argon and HeNe excitation light is combined at the dichroic mirror (21). The back-propagated (reflected and fluorescence) light from the tissue is deflected into corresponding detectors. The band-rejection filter (8) (Chroma Z488/633) transmitted the 488nm and 633nm bands and diverted the green fluorescence into the fluorescence detection arm (10, 11, 12). An excitation filter (Omega XR3000, Optical density at 488nm = 10^{-6}) was placed before the fluorescence detection pinhole to block the 488nm excitation light (9). The reflected light from Argon and HeNe transmitted through Z488/633 (8) is diverted by the 50/50 beam-splitter into the reflection detection arms. The cube beam-splitter in the original system was replaced by a plate beam-splitter (13) with anti-reflection coating. The reduced the optical noise in the system due to reflections from the beam-splitter. The blue and red reflectance signal were split by the dichroic mirror (4) into the respective pinhole/fiber/detector assemblies. In this way the three signals were separated and detected.

The pinhole radius (R_{ph}) in a confocal system set equal to the radius of the central maxima of the Airy pattern projected by the tube lens at the plane of the pinhole. The radius of this Airy pattern is equal to the product of the magnification of the system and the lateral resolution of the objective lens. The lateral resolution of th objective lens is given by $\Delta x = 2c\lambda/NA$ where c is 0.61 for incoherent light and 0.82 for coherent light and 0.46 for laser beam with Gaussian radial profile [66]. The magnification of the system depends on the objective lens (2), the scanning relay lens (4, 5), and the tube lens (10, 15, 18) focusing the signal into the pinhole. The system magnification in the reflectance channel is 73 and fluorescence channel is 43 [1]. This makes the radius of central disc of the Airy pattern at the plane of the pinhole to be 36 μm and 47 μm for blue and red reflectance channels respectively. So, a 50 μm pinhole was used, which was slightly larger than the focal spot at the

pinhole plane. The light from the pinhole was coupled into a 200 μm optical fiber and connected to the detector.

The system is configured to either detect the two reflectance channels simultaneously or detect the blue reflected signal and the green fluorescence signal simultaneously. The signal from the red reflectance and the green fluorescence optical fiber are coupled into the same detector. Photo-multiplier tubes (PMT: 5773-01, Hamamatsu Photonics, Japan) were used as the detectors. The electrical circuit that runs the PMT is shown in figure 4.2. A variable resistor, (R) is used to control the gain of the PMT module. A multi-contact switch with 10 different resistance values was built to manipulate the control voltage between 0.25V and 0.9V. The relation between the gain control switch and the gain is shown in Table 4.1. The signal output of the PMT is connected to trans-impedance preamplifier (Model: C7319, Hamamatsu Photonics, Japan) for current-to-voltage. The preamplifier has the additional gain setting from 10^5 to 10^7. A custom-built preamplifier used in previous version of the confocal system was replaced with the C7319 preamplifier that reduced the electronic noise in the system.

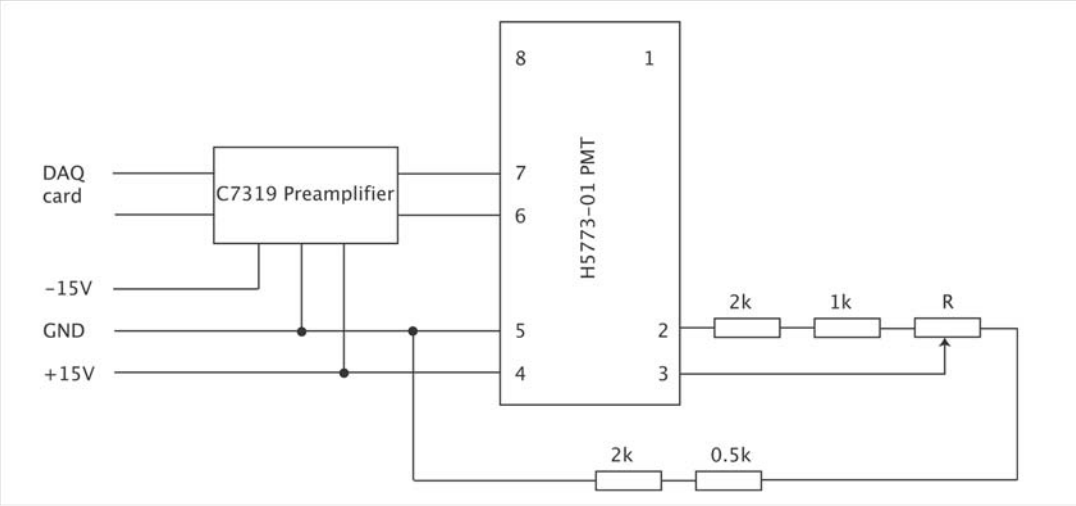

Figure 4.2: PMT gain and trans-impedance amplifier circuit

Table 4.1: Relation between the gain control switch position and corresponding gain of the PMT module.

Switch Pos.	PMT Gain
1	$1.5 \cdot 10^2$
2	$5.0 \cdot 10^2$
3	$1.5 \cdot 10^3$
4	$4.0 \cdot 10^3$
5	$8.0 \cdot 10^3$
6	$1.8 \cdot 10^4$
7	$6.0 \cdot 10^4$
8	$2.0 \cdot 10^5$
9	$5.0 \cdot 10^5$
10	$1.0 \cdot 10^6$

The system is controlled and operated by software developed in LabVIEW^{TM} (National Instruments, Austin, TX). Two programs were developed exclusively to operate the rCSLM system. A program (Scan.vi) was written to survey the tissue and select a region in the sample to image (figure 4.3). A different program (Stack.vi) was developed to acquire data from the tissue. This program can acquire data simultaenously from two reflectance channels or from blue reflectance and green fluorescence channels (figure 4.4). The field of view of the image can be controlled by the user input: "Scan Angle", which is the functional zoom of the system. The software is designed to acquire one X-Y scan (slice) at a time. Then the z-stage steps into the sample along the optical axis. Three-dimensional image data is acquired as a set of XY-scans. The software creates a directory and saves all the XY-scans in the directory. The data from individual XY-scans are formatted and saved as 3D array using MATLAB^{TM} (Mathworks, Natick, MA) for further analysis.

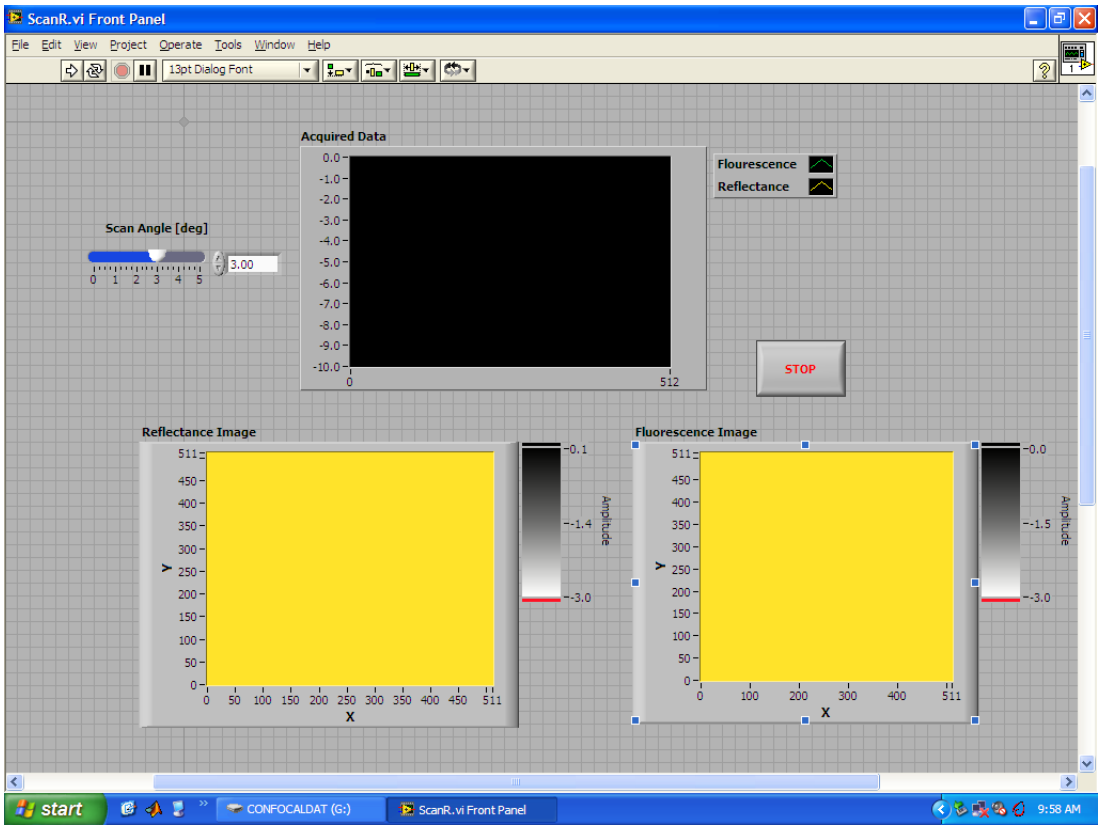

Figure 4.3: Screen shot of the front panel of the Scan.vi function designed to survey the sample and determine the imaging parameters. The program runs continuously and the (x,y) location is adjusted by micrometers on the stage, and the z-position is adjusted by the manual adjustment knob on the z-axis stage controller box. The (x,y) location, the total depth and the step sizes to be used are determined using this program.

4.2 Calibration of theoretical model using tissue phantoms

Optical tissue phantoms are generally used to validate theoretical models [67]. Here, we used optical phantoms made from polystyrene microsphere suspensions to test the (μ, ρ) model developed for the rCSLM system. Microsphere phantoms are used because the theoretical optical properties of the phantom can be computed using Mie solution to the Maxwell's equation that describes the scattering of electromagnetic radiation by a sphere, addressed as Mie theory in this report.

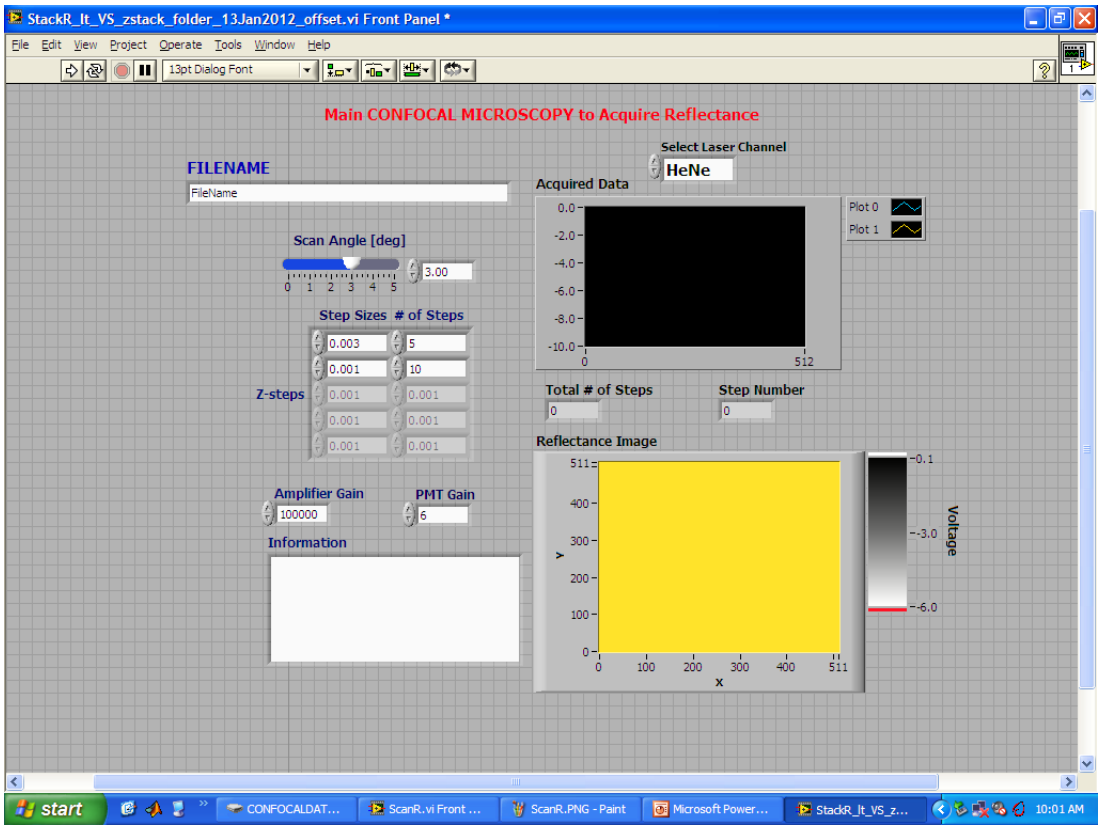

Figure 4.4: Screen shot of the front panel of the Stack.vi program designed to operate and acquire 3D data from rCSLM. The field of view is set by changing the 'Scan Angle [deg]' value. The step sizes and the corresponding number of steps is set. The user inputs the filename, scan angle, PMT gain, and any comments about the data (in Information box). The program creates a directory with 'filename' and saves the all the user inputs in a text file and saves individual slices in the same directory. Later these slices are processed using MATLAB^{TM} and saved as 3D array for further processing.

According to Mie theory, scattering coefficient and anisotropy of scattering are a function of diameter of the spheres, wavelength of the light, and relative refractive index of the sphere to the refractive index of the medium [6]. The scattering coefficient (μ_s) of the microsphere phantom is dependent on the volume fraction of spheres and size of the spheres. But, the scattering anisotropy (g) is dependent on the diameter (or circumference) of the microspheres relative to the wavelength of the light (λ). In this work, 0.1 μm diameter microsphere suspensions were used

as standard tissue mimicking phantom. Tissue phantoms were made with different concentrations of spheres suspensions and measured to validate the model to measure different scattering coefficients (μ_s) values. We also used microspheres of different diameters to validate the theoretical model to measure different scattering anisotropy, g values.

4.3 Materials and Methods

4.3.1 Materials

Polystyrene microspheres samples were procured from Polysciences Inc. (Polysciences, Inc. Warrington, PA). Spheres of different diameters were used that have different scattering anisotropy (g). The diameters of the spheres used were 0.1, 0.14, 0.17, 0.20, 0.26, 0.36 μm. Table 4.2 show the sizes and the respective anisotropy values of the spheres used in this study determined by Mie theory [68]. All the spheres samples were provided as 10% v/v aqueous suspensions. Concentration of the sphere suspensions was adjusted such that the scattering coefficient (μ_s) of the phantoms with different sphere size is same. The phantoms were prepared such that they have a theoretical scattering coefficient of $\approx 60\ cm^{-1}$ determined by Mie theory (μ_{s_Mie}). The scattering coefficient (μ_s) of 60 cm^{-1} was selected as it gives a mean free path ($mfp = 167\mu m$) approximately equal to the thickness of the cover-glass spacer used in the collimated transmission experiment and where the transmitted light undergoes one scattering event. De-ionized water was added to control the concentration of the sphere solution to achieve desired concentration (Column 2 in table 4.2). Stock solutions of required concentration were prepared for sphere solution of each diameter. These stock solutions were used both in collimated transmission measurements and the rCSLM measurements.

To validate the model to measure different scattering coefficient (μ_s), micro-

Table 4.2: Table with experimental parameters to validate theoretical model at different scattering anisotropy, g, (i.e. different sphere diameters). The refractive index of polystyrene spheres is 1.6035 at 488nm, while that of water is 1.3374.

Diameter of sphere (μm)	Concentration (v/v)%	g_{Mie} [-]	g_{Model} [-]	μ_{s_Mie} (cm^{-1})	μ_{s_trans} (cm^{-1})	$\mu_{s\_confocal}$ (cm^{-1})
0.1	2	0.1293	0.11±0.01	59.8	43.8	40.1±4
0.14	0.9	0.2603	0.27±0.02	59.6	53	49±2
0.17	0.625	0.3923	0.41±0.01	59.5	46	48±1
0.2	0.5	0.5377	0.59±0.03	61	70.6	70±10
0.26	0.3	0.7107	0.79±0.01	56	116	120±10

spheres suspension phantoms were made with 0.1 μm diameter microspheres as a standard size. Table 4.3 shows the scattering coefficients, the concentration of spheres suspension used in the study and the optical properties of the phantoms determined from rCSLM signal ($\mu_{s\_confocal}$). Stock solutions of the predetermined concentrations were prepared. The stock solution were sonicated for 10 minutes and used in collimated transmission and rCSLM experiments. The actual scattering coefficient of the stock solution was measured by collimated transmission experiment (μ_{s_trans}), column 6 of table 4.3. The same stock solution was used in the confocal system to acquire 3D data from the sample. Variable step size was used to decrease acquisition time and image deeper into the tissue phantom.

4.3.2 Methods

Collimated Transmission Measurement

Collimated transmission measurements were done to determine the experimental scattering coefficient (μ_s). The scattering coefficient (μ_s) measured by collimated transmission measurement was often different from the theoretically calculated value due the errors in sample preparation and changes in the initial concentration of the spheres suspension. The apparent scattering coefficient of the microsphere

Table 4.3: Table with experimental parameters to validate theoretical model at different scattering coefficient, μ_s, values. The refractive index of polystyrene spheres is 1.6035 at 488nm, while that of water is 1.3374.

Diameter of sphere (μm)	Volume Fraction (v/v)%	g_{Mie} [-]	g_{Model} [-]	μ_{s_Mie} (cm^{-1})	μ_{s_trans} (cm^{-1})	$\mu_{s\_confocal}$ (cm^{-1})
0.1	0.33	0.1293	0.17±0.05	10	11.4	8.8±2
0.1	0.67	0.1293	0.1±0.05	20	22.2	19±2
0.1	1.34	0.1293	0.12±0.03	40	38.6	36±3
0.1	2.0	0.1293	0.18±0.06	60	53.8	54±4
0.1	2.68	0.1293	0.15±0.05	80	68.2	79.5±7
0.1	3.35	0.1293	0.11±0.04	100	82.5	82±3

phantoms were determined experimentally by collimated transmission experiment (μ_{s_trans}). The stock solution was sonicated for 10 minutes to avoid aggregation before preparing the phantoms. Phantoms were made by having the sphere suspensions of required concentration sandwiched between a pair of glass slides with cover slip as the spacer for transmission experiment. So, the thickness of the phantom was equal to the thickness of the cover slip (150 μm). The transmitted light through the sample (T_{sample}) and through water (T_{water}) was recorded. Scattering coefficient (μ_s) was calculated using Beer's law (equation 4.1).

$$\mu_s = -\ln\frac{\left(\frac{T_{Sample}}{T_{water}}\right)}{t_{cs}} \tag{4.1}$$

where t_{cs} is the thickness of the sample, i.e., the thickness of the cover-glass ($\approx 150\mu m$).

The Argon laser ($\lambda = 488nm$) used in the confocal system was diverted into a collimated transmission system for ballistic transmission experiments. The diameter of the beam was 1 mm. The laser was modulated at 700 Hz by a chopper and transmission was detected using a lock-in amplifier (Standford Research Systems, SR830) for higher sensitivity. A photodiode (DET216, ThorLabs Inc) was used as

the detector.

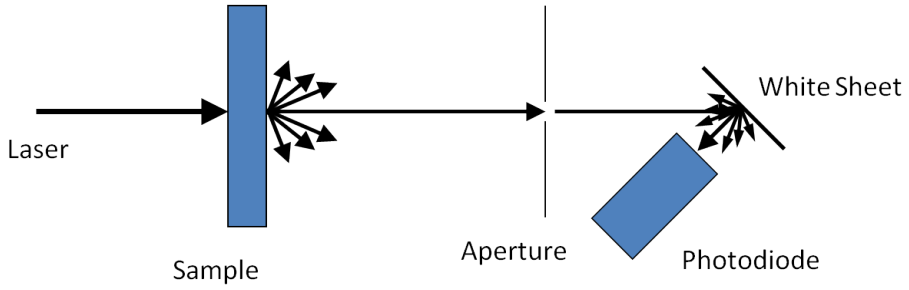

Figure 4.5: Schematic of the collimated transmission experiment.

The same stock solution was used to make phantoms for rCSLM imaging. The phantoms were made by having the sphere solution sandwiched between two cover slips and a glass slide was used as a spacer. The sandwich was made using a cover glass to minimize the amount of glass between the objective lens and sample. The sample was coupled to the objective lens with water. X and Y-axis scanning mirrors captured a 512 x 512 pixel image at each depth while the z-axis stage stepped through the sample acquiring a 3D image, M(x,y,z) of the sample. The pixel size was 0.31 μm x 0.31 μm, while the step size in the z-axis was varied at different locations in the sample to reduce the acquisition time and get reliable data. The step size of 1 μm was used near the glass-sample interface and a step size of 10 μm was used as the focus moved deep into the homogeneous sample. The focus was scanned from glass through the glass-sample interface into the sample.

4.3.3 Analysis

The signal $M(z)$, as a function of depth was determined by averaging a neighborhood of 10 x 10 pixel centered around the (x,y) point of interest in the acquired 3D image, $M(x, y, z)$. The pixel values for M(z) were converted to reflectance units, $R(z)$, by $R(z) = calib\, M$, where $calib = \frac{R_{wg}}{M_{wg}}$, and M_{wg} was the measurement of a water-glass cover slip interface and R_{wg} was the value reflectance from the water-

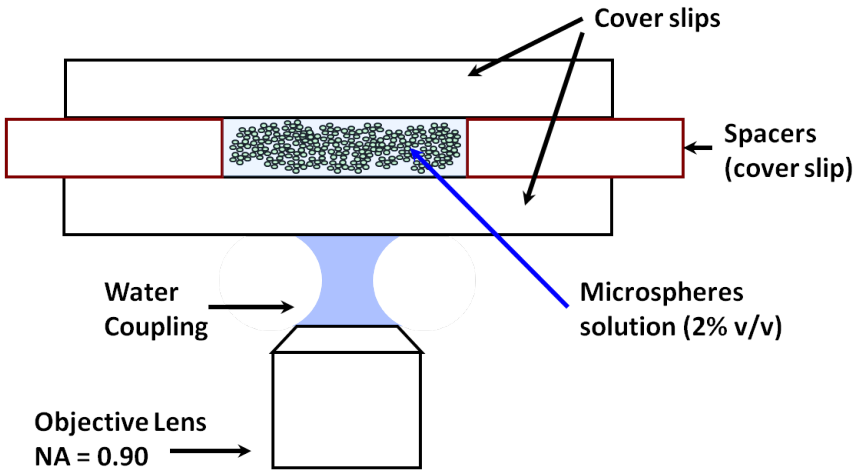

Figure 4.6: Illustration of the microsphere phantom arrangement (Not to scale). A sandwich of cover-glass was used with cover-glass spacer (for collimated transmission experiment) or glass slide spacer (rCSLM measurement) were used to control the thickness of the sample.

glass interface calculated by $[\frac{(n_1-n_2)}{(n_1+n_2)}]^2 = 0.0045$ where $n_1 = 1.337$ (refractive index of water) and $n_2 = 1.53$ (refractive index of the cover glass) at 488 nm. Figure 4.7 shows an example of the microspheres phantom data acquired with rCSLM system. Figure 4.7A shows an XZ slice of the 3D data from 0.1 μm diameter sphere suspension of 2 % V/V concentration. Figure 4.7B shows the rCSLM signal as a function of depth. The signal $M(z)$ is plotted on a semi-log plot which shows the exponential decay of the rCSLM signal with depth. The signal at each pixel is displayed by blue line, while the mean of 10 x 10 pixel taken at each z position is displayed as red circles. The noise floor of the system is 5 x 10^{-3}V as shown in the figure 4.7B. The system has a dynamic range of 3 order of magnitude.

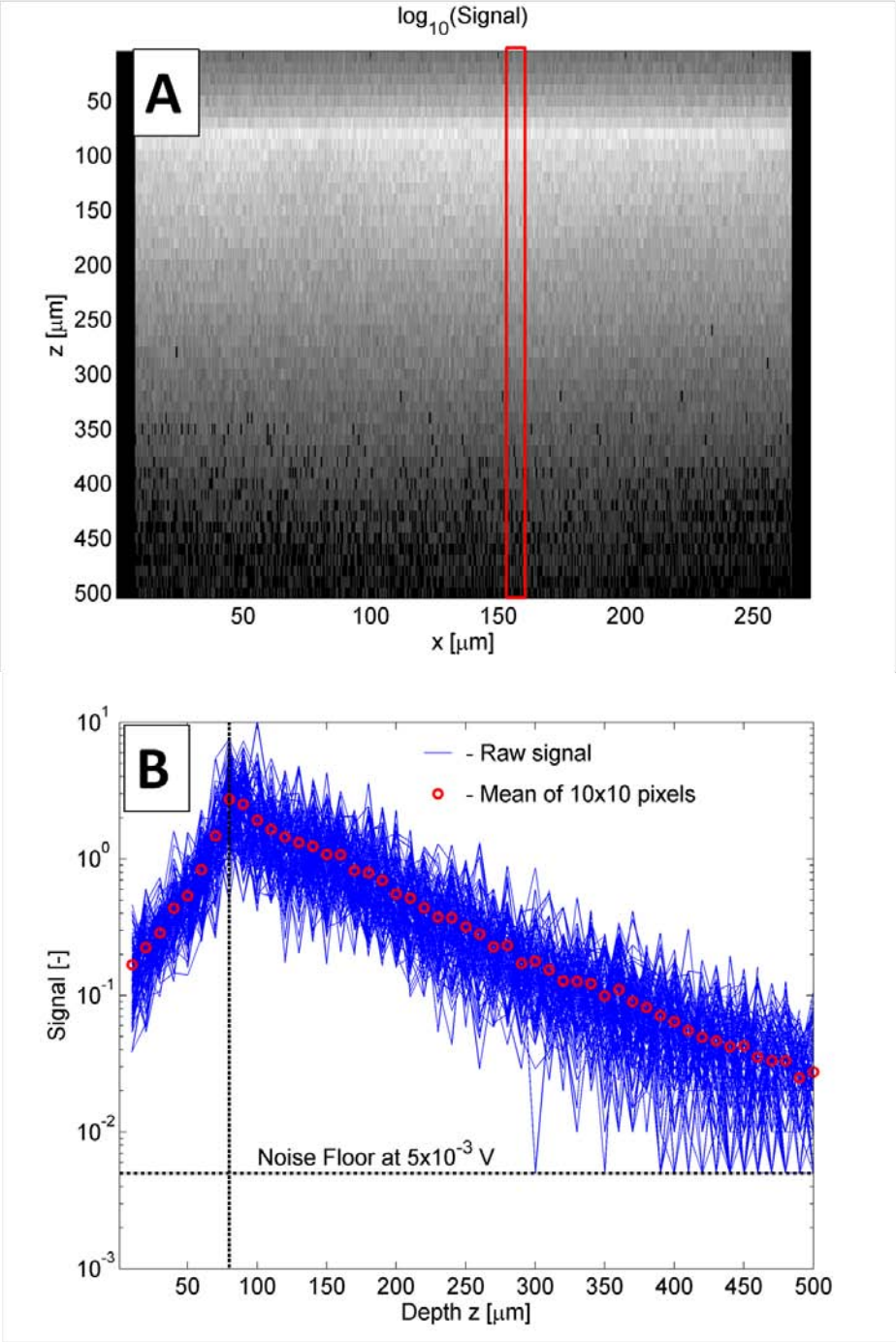

Figure 4.7: (A) An XZ slice of the microsphere phantom made of 0.1 μm diameter microspheres at 2 % v/v concentration. (B) A semi-log plot shows the rCSLM signal as a function of depth. Blue line is the raw signal at each pixel. The population blue lines represent the 10 x 10 pixels averaged to obtain the mean signal with respect to depth (z) displayed by red circles. The raw signal and mean signal follows an exponential decay function. The noise floor of the system is 5 x 10^{-3}V.

The reflectance $R(z)$ at each x,y position was fit with an exponential decay function (equation 4.2), characterized by two parameters, ρ and μ.

$$R(z) = \rho e^{-\mu z} \tag{4.2}$$

Optical properties of scattering, the scattering coefficient (μ_s) and the scattering anisotropy (g), of the phantoms were specified by using the theoretical model presented in chapter 3, that maps the experimental parameters of μ and ρ to optical properties of μ_s and g by the following equations:

$$\mu = a(g)\mu_s 2G(g, NA) \tag{4.3}$$

$$\rho = \mu_s \Delta z b(g, NA) \tag{4.4}$$

where Δz is the axial resolution of the objective lens. It defines the region at the focus of the objective lens from where the scattered light is collected. It is given by $\Delta z = f\frac{1.4n\lambda}{NA^2}$, where the λ is the wavelength ($\lambda = 488$nm), n is the refractive index of the coupling medium ($n_1 = 1.3371$ for water), f is the axial calibration factor to calculate the apparent axial resolution of the system, and NA is the numerical aperture of the objective lens (NA = 0.9). The axial calibration factor was 5.5 for the microsphere calibration experiments. The f scales the theoretical axial resolution and causes the analysis grid to move on ρ-axis. The product $\mu_s\Delta z$ specifies the average number of scattering events at the focus of the objective lens, which is a number smaller than unity as Δz ($1.12\mu m$) is very small compared to the mean free path, $mfp = 1/\mu_s$ (for $\mu_s = 60\ cm^{-1}$; $mfp = 168\ \mu m$) of the phantoms. The (μ, ρ) determined from the experiment were plotted over the grid to specify the optical properties. Refer to chapter 3 for details on $a(g, NA)$, $G(g, NA)$ and

$b(g, NA)$.

4.4 Results

Table 4.2 shows the details of the phantoms and results from the analysis. Different diameter microspheres were used to validate the model on samples that differ in scattering anisotropy (g). The g of the phantoms ranged from 0.12 to 0.71 as determined by Mie theory [68]. The concentration of the spheres suspension was adjusted to give the theoretical scattering coefficient, μ_s, of 60 cm^{-1}. The true μ_s values of the samples determined by collimated transmission experiment (μ_{s_trans}) is given in column 6 of table 4.2. Figure 4.8 shows the scatter plot of the (ρ, μ) values determined by from the least-squares fit of $R(z)$ by equation 4.2 superimposed on the (μ_s, g). Data from samples made from spheres of different diameters are represented by different marker and color superimposed on the (μ_s, g) grid determined by theory. The plot also shows the mean of the (μ, ρ) values ($\diamond$). The value of μ_s determined by collimated transmission and the scattering anisotropy, g value from Mie theory were used in equations 4.4 and 4.3 to calculate the corresponding μ and ρ values. These values are plotted on the grid ($\triangleright$).

Figure 4.9 shows the closeup of the figure 4.8 with the mean of the (μ, ρ) pairs determined from the experiment. The (μ, ρ) values calculated from (μ_s, g) values determined by the combination of Mie theory (g) and collimated transmission (μ_s) experiment are also plotted. The error bars on the rCSLM results represent one standard deviation of the results. As the diameter of the microspheres increased the model over-predicts the value g compared to the value of g computed from Mie theory. But, the scattering coefficient (μ_s) predicted from rCSLM results is comparable to the collimated transmission results. Figure 4.10 compares the scattering anisotropy values determined from rCSLM + theoretical model (g_{Model})

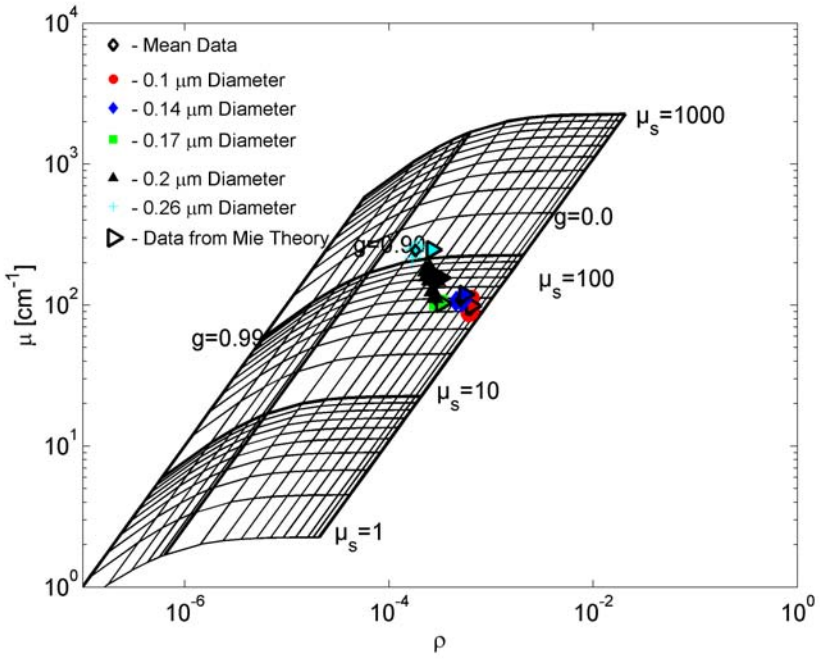

Figure 4.8: Plot of the experimentally (filled markers) determined μ and ρ data pairs and corresponding values calculated from Mie Theory ($\triangleright$) for different diameter spheres superimposed on the (μ_s, g) grid. Data from different spheres diameter is represented by different color and markers. The plot also shows the mean of the μ and ρ ($\diamond$). Data with $\triangleright$ marker is calculated from g determined by Mie theory and μ_s determined by collimated transmission experiment.

versus scattering anisotropy determined from Mie theory (g_{Mie}). The data falls on the identity line (dotted line) that shows the agreement between g_{Model} and g_{Mie}. A good agreement between the theoretical values and the experimental values of g was observed for smaller diameter spheres (0.1 *and* 0.14μm diameter spheres). The scattering coefficient (μ_s) of 0.26 μm diameter showed unusually high value than the expected 60 cm^{-1}. This can be due to the error in the sample preparation caused by the small concentrations involved. Collimated transmission measurements were employed to determine the actual scattering coefficient (μ_s) of the sample, which are in agreement with the results from rCSLM measurements.

Figure 4.11 shows the results from experiments to various the model to predict change in scattering coefficient (μ_s). 0.1 μm diameter microsphere suspension

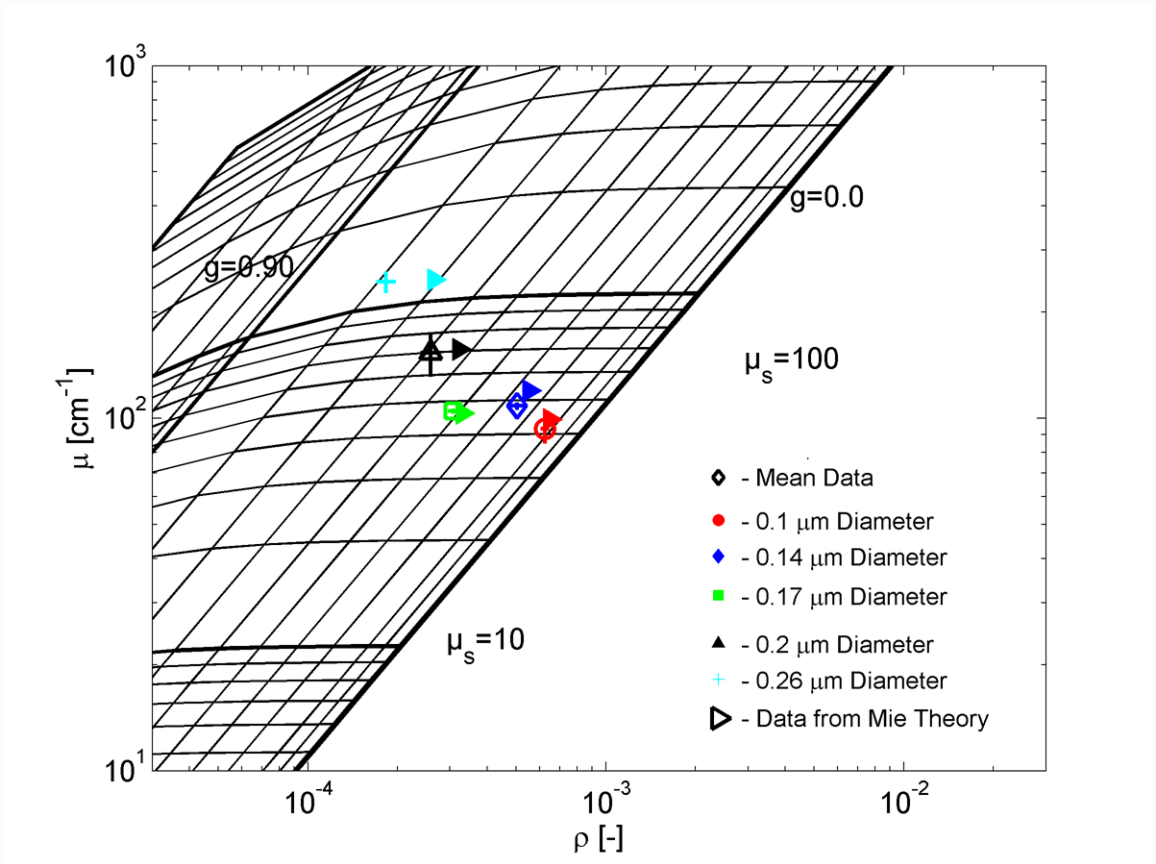

Figure 4.9: Close-up of figure 4.8 to show the variation in the μ and ρ and their relation to the values ($\triangleright$) determined by Mie theory and collimated transmission.

was used as a standard, and the concentration was manipulated to get a range of scattering coefficient values (Table 4.3). The plots are analogous to figure 4.8 in terms of the color and marker scheme used. The concentration of the sphere suspension required to give scattering coefficient of [10 20 40 60 80 100]cm^{-1} was calculated using Mie theory, denoted as μ_{s_Mie} in table 4.2. But, as mentioned earlier the μ_s of the stock solution of the samples were measured using collimated transmission experiment, denoted μ_{s_trans}, which were considered to be the actual μ_s of the samples (Column 6 in table 4.3). Figure 4.11 also shows the mean of the (μ, ρ) data and the values determined from Mie theory values similar to figure 4.8. As the concentration of the sphere suspensions increased the μ_{s_trans}

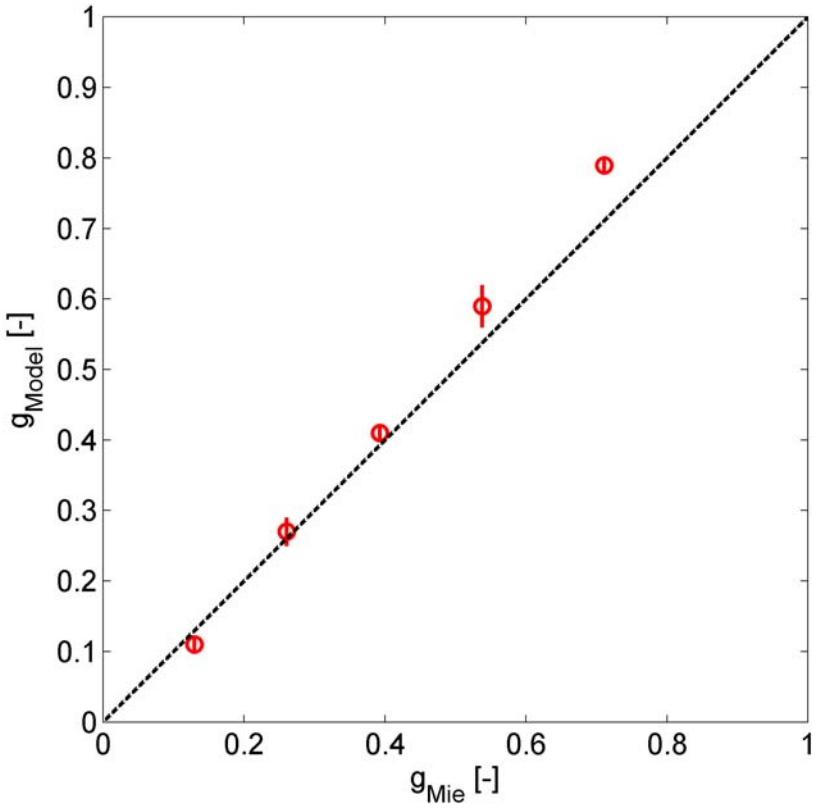

Figure 4.10: Plot to compare the scattering anisotropy determined by rCSLM (g_{Model}) and Mie theory (g_{Mie}). Error bars in the vertical direction represent $\pm$ 1 standard deviation. The identity line (dotted line) shows the agreement between g_{Mie} and g_{Model}.

decreased compared to μ_{s_Mie}. But, the μ_s predicted by the model $\mu_{s\_confocal}$ are in agreement with μ_{s_trans}. All the data falls on the $iso-g$ lines which is expected as only one diameter ($0.1\mu m$) microspheres were used in the study. This shows the model is sensitive to the g of the sample.

Figure 4.12 shows the close-up of figure 4.11 to have a better view of the differences between the μ_{s_trans} and $\mu_{s\_confocal}$ data, where the mean of (μ, ρ) are plotted along with (μ, ρ) predicted from a combination of Mie theory (to find g) and transmission experiment (to find μ_s). Figure 4.13 plots the scattering coefficient values determined from the theoretical model ($\mu_{s\_confocal}$) versus scattering coeffi-

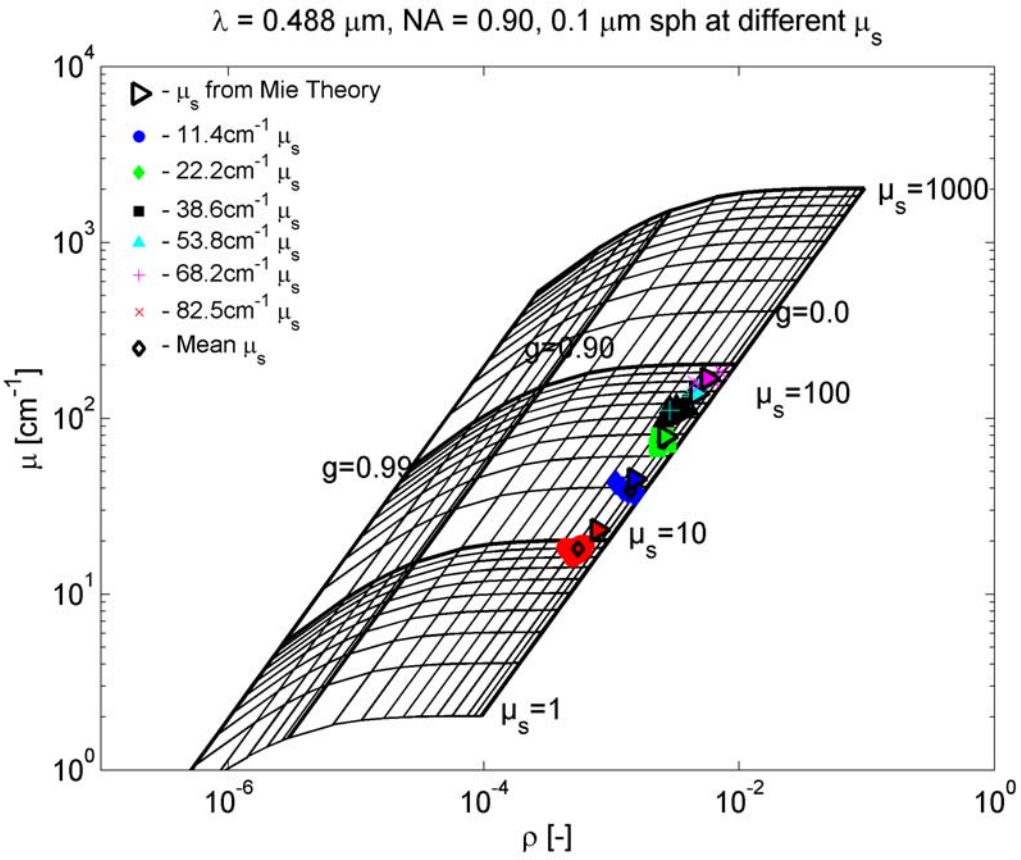

Figure 4.11: Plot of the experimentally (filled markers) determined μ and ρ data pairs and corresponding values calculated from Mie theory($\triangleright$) for 0.1 μm diameter spheres with different scattering coefficient, μ_s, superimposed on the (μ_s, g) grid. Data from different μ_s is represented by different color and markers. The plot also shows the mean of the μ and ρ ($\diamond$). Data with $\triangleright$ is calculated from g determined by Mie theory and μ_s determined by collimated transmission experiment.

cient determined from transmission experiment (μ_{s_trans}). The data falls around the identity line (dotted line) that shows that the agreement between $\mu_{s\_confocal}$ and (μ_{s_trans}) values. A good agreement between the theoretical values and the experimental values of μ_s was observed, except for sample at μ_{s_Mie} of 80 cm^{-1}.

The above experiments describe the validation of the theoretical model to determine optical properties of scattering using tissue phantoms made from microsphere suspensions. This report addresses the ability of the model to predict differences in the scattering anisotropy (g) and scattering coefficient (μ_s) of the tissue phan-

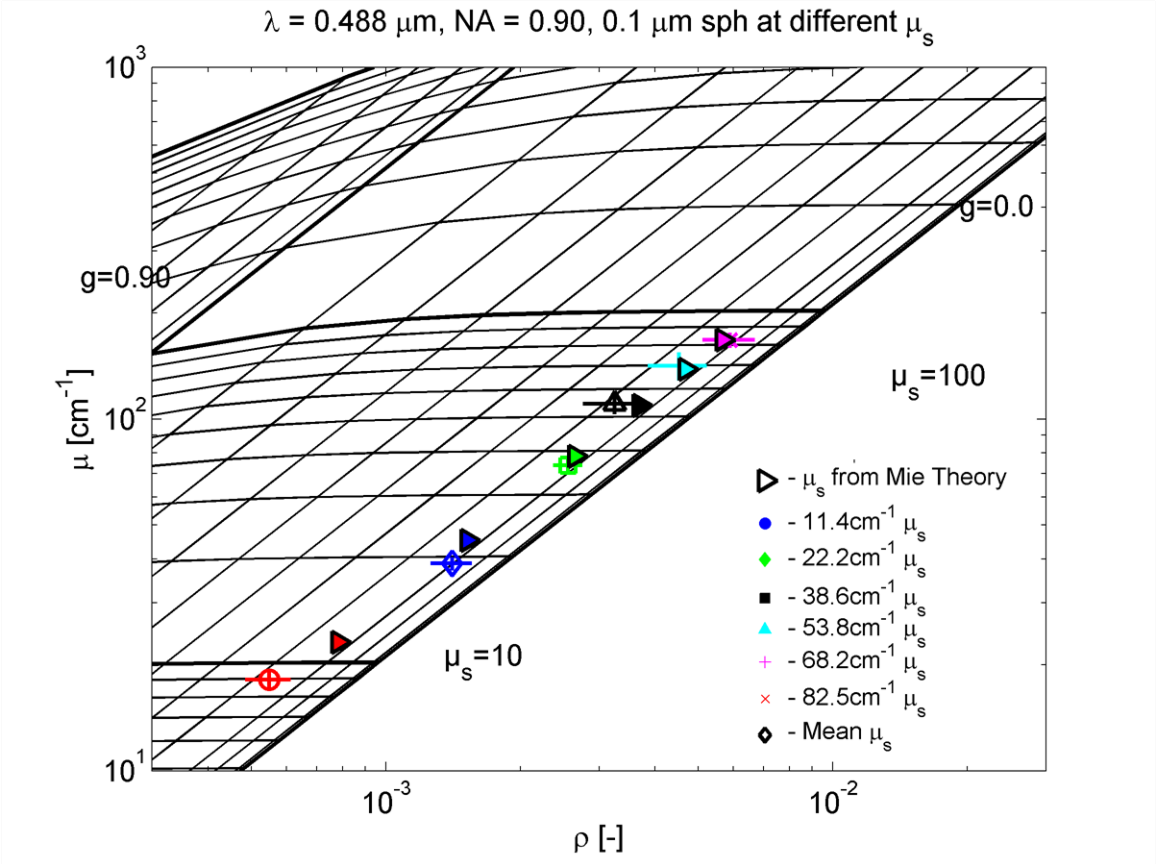

Figure 4.12: Close-up of figure 4.11 to show the variation in the μ and ρ and their relation to the values ($\triangleright$) determined by the combination of Mie theory and collimated transmission.

toms. The experimentally determined scattering anisotropy values (g_{Model}) were compared with scattering anisotropy (g_{Mie}) values determined using Mie theory (figure 4.10). The model predicted the scattering anisotropy of microsphere phantoms with in an error of $\pm 5\%$. The concentrations needed to make phantoms of desired scattering coefficient is very small for larger diameter microspheres. Error in sample preparation cause the actual μ_s to be different from the expected μ_s. The model was also validated by measuring phantoms of different with different scattering coefficients (μ_s) values. The model predicted μ_s values within an error of 10 % (figure 4.13). Aggregation of spheres was observed at higher concentration of spheres (not included) which might explain the increase of the

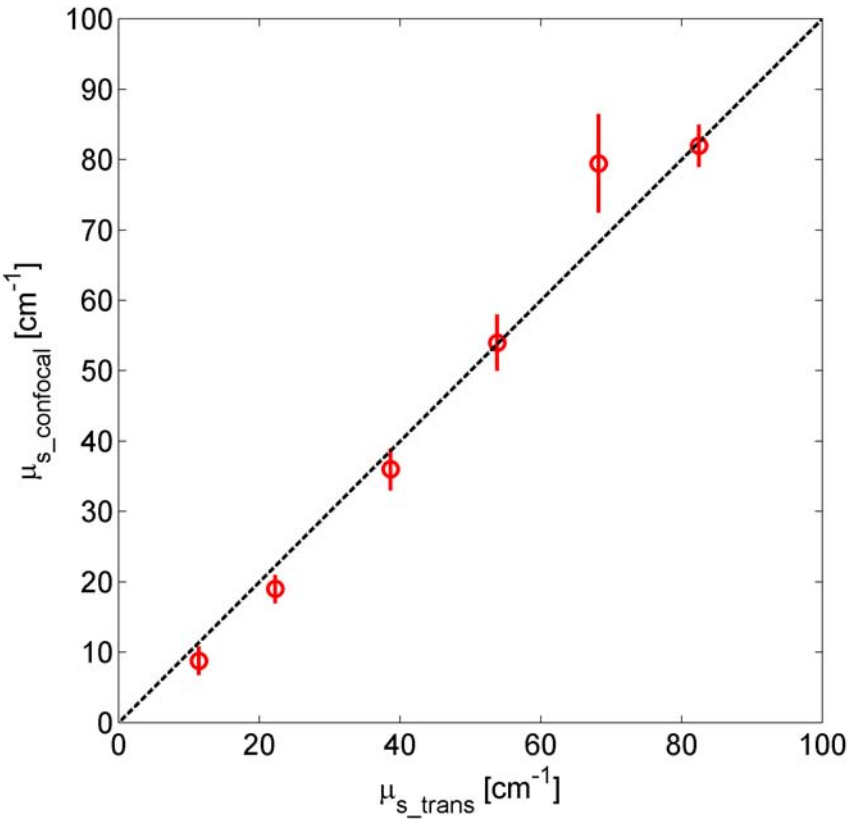

Figure 4.13: Plot to compare the scattering coefficient determined by rCSLM ($\mu_{s\_confocal}$) and by collimated transmission measurement (μ_{s_trans}). Error bars in the vertical direction are represent the standard deviation. The identity line (dotted line) shows the relation between the $\mu_{s\_confocal}$ and μ_{s_trans}.

error in $\mu_{s\_confocal}$ measurements. The model was also validated with microsphere phantoms with added absorber [69] (not shown here). The model predicted the absorption coefficient (μ_a) of the phantom, when scattering coefficient is known. Subsequent chapters describe application of the theoretical model. Optical properties of commercially available tissue phantoms and reflectance standards were determined using the model (chapter 6). Chapter 5 describes determination of optical properties of murine tissues.

Chapter 5

Determination of optical scattering properties of murine tissues by rCSLM

Introduction

Interaction of light with tissue (propagation, thermal, etc) are characterized by optical properties summarized in table 2.1 in chapter 2. These optical properties are necessary to describe the propagation of light in media (tissue, atmosphere etc). Light transport and energy deposition in tissue are affected by the optical properties: scattering coefficient (μ_s), scattering anisotropy (g) and absorption coefficient (μ_a). Scattering coefficient affects the amount of light energy reaching a point in the tissue, while the absorption coefficient (μ_a) affects the amount of light energy deposited at a point in the tissue. Performance of laser therapeutic techniques like photodynamic therapy (PDT) depends on the amount of light energy deposited at the site of interest in the tissue, which can be analyzed by knowing the optical properties of tissues. So, optical properties are needed to effectively use the light for diagnostics and therapeutics.

This chapter describes determination of optical properties of mouse tissue. The goal was to estimate optical properties of different tissue types and study differences

between them. Five different tissues types were studied. The tissue types studied were: brain white matter, brain gray matter, liver, muscle and skin.

5.1 Materials and Methods

5.1.1 Materials

Five different tissue types were used in this study. SKH-1 hairless mice, 3-4 week old were euthanized. Brain, Skin, Liver and Muscle tissues were freshly excised. Gray and White matter of the brain were separated and imaged separately. The skin tissue was excised from abdominal side of the mouse. Hairless mice were chosen to avoid artifacts from shaving to remove hair from the skin. Tissues were used fresh with no processing. The tissues were imaged within 3 hours. Brain tissues were imaged immediately after excision. All animal studies were approved by the Oregon Health and Science University Institutional Animal Care and Use Committee.

Two experiments were performed, which differed in the way the extracted tissue were handled. In the first experiment seven mouse (addressed as 'set 1') were used, where the excised tissue placed on a tissue paper soaked in phosphate buffered-saline (PBS) at room temperature. The tissue was contact with PBS during the experiment. In the second experiment, five mouse (addressed as 'set 2') were used, where the excised tissue was stored in a test tube with a tissue paper soaked in PBS at the bottom and tissue was placed such that it did not contact the tissue paper. The test tubes were stored in ice.

Microsphere suspensions were used to calibrate the confocal system for each experiment. 0.1 μm diameter microsphere suspension procured from Thermo scientific (Model: 5010B) were used. A 2% v/v suspension was placed on a sample holder. Sample holder is a sandwich of two 25 mm x 60 mm cover glass with

spacers made of glass slide. The sample was 1-mm thick with a 150 μm cover glass between the coupling medium of the objective and the sample.

5.1.2 Experimental Protocol

The tissue samples were placed on a 1 mm thick metal plate that was manufactured to the specifications (size and shape) of a standard microscope slide. The metal plate had 2-mm diameter hole at the center. Tissues were placed on the hole at the center of the plate and coupled to the objective lens through the hole by gel (GenTeal, Novartis Pharmaceuticals Corp., NJ). The refractive index of gel is similar to water. Using gel as coupling agent avoided problems of loss of coupling fluid during imaging and contamination of the coupling medium by fluids from the tissue (like blood). 3D data was acquired by stepping the z-axis stage through the sample, and the xy-galvo scanning mirrors acquired a 512 x 512 pixel image at each depth. The rCSLM has a sampling rate of 25-kHz, which takes 15 minutes to acquire each 3D data. To minimize acquisition time and increase the depth imaged, variable step sizes were used. A large step size was used to scan through the volume above the sample (region between the tissue and objective lens) and after the focus reached 50-70 microns into the tissue. Whereas smaller step size of 1-μm (generally 50 steps were used) was used at the interface between the tissue and the coupling medium. Depending on the tissue type, the total depth imaged changed and the step sizes were chosen accordingly. Typically the large step sizes were between 2-5 μm. Total depth imaged also increased because of the curvature of the tissue surface.

5.1.3 Data Analysis

The reflectance signal in the rCSLM was acquired as voltages by a PMT, V [Volts], which was stored as a 3-D array, $V(x, y, z)$ from one site per tissue type. The x, y were the lateral directions, and the z was the axial distance of focus in the tissue. Voltages recorded ranged from 0 to 10 V, digitized by a 12-bit A/D converter. The data was recorded as 512 pixels x 512 pixels x Nz pixels, cube; where Nz was the number of steps (70 to 90) used per tissue. As explained the number of steps, Nz, was varied for each sample to optimize acquisition time and total depth captured. The pixel size in the x, y plane was 0.3115 μm x 0.3115 μm.

The pixel values in Volts was converted to reflectance by calibrating against the reflectance from a gel-glass coverslip interface ($R_{gg} = [\frac{n_1 - n_2}{n_1 + n_2}]^2 = 0.0044$, where $n_1 =$ 1.35 (gel), and $n_2 = 1.52$(glass)). The signal from gel-glass coverslip interface (V_{gg}) was acquired with the same gain setting as the tissue. To avoid saturation of the detector a neutral density filter was used during gel-glass cover slip measurement. The $V(x, y, z)$ was converted to reflectance signal by the following equation:

$$R(x, y, z) = V(x, y, z) \ \frac{R_{gg}}{V_{gg}} \tag{5.1}$$

For each dataset, 50 (x, y) locations were randomly selected in the field of view to analyze. A random number genera At each location a region of interest of 10 x 10 pixels around the neighborhood were averaged to obtain an average axial reflectance profile $R(z)$. The region of interest corresponded to 3.1 μm x 3.1 μm x (100 - 150) μm. The tissue surface was irregular due to structure of the tissue, for example hair follicles in the field of view gave bad fits, or due to the mounting of the sample on the microscope. Fits from the irregular surface of the tissue were rejected by the algorithm. Due to difficulty in handling the tissue, the tissue

surface was not flat in x,y direction. This lead to data with insufficient points as a function of depth to fit. Data with at least 10 points to fit were selected for fits. The starting point of the data to fit was chosen 5-μm from the surface to avoid the signal from the tissue-gel interface. Data from few tissues were corrupted as the tissue moved during the imaging, this was due to the use of the gel as coupling medium. As the objective lens was moved closer to the tissue surface, due to the viscosity of the gel instead of the focus moving deeper into the tissue, the tissue was moved and the focus stayed at the same lateral plane in the tissue, that corrupted the data. This problem does not occur with water coupling, though contamination of water by the tissue fragments and blood corrupted the data when imaged with water as a coupling medium.

$$R(z) = \rho e^{-\mu z} \tag{5.2}$$

The axial reflectance profile was modeled as a simple exponential decay equation 5.2. The top of the tissue was found by identifying the peak reflectance. Then the data starting 5 μm from the top of the tissue to the end was fit with equation 5.2. A water-dipping objective lens was used in the rCSLM system, and as the refractive index of the tissue (n = 1.37) is similar to water (n = 1.33), the axial translation of focus is not subjected to refractive index correction 7. In this study gel with refractive index similar to water was used as coupling medium. The optical properties of the tissues were extracted using the model described in chapter 3.

5.2 Results

Figure 5.1 shows the typical *en face* images from each tissue type. Dendritic structures were visualized in the brain gray matter, while axons were visible in the brain white matter. In skin epidermis and dermal regions were observed in sagittal views (not shown) similar to the data presented in literature [5]. The dermis of the skin showed large fiber bundles of collagen distinct from other studies with mouse skin. Probably it is the phenotype of the SKH-1 hairless mouse. Liver was homogeneous with hepatocytes visible with dark nuclei. Several features with high reflectance were also visible between the cells. Muscle tissue images show several fiber bundles randomly oriented in the field of view which was different compared to past studies. Experiments were performed with Argon(488nm) laser. The data from liver was consistent across all the mouse which is evident from the results from the fitting (figure 5.2).

The 3-D data acquired by rCSLM were analyzed as described in methods section. Due to the difficulty in handling the tissues, tissue surface was not flat, rather it was inclined with respect to depth. Due to this, only part of the field of view is in focus per slice and some parts of the image did not have enough depth information to fit. A algorithm was designed to accept the data if there were at least 10 points to fit. 50 depth profiles were randomly picked from each data set and analyzed.

The results from the two sets of mice are presented separately. Figure 5.2 shows the scatter plot of optical properties determined from individual tissue types from set 1, superimposed on the grid. Figure 5.3 shows the scatter plot of the results from the set 2. The variability in the results is related to the tissue structure. The variability of optical properties of liver is small compared to other tissue types. This is due to the homogeneous structure of the liver formed by hepatocytes. Compared to liver all other tissue types have large variation in the optical properties. This

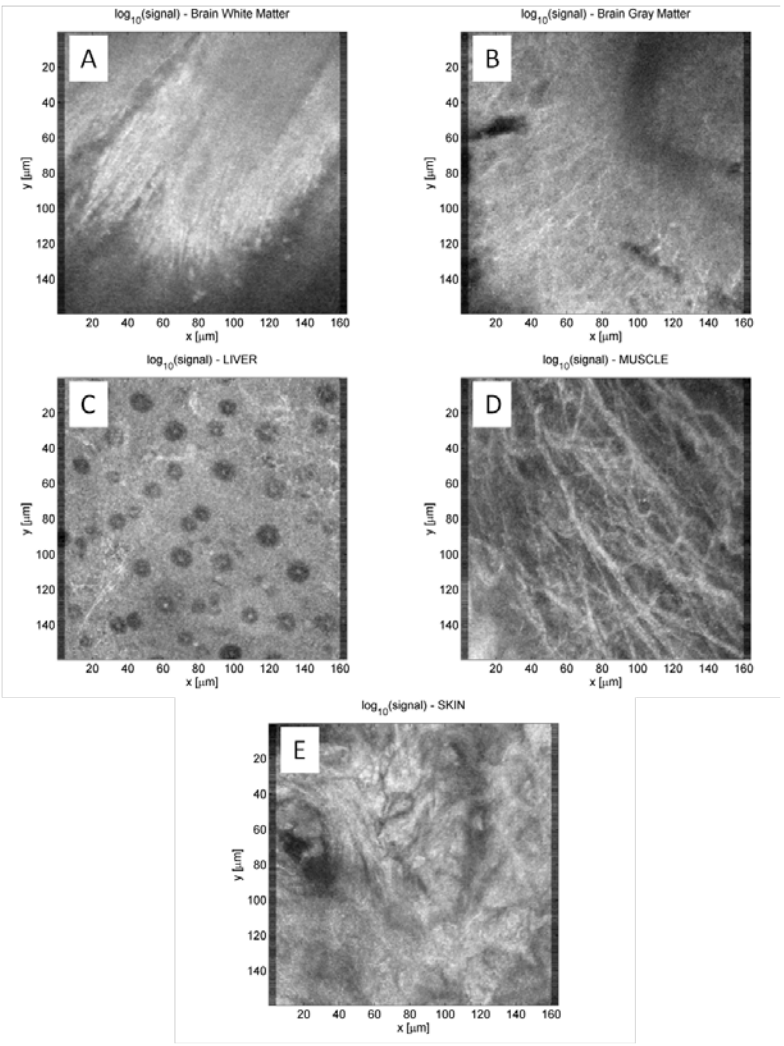

Figure 5.1: Typical *en face* views of the tissues imaged by rCSLM. A) Brain white matter; B) Brain gray matter; C) Liver; D) Muscle; E) Skin.

may be due to the complexity in tissue structure. Fibrous tissue like muscle and skin presented more variability in the results of the fits.

The results from brain gray matter, brain white matter and liver from two both experiments are similar. However, the g values of the muscle tissue from set 1 where the tissue is in contact with PBS, was higher than the muscle tissue in set 2 where the tissue was not in contact with PBS. The results from skin tissue show similar changes. Contact with PBS might be the reason for the difference in the g values between the two sets.

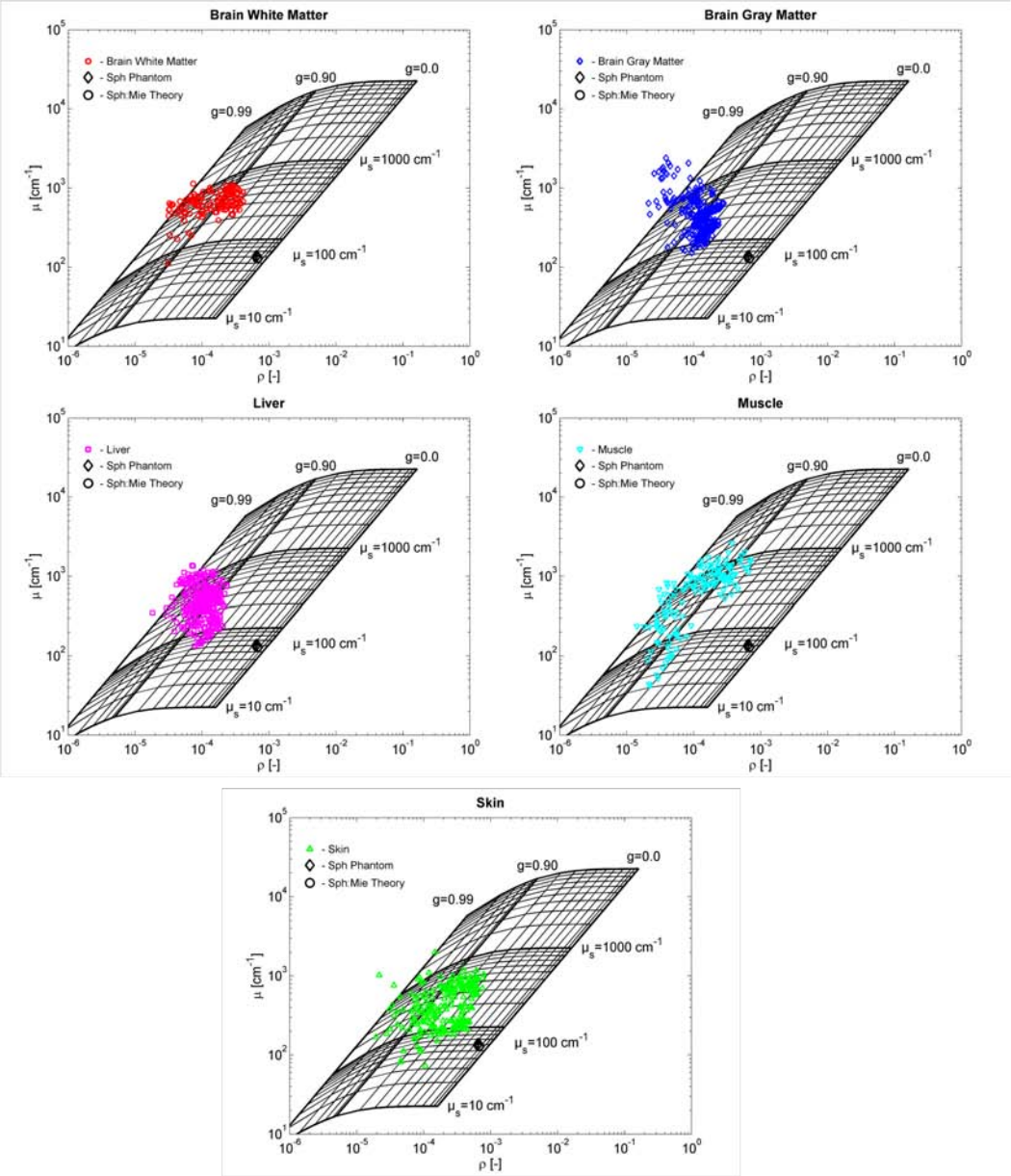

Figure 5.2: The (μ, ρ) values determined from the tissues of mice from set 1, are plotted in the above scatter plot. The tissue was in contact with tissue paper soaked in PBS. Data from each tissue is plotted in a separate figure. The data is superimposed on (μ_s, g) analysis grid. Different tissues are represented by different color and marker. The results from microsphere calibration ($\diamond$) is also plotted on the grid.

Figure 5.4 shows the median of all the μ and ρ values of each tissue type. The data from set 1 show that the anisotropy (g) of the mouse tissue types between

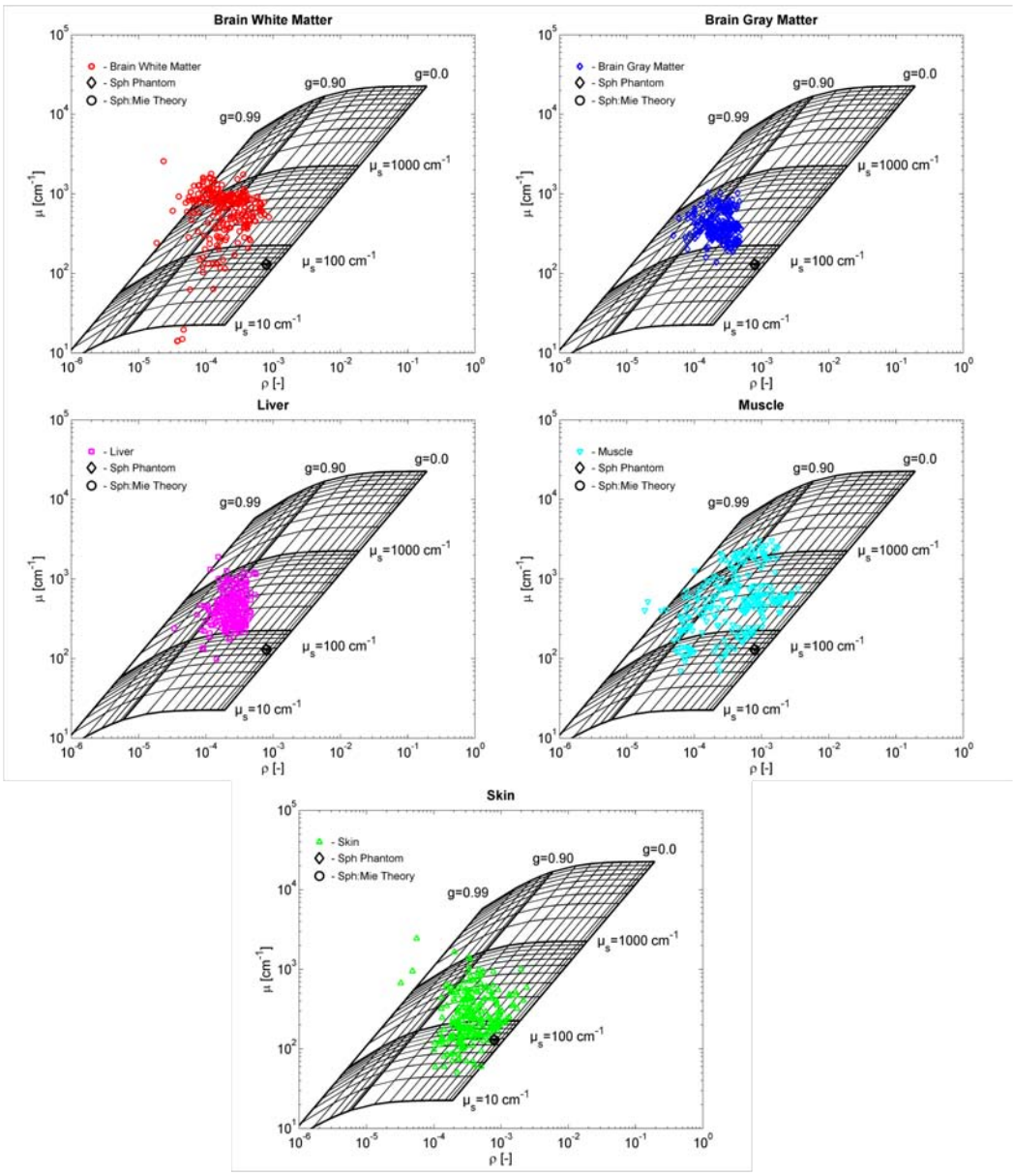

Figure 5.3: The (μ, ρ) values determined from the tissues of mice from set 2, are plotted in the above scatter plot. The tissue was not in contact with PBS. Data from each tissue is plotted in a separate figure. The data is superimposed on (μ_s, g) analysis grid. Different tissues are also represented by different color and marker. The results from microsphere calibration ($\diamond$) is also plotted on the grid.

0.7 and 0.95, while the scattering coefficient (μ_s) between 100 and 800 cm^{-1}. Scattering anisotropy of tissues from set 2 range between 0.6 to 0.95 and the scattering coefficient in the range of 100 to 800 cm^{-1}. The results from the two sets

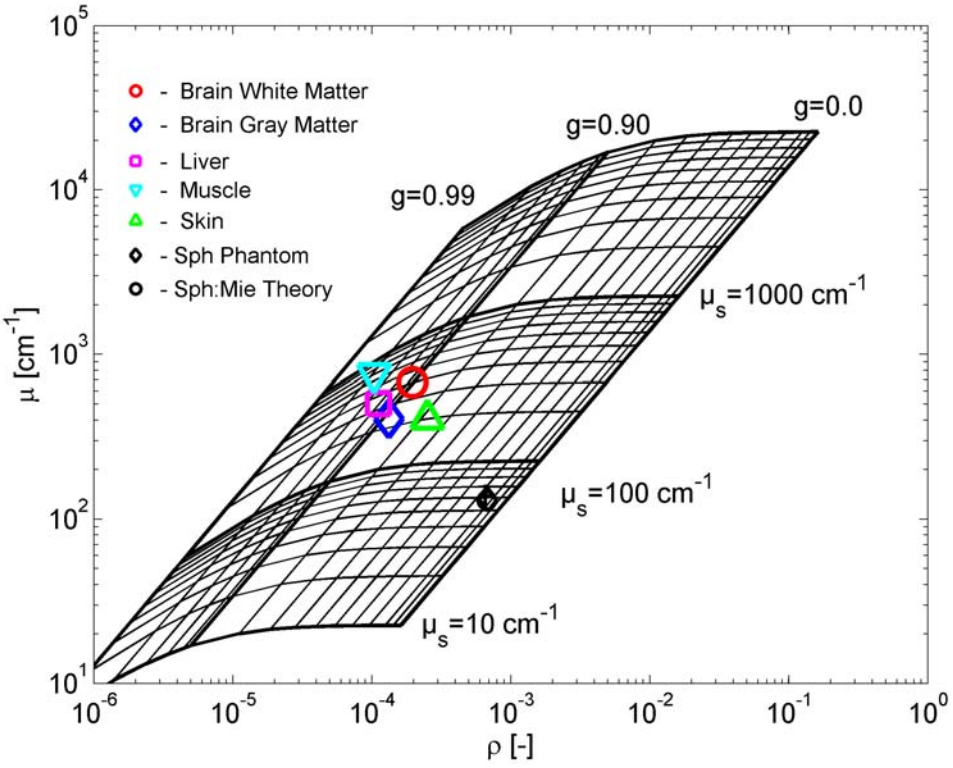

Figure 5.4: The median ρ and μ of the tissue data from set 1 where the tissue is in contact with PBS, are superimposed on the analysis grid.)

of mice are consistent for tissues. The results from muscle for both the experiments had large variability, hence the median value of the set 1 and set 2 differ more than other tissue types. Results from liver and brain gray matter gave consistent results across all mice. The variability in the results is small compared to other tissue types. The results also varied as the region of interests to fit were selected randomly by the analysis algorithm. We believe manual selection of the region of interests with smooth data can improve the results.

This chapter described estimation of optical properties of five murine tissue types using the theoretical model presented in chapter 3. Two sets of mice were used in the study. The results from the two group of mice were consistent. The variability of the results is related to the ultrastructure of the tissue. Homogeneous

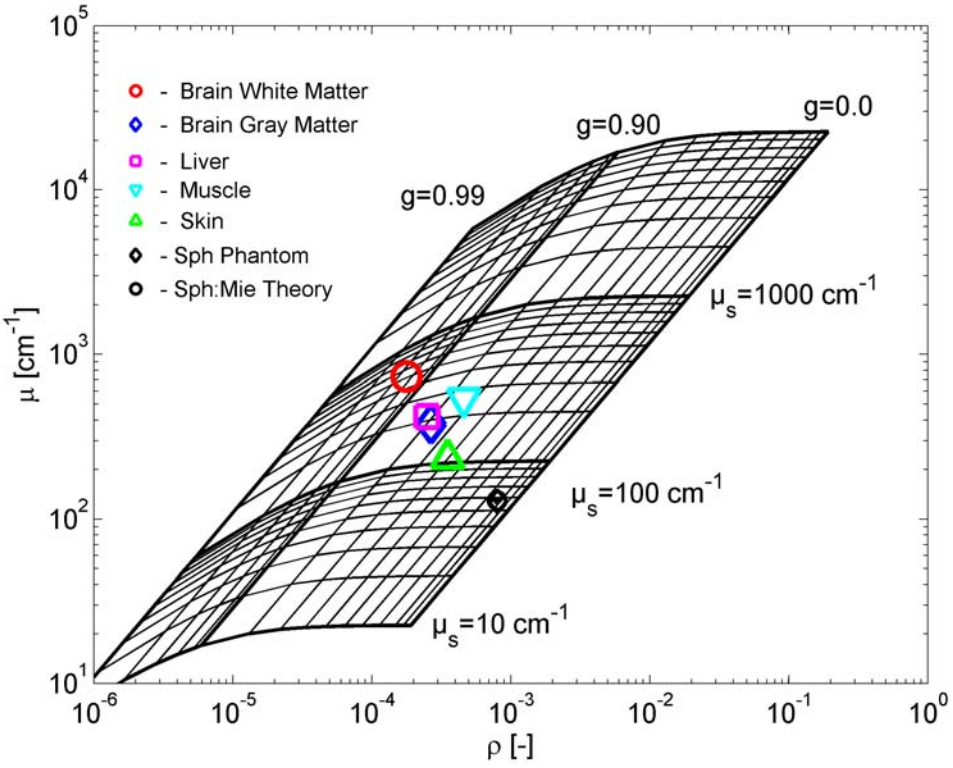

Figure 5.5: The median ρ and μ of the tissue data from set 2 where the tissue is not in contact with PBS, are superimposed on the analysis grid.)

tissue types like the liver and brain gray matter showed consistent results across all the mouse used in the study. Whereas fibrous (muscle) and layered tissue (skin) showed large variation. The theoretical model described in chapter 3 was validated using microsphere phantoms in chapter 4 and this chapter used the model to estimate optical properties of murine tissue. The following chapters apply the (μ, ρ) model to characterize, the mechanism of optical clearing of tissues (chapter 7) and the effect of a gene mutation on the collagen fiber organization in mouse dermis (chapter 8) through optical properties.

Chapter 6

Reflectance confocal microscopy of optical phantoms

This chapter was co-authored by: Bo Wang and Steven L. Jacques. This chapter was published in 'Biomedical Optics Express' [70],

6.1 Introduction

A variety of optical measurements can easily measure the absorption coefficient, μ_a, and the reduced scattering coefficient, $\mu_s' = \mu_s\,(1-g)$, of a tissue sample. However, separation of μ_s' into the two factors, the scattering coefficient, μ_s, and the anisotropy of scattering, g, usually involves bench-top experiments with thin tissue slices. This chapter describes a method that measures μ_s and g non-invasively on an intact tissue, which is therefore useful for in vivo measurements of tissue optical properties [1]. This chapter demonstrates the technique on some phantom tissues.

The method uses reflectance confocal scanning laser microscope (rCSLM), or alternatively optical coherence tomography (OCT), to scan into a sample material and observe the exponential decay of reflected signal as the focus is translated deeper into the sample. At deeper depths it is more difficult for photons to penetrate to the focus and scatter back out into the collection solid angle of the objective lens. Others have recognized that attenuation of an rCSLM or OCT

signal could characterize tissues (see [71] for review). The key improvement of this proposed method is to incorporate scattering anisotropy into the treatment so as to separately specify μ_s and g.

The method has been used to study the scattering consequences of a single gene mutation in mouse skin [5], the scattering changes as cells remodel a collagen gel [3, 23], and the scattering changes in mouse skin when soaked in glycerin to achieve optical clearing [72]. In all cases, the distinction between μ_s and g could be discerned. The g value is of particular interest since it relates to the size of scatterers [9]. The method has been used for enhanced image contrast in optical coherence tomography imaging of breast cancer lymph nodes [4, 73].

The three types of phantoms tested were (1) polystyrene microspheres in a gel, (2) solid polyurethane phantoms, and (3) a well-known commercial reflectance standard.

The goal of this report is to illustrate the use of the rCSLM technique as applied to solid phantoms and to offer an initial characterization of the μ_s and g of the phantoms.

6.2 Methods

6.2.1 Phantoms

A set of five phantom materials were tested:

1 Polystyrene microspheres in aqueous agarose gel.

The sphere diameter was 100-nm at a volume fraction of 2%. The refractive indices at 488 nm were $n_{spheres} = 1.599$ for spheres and $n_{water} = 1.336$ for the aqueous gel (98% water). The gel was held between a 1-mm-thick glass slide and a 120-μm-thick coverslip. One location on phantom was tested, since

such gels are routinely measured in our lab.

2 Hard polyurethane phantom

The phantom was obtained from INO, Inc., Canada, and is called Hard Biomimic^{TM} phantom [9]. See figure 6.1(A). Three locations of the phantom were tested, but the results were very consistent for each site.

3 Soft polyurethane phantom.

The phantom was obtained from INO, Inc., Canada, and is called Soft Biomimic^{TM} phantom. See figure 6.1(B). Again, three locations were tested.

4 Spectralon^{TM}, 99% reflectance standard.

The reflectance standard was obtained from LabSphere, Inc. (New Hampshire, USA), and is now available from Pro-Lite Technology, Inc. See figure 6.1(C). One location tested.

5 Spectralon^{TM}, 75% reflectance standard.

The reflectance standard was obtained from LabSphere, Inc. (New Hampshire, USA), and is now available from Pro-Lite Technology, Inc. figure 6.1(C). One location tested.

6.2.2 Confocal reflectance microscope

The reflectance-mode confocal scanning laser microscope (rCSLM), built in our laboratory (refer section 4.1 for a detailed description) has been used in previous studies [1, 3, 5, 71, 72]. An argon-ion laser channel was used in this study. The objective lens was water-coupled to the optical phantoms (Biomimic^{TM} and Spectralon^{TM} phantoms). For the microsphere gel, the microscope was water-coupled to the coverslip. Figure 2 shows the basic design. The pixel size was 0.312

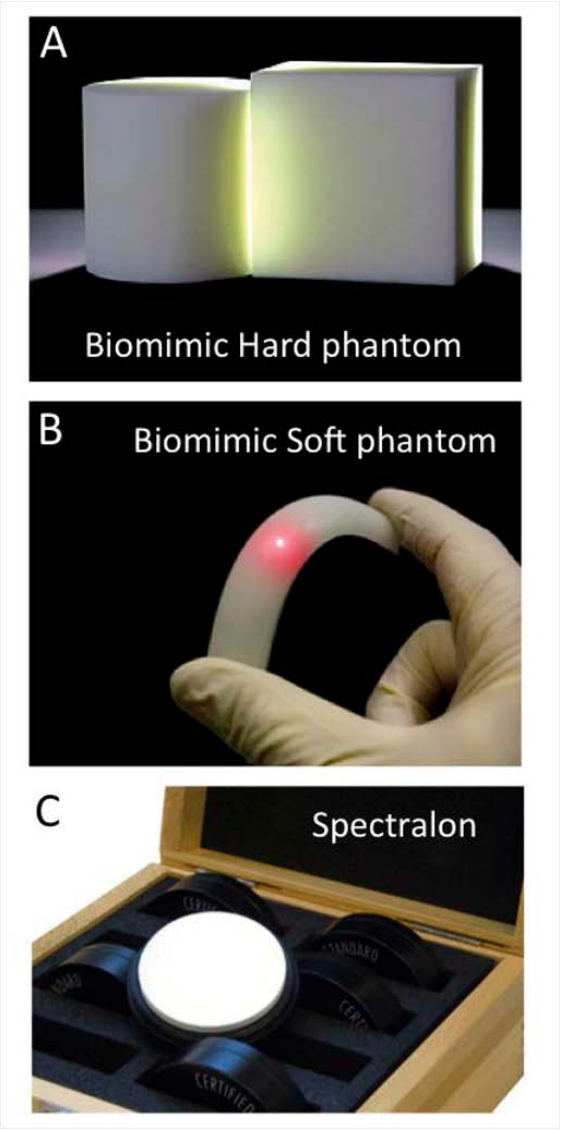

Figure 6.1: The phantoms. (A) Hard Biomimic^{TM} polyurethane phantom, INO, Inc., Canada. (B) Soft Biomimic^{TM} polyurethane phantom, INO. (C) Spectralon^{TM}, Pro-Lite Technology, Inc. Not shown is the gel phantom composed of 1% volume fraction 100-nm-dia. polystyrene microspheres in aqueous agarose gel. (Photos A,B from reference [2])

μm x 0.312 μm in lateral direction, while the axial step size of 1 μm at the water-phantom interface region (approximately 50 μm). However, to achieve a broader axial range of imaging, the axial stepsizes were increased to 5 or 10 μm at positions above and below this region were of 1-μm stepsizes was used.

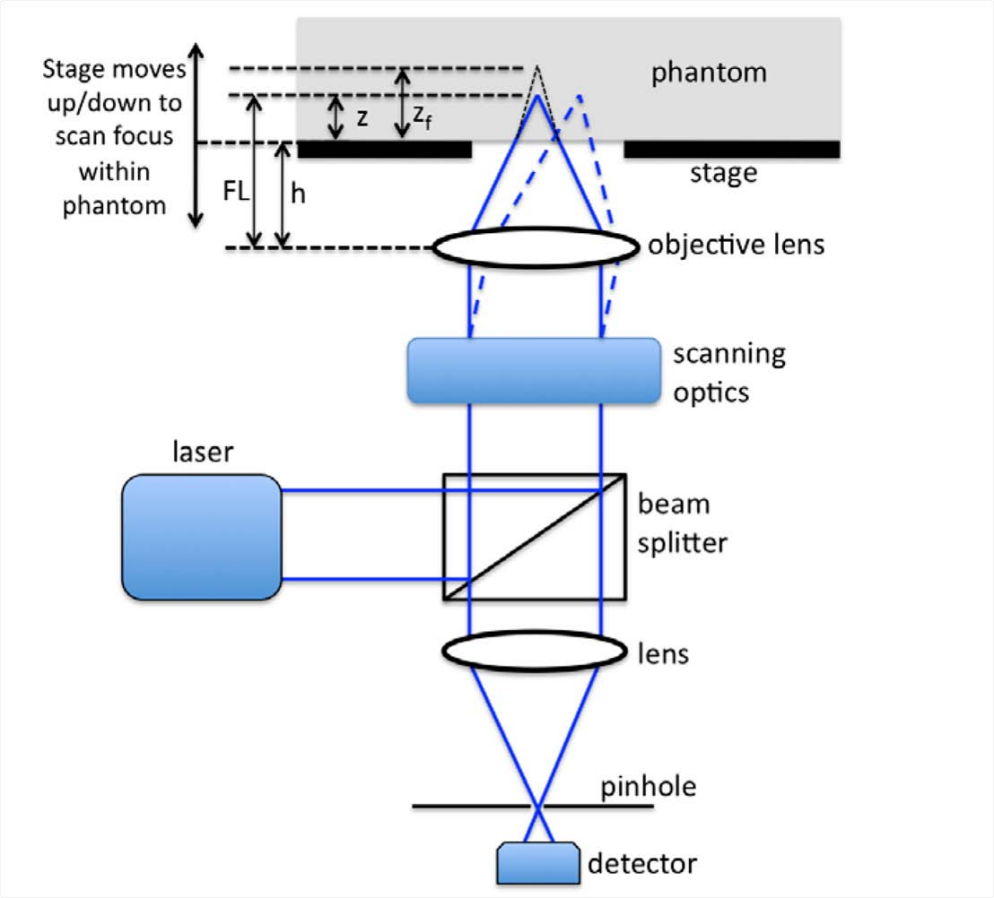

Figure 6.2: Schematic of the reflectance confocal scanning laser microscope (rC-SLM). Laser light is delivered to a focal volume within the phantom, and reflectance from this focus is returned through a pinhole to a detector. The sample stage moves the phantom up and down in order to scan the focus within the phantom.

6.2.3 Data acquisition

Figure 6.3 shows examples of the raw images of reflectance for the phantoms, shown as $\log_{10}(V(z,x))$ where V is the detector voltage. The abcissa, x, is the lateral position of the phantom. The ordinate, z, is the apparent depth of the focal volume equal to the difference between the focal length (FL) and the distance (h) between the objective lens and the phantom surface.

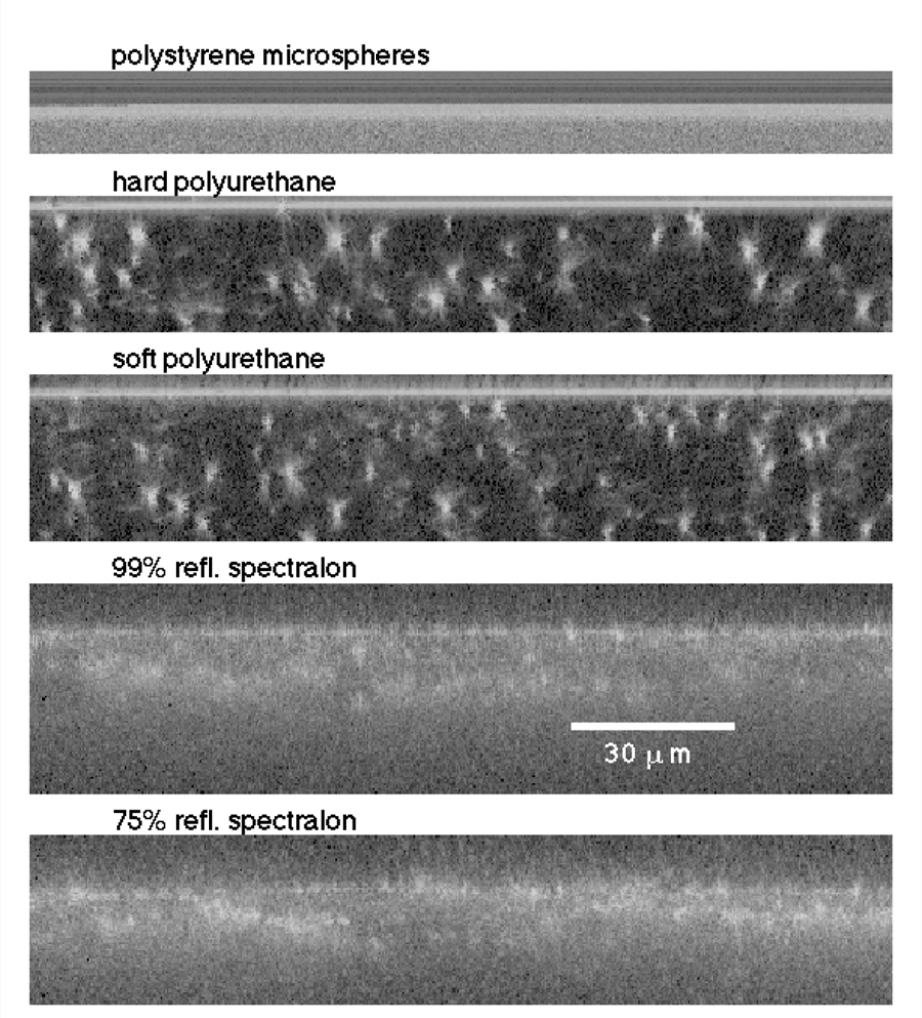

Figure 6.3: Side-view confocal reflectance image in volts, image(z,x) at y = middle of 3D image. The images show $\log_{10}$(voltage), where voltage encodes the reflectance. The color code is black = 0.01V and white = 10V. The axial stepsize, Δz, was 1 μm. The microspheres have a glass/gel interface, while others have a water/phantom interface.

6.2.4 Calibration

Figure 6.4 shows the calibration of the system. The glass-water(gel) interface of the microsphere-water(gel) phantom was imaged to yield a peak voltage $V_{gw} = 5.14$ V. The expected reflectance from this interface was $R_{gw} = ((n_{water} - n_{glass})/(n_{water} + n_{glass}))^2 = 0.00427$, where $n_{glass} = 1.522$. Then a calibration factor was calculated: $calib = \frac{R_{gw}}{V_{gw}} = 1.204\ x\ 10^{-4}$[1/V]. Thereafter, any measurement V was multiplied

by *calib* to yield the reflectance R, which is the fraction of light delivered by the microscope that is returned into the microscope for detection.

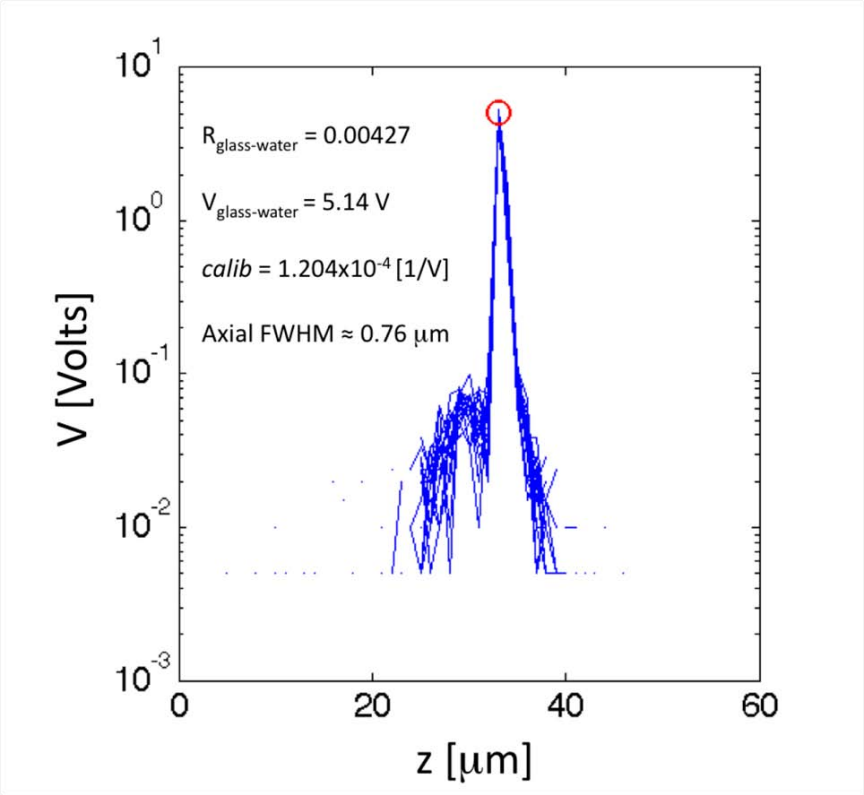

Figure 6.4: Calibration of confocal reflectance measurement at 488 nm wavelength, using glass-water(gel) interface. Subsequent measurements of phantom are multiplied by the factor *calib* ($1.204 \text{ x } 10^{-4} V^{-1}$) such that a measurement of a glass-water interface will yield $R_{glass-water} = 0.00427$ and measurement of a mirror will yield $R_{glass-water} = 1$.

To check the calibration, the axial profile, $R(z_f)$, for the polystyrene microsphere gel phantom was analyzed to fit the expression:

$$R(z_f) = \rho \, e^{-\mu \, z_f} \tag{6.1}$$

As the distance height (h) of the lens above the surface of the phantom was changed, the apparent depth position of the focus varied as $z = FL - h$, where FL is the focal length of the lens. When $h = FL$, the focus is at the phantom

surface. As h was decreased, z moved into the tissue. However the true position of the focus, z_f, increased as:

$$z_f = \frac{\partial z_f}{\partial z}(z - D_{glass}) \tag{6.2}$$

where D_{glass} is the thickness of the glass coverslip if in place (if no glass, D_{glass}= 0). The parameter $\frac{\partial z_f}{\partial z} = \frac{tan(\theta_1)}{tan(\theta_2)}$, where $\theta_1 = sin^{-1}(\frac{NA}{n_{water}})$ and $\theta_2 = sin^{-1}(\frac{NA}{n_{phantom}})$. The factor $\frac{NA}{n\_phantom}$ is referred to here as the *effective numerical aperture*. For the aqueous gel, the value of $\frac{\partial z_f}{\partial z}$ is 1.00. For the polyurethane and Spectralon^{TM} phantoms, the value of $\frac{\partial z_f}{\partial z}$ was 1.20, based on an assumed value of 1.49 for $n_{phantom}$. Hence, the original data versus z was converted to data versus z_f before subsequent analysis.

6.2.5 Analysis

The behavior of $R(z_f)$ depends on the parameters ρ and μ, which are described as

$$\mu = (\mu_s a(g) + \mu_a) 2G(g, NA) \tag{6.3}$$

$$\rho = \mu_s \Delta z b(g, NA) \tag{6.4}$$

where Δz is the standard axial resolution, $\Delta z = \frac{1.4\lambda}{NA^2}$, where $NA = sin(\theta/2)n_{phantom}$ with $\theta/2$ equal to the half angle of light delivery within the phantom and $n_{phantom}$ is the refractive index of the phantom [71, 74]. The value of $n_{phantom}$ for the polyurethane and Spectralon^{TM} phantoms was assumed to be 1.49.

The parameters $a(g)$, $b(g, NA)$ and $G(g, NA)$ in equations 6.3 and 6.4 are described in chapter 3. Figure 6.5 shows an example analysis. A superficial region (5-50 μm below the surface) was used for fitting, beyond the effects of the front

surface reflectance and before diffuse light begins to contaminate the signal. The noise floor due to diffuse light reflectance escaping within the solid angle eventually collected by the detector pinhole becomes important when the focus is located at depths beyond the transport mean free path, $1/(\mu_s(1-g))$. Hence, useful measurements are restricted to the superficial layer.

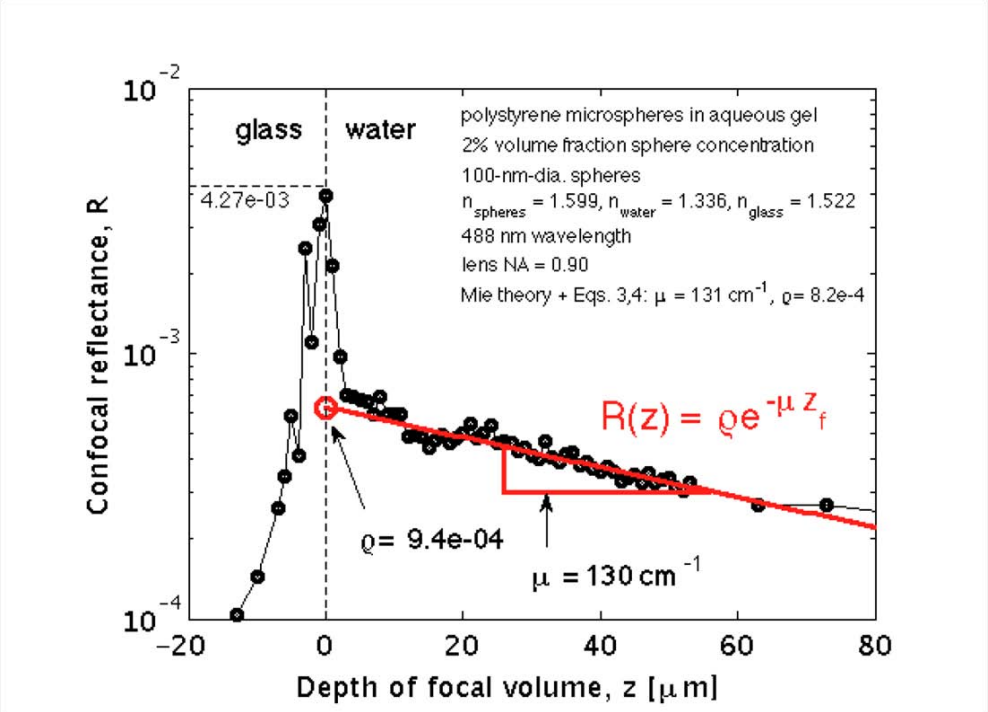

Figure 6.5: Axial profile of confocal reflectance versus depth of focus, $R(z_f)$. The reflectance from the glass-gel interface was assumed to match the specular reflectance of a glass-water interface, $R_{glass-water} = 0.00427$, and was used to scale the laboratory counts. Hence, $R(z_f)$ is calibrated such that reflectance from a mirror in the focus yields R = 1. The exponential red line is $R(z_f) = \rho e^{(-\mu z_f)}$. The value ρ is the extrapolated red line value at $z_f = 0$. The value of μ is specified by the slope.

Figure 6.6 plots the mean μ versus mean ρ from figure 6.5 on a grid of $iso-g$ lines and $iso-\mu_s$ lines, based on equations 6.3 and 6.4. This grid allows interpretation of the μ and ρ data in terms of the optical properties μ_s and g. The experimental data point (red circle) indicates $\mu_s = 57.7\ cm^{-1}$, $g = 0.072$, $\mu = 130\ cm^{-1}$, $\rho = 9.2$ x 10^{-4}. Also shown is the predicted data point using Mie theory

(black diamond), which has values of $\mu_{s.MIE} = 58.2\ cm^{-1}$, $g_{MIE} = 0.129$, $\mu_{MIE} = 131\ cm^{-1}$, $\rho_{MIE} = 8.2$ x 10^{-4}. Work continues on testing the accuracy of the first-order theory (equations 6.3, 6.4) and on experimental methods for preparing microsphere gels for calibration.

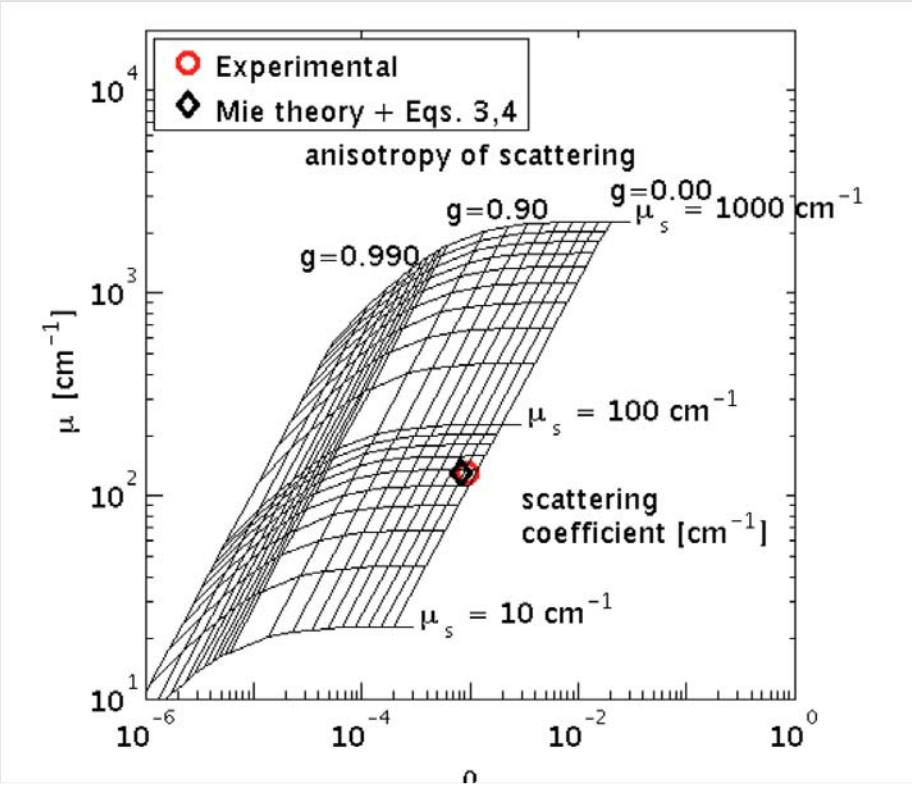

Figure 6.6: Calibration grid with experimental data (red circle) and the Mie theory prediction (black diamond) using Equation 6.3 and 6.4 for the polystyrene microsphere gel of figure 6.5. Mie theory predicts $\mu_s = 58.2\ cm^{-1}$, $g = 0.129$, and equations 6.3 and 6.4 predict μ_{MIE}, $= 131\ cm^{-1}$, $\rho_{MIE} = 8.2$ x 10^{-4}. The experiment presents $\mu = 130 cm^{-1}$, $\rho = 9.2$ x 10^{-4}, and $\mu_s = 57.7\ cm^{-1}$, $g = 0.072$.

6.3 Results

The images of figure 6.3 show that the polyurethane (hard and soft polyurethane phantom) presented a low density of TiO_2 particles that strongly scattered light. These phantoms did not present a uniform attenuation $R(z_f)$ within the range of

imaging that could be reliably analyzed using equations 6.1- 6.3. Nevertheless, the data was fit by equation 6.1 to yield μ and ρ experimental values.

Figure 6.7 shows axial profiles of 15 random x,y positions in the phantoms. The curves indicate a slow attenuation of signal as the focus is moved deeper into the tissue. Red lines indicate exponential fits to the attenuation of the $R(z_f)$ signal (bold lines indicate region of data fitted), and the slopes specify the values of μ. The fit is extrapolated (dashed lines) to the front surface of the phantom to specify the value of ρ (indicated by red symbol).

Figure 6.8 displays a plot of the μ and ρ values specified by the fits shown as red lines in figure 6.7, and superimposes a grid of $iso-\mu_s$ and $iso-g$ lines to aid interpretation. The grid is drawn assuming the lens is water coupled to an aqueous gel (n = 1.336). There is agreement between the experimental measurement and Mie theory for the microsphere gel. The grid shifts downward slightly when the lens is water coupled to the phantom polymer materials (n assumed to be $\approx$ 1.49) (grid not shown since shift is very small; the grid's μ and ρ drop $\approx$ 3%, so data are properly deduced to be $\approx$3% higher than values calculated with the water-coupled grid). The analysis considered this effect when computing the values summarized in Table 6.1.

Table 6.1: Summary of phantom measurements and properties

Phantom	μ $[cm^{-1}]$	ρ	μ_s $[cm^{-1}]$	g
Mie theory for microspheres	131.2	8.1x10^{-4}	58.2	0.112
polystyrene microsphere gel	135.5	8.6x10^{-4}	60.1	0.122
hard polyurethane (Biomimic^{TM})	6.4	3.1x10^{-5}	7.6	0.531
soft polyurethane (Biomimic^{TM})	50.9	5.8x10^{-5}	24.4	0.674
99% refl. Spectralon^{TM}	289	1.2x10^{-3}	132	0.262
75% refl. Spectralon^{TM}	439	3.8x10^{-3}	200	0.003

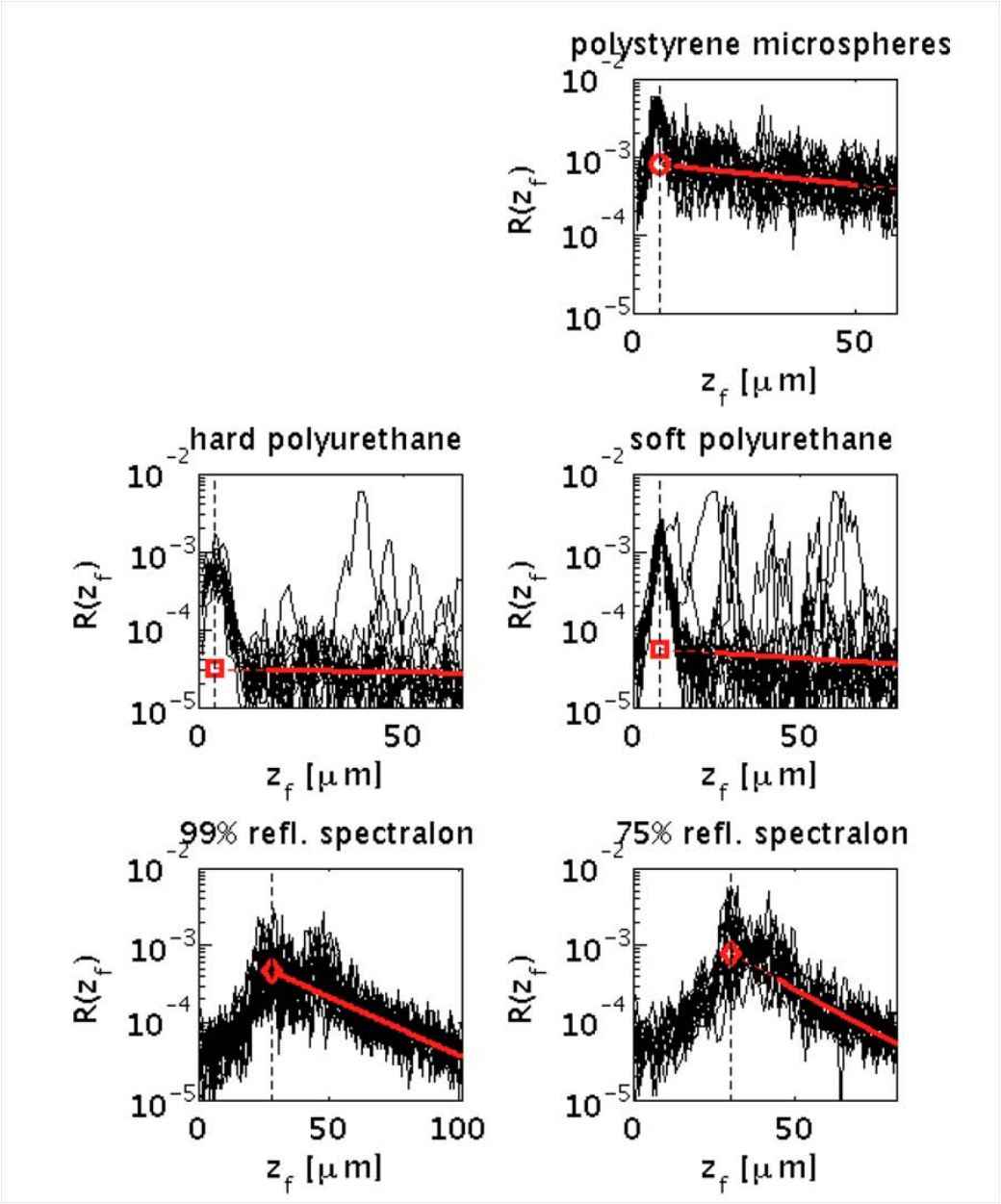

Figure 6.7: Sampling of 15 axial profiles for the phantoms. The polyurethane phantoms have a baseline of low reflectance at the noise level of the measurement, but there are occasional spikes of reflectance from local strong reflectors. Bold red lines are exponential fits to the data, which is extrapolated to the front surface, indicated by red symbol.

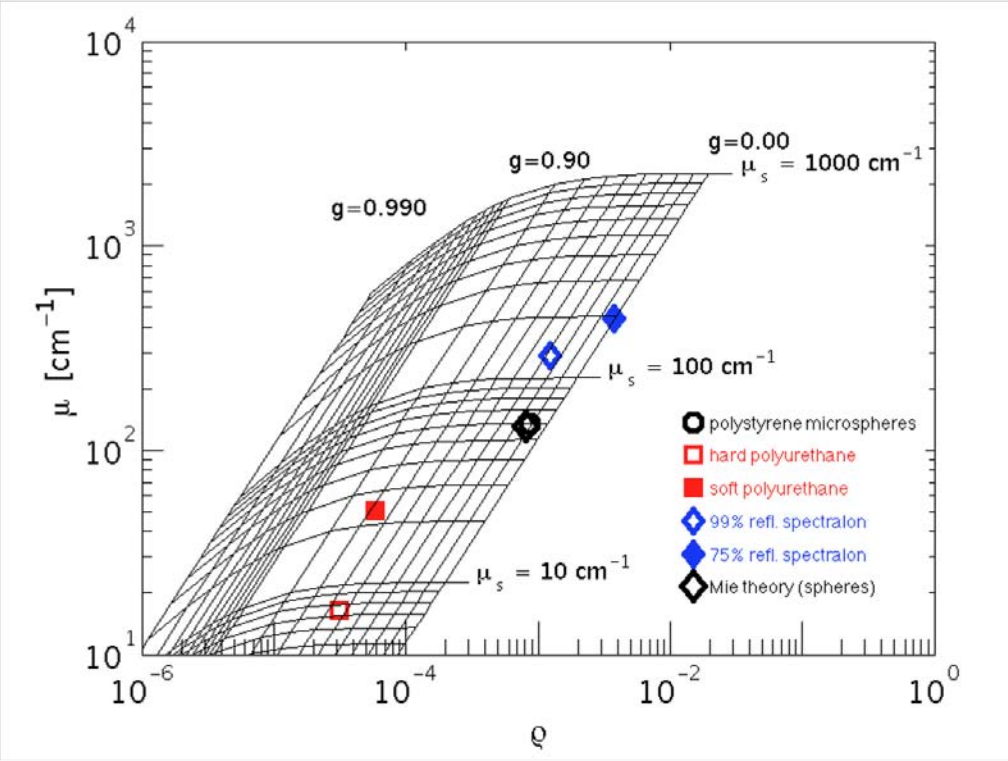

Figure 6.8: Experimental attenuation vs reflectivity for phantoms at 488 nm wavelength, based on exponential fits of axial profiles (red lines in figure 6.7). The experimental measurement on polystyrene microspheres and the prediction of Mie theory are closely aligned.

6.4 Discussion

This pilot study of the optical properties of phantoms is intended to illustrate a noninvasive experimental approach toward specifying the optical scattering properties of a phantom, specifically the scattering coefficient (μ_s) and the anisotropy of scattering (g). The polyurethane phantoms (INO Biomimic^{TM}) were shown to have a background optical properties along with a low density of dispersed strongly scattering TiO_2 particles. The soft polyurethane phantom had higher μ_s than the hard polyurethane phantom probably due to the difference in the composition of the background material that gives different physical characteristics. However, the results (figure 6.8) show that the g values are similar for the both polyurethane

phantoms. The characteristics of TiO_2 particles used in the polyurethane phantoms are proprietary and not known. Moffitt *et al.* [75] employed scanning electron microscope to determine the size of the TiO_2 used to make phantoms similar to hard Biomimic^{TM} phantoms. The size of the TiO_2 was determined to be 340±90 nm. The g values were calculated for TiO_2 particles embedded in polyurethane background material using Mie theory by assuming TiO_2 particles to be spheres. The g of the TiO_2 particles is between 0.48 and 0.62 at 488nm, similar to the values determined by rCSLM measurement. It is not known if the Biomimic^{TM} phantoms use the similar TiO_2 particles used by Moffitt *et al.* [75].

Spectralon^{TM} phantoms were more dense in scattering, hence a higher μ_s than the polyurethane phantoms, and individual strongly scattering particles were present but less evident. The polystyrene microsphere gel phantom was the most uniform phantom, composed of a high concentration (2% volume fraction) of 100 nm-dia. spheres. Our experience with microsphere phantoms using larger spheres is that they present as discrete strong scatterers, similar to TiO_2 particles in Biomimic^{TM} phantoms. Therefore, we routinely use small 100 nm-dia. spheres when calibrating experiments.

Future work should explore the wavelength dependence of the μ_s and g values derived from axially scanned rCSLM signals. Comparison of the values against macroscopic measurements of the diffusion property $\mu_s' = \mu_s(1-g)$ should be made.

The method outlined in this paper can be used with any confocal microscope or OCT system operating in reflectance mode. The method has been used with a variety of systems, both custom built and commercial. The μ measurement is easily accomplished if the axial stepsize between successive x,y images is known. The ρ measurement requires calibration, however, such as the measurement of a glass/water interface, as in this paper. Alternatively, the measurement of a

microsphere gel can be used to calibrate ρ. Since the anisotropy g is sensitive to ρ, the calibration is worthwhile if rCSLM or OCT is used to characterize the nanoarchitecture of a tissue.

Chapter 7

Assessment of optical clearing agents using reflectance-mode confocal scanning laser microscopy

This chapter was co-authored by: Kevin G. Phillips and Steven L. Jacques. This chapter was published in 'Journal of Innovative Optical Health Sciences' [72],

7.1 Introduction

Optical clearing agent (OCA) is a chemical substance that alters the scattering properties of tissue, to allow better light penetration. This is achieved by applying a clearing agent like glycerin to the skin, which penetrates into the skin. The glycerin entering the dermis is expected to increase the refractive index of the tissue as well as to osmotically withdraw water from the dermal collagen fibers, thereby yielding a lower scattering. In previous work, we have used reflectance mode confocal microscopy to image the superficial layers of mouse skin to investigate onset of melanoma in murine cancer models [16], genetic changes in skin [5] and epidermal thickening due to keratinocyte proliferation [76]. In this chapter, confocal reflectance imaging is used to specify tissue optical scattering properties

of skin dermis exposed to clearing agents. In such imaging, the initial magnitude and attenuation of reflectance as the focus is scanned into the tissue provides information about the optical properties of scattering coefficient (μ_s) and anisotropy of scattering (g). In this chapter, we report on the effect of clearing agents (saline, 80% Dimethyl Sulphoxide (DMSO), pure glycerin) on the μ_s and g of scattering at 488 nm wavelength of mouse dermis.

7.2 Materials and Methods

Three 14-week-old mice on a C57/Black genetic background were euthanized and from each mouse four skin samples from depilated regions of the back were freshly excised and the dermal side of each specimen was scraped clean of any muscle and subcutaneous fat. This dermal surface was immediately placed in a shallow pool of either saline, glycerin (Fischer Scientific, 99.9% pure), or Dimethyl Sulphoxide (DMSO) (Fischer Scientific) diluted by water to an 80% solution [77], held within a small petri-dish. The clearing agents were allowed to permeate the skin tissues for 1 hr [78], then blotted dry with a cotton swab. Samples were then placed against a glass coverslip that was positioned on the optical stage of an inverted reflectance-mode confocal scanning laser microscope (rCSLM), using water to couple the lens to the glass coverslip. One sample was kept moist but not immersed in any fluid, then measured, which served as a control. A total of 12 samples (3 mice x 4 samples) were imaged before and after treatment. All animal studies were approved by the Oregon Health and Science University Institutional Animal Care and Use Committee.

7.2.1 Imaging System

The rCSLM microscope used in this study is described in section 4.1. A water-coupled objective lens was used in the rCSLM system. As the sample stage is moved to translate the focus into the tissue, the higher refractive index of OCA introduced an error in the location of the focal point within the tissue. Figure 7.1 illustrates the penetration of light into a sample from below in the inverted microscope. Controlling the height of the sample stage controlled the lens/glass-coverslip distance (h), which in turn controlled the apparent depth of the focus, z'_f. As light moved through the lens/water/glass-slide/tissue interfaces, refraction occurred that affected the true depth of the focus within the tissue. In figure 7.1, the apparent depth z'_f is show by the dashed lines, while the true focus z_f is shown by the solid lines. The change in z_f relative to a change in z'_f was determined by ray tracing. The refractive index values of saline, skin (dermis), 80% DMSO, [79] and glycerol [80] were 1.33, 1.38, 1.45 and 1.47, respectively, which resulted in $\frac{\partial z_f}{\partial z'_f}$ to equal 1.00, 1.055, 1.161 and 1.187, respectively. The true value of the focus was calculated:

$$z_f = \frac{\partial z_f}{\partial z'_f}(FL - (h + D_g)) \tag{7.1}$$

where h was the lens-glass distance, D_g was the thickness of the glass, and FL was the focal length of the lens. The refraction also influenced the apparent numerical aperture of the objective lens, in other words, changed the solid angle of collection of backscattered light. This small correction was also included in the calculation of G (equation 7.5 below). In summary, the refractive index of the sample was considered in the calculations.

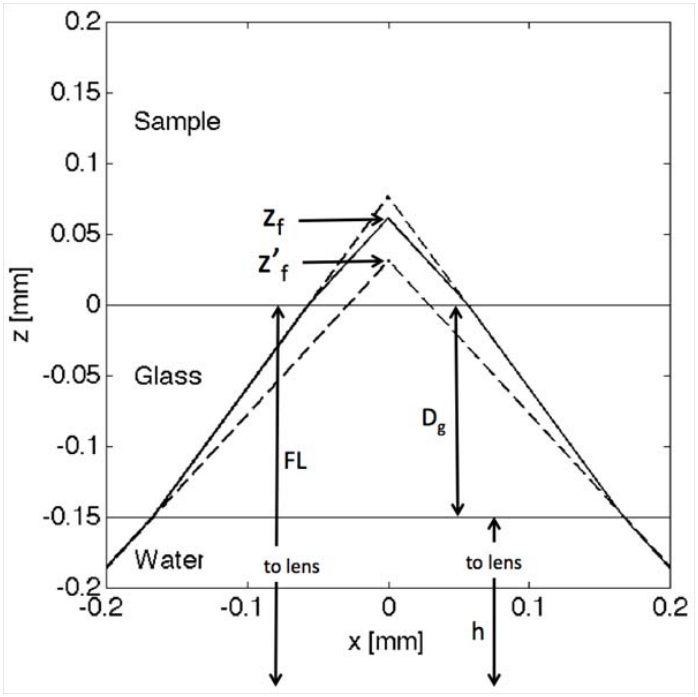

Figure 7.1: The confocal microscope operates in inverted mode, delivering light from below from the lens through water and a glass coverslip into the sample. The relationship between the true position of the focus (z_f) (solid line) and the apparent position of the focus, $z'_f = FL - (h + D_g)$ (dashed line), where h is the distance between the lens and the glass/sample interface and D_g is the thickness of the glass coverslip, is described as $z_f = z'_f = \frac{\partial z_f}{\partial z'_f}$, where $\frac{\partial z_f}{\partial z'_f}$ equals 1.000, 1.055, 1.161 and 1.187 for water (saline), skin (dermis), 80% DMSO, and glycerin, respectively, at 488 nm wavelength.(Refractive indices are $n_{water} \approx 1.33$, $n_{dermis} \approx 1.38$, $n_{80\%DMSO} \approx 1.45$, $n_{glycerin} \approx 1.47$).

7.2.2 Image Processing

The rCSLM system stored a reflectance signal from the PMT, $V[Volts]$, from the different tissue samples in a three dimensional array, $V(x, y, z'_f)$. Here x and y corresponded to transverse directions, while z'_f corresponded to the apparent axial distance of the focus within the tissue prior to correction for the refractive index of the sample. The average axial reflectance profile for a region of interest on the

skin was calculated:

$$R(z_f') = \frac{1}{CALIB}\frac{1}{N}\sum_{i=1}^{10}\sum_{j=1}^{10} V(x_i, y_j, z_f') \tag{7.2}$$

averaging $N = 100$ voxels within 10x10 x,y voxels for each of 100 z-axis depths. This region of interest corresponded to a $4\mu m$ x $4\mu m$ x $100\mu m$ volume. After correcting for refraction, the $R(z_f)$ signal decayed exponentially versus the true depth of focus z_f, characterized by a local reflectivity ρ and an attenuation coefficient $\mu[cm^{-1}]$.

$$R(z_f) = \rho\, e^{-\mu z_f} \tag{7.3}$$

The optical properties were extracted from $R(z_f)$ by mapping the ρ and μ into the scattering coefficient (μ_s), and anisotropy of scattering (g), using the analysis described in chapter 3. Briefly the

$$\mu = a(g)\mu_s 2G(g, NA) \tag{7.4}$$

$$\rho = \mu_s \Delta z b(g, NA) \tag{7.5}$$

where scattering efficiency factor, $a(g)$, mitigates the effect of scattering to prevent transmission of photons to/from the focus; $a(g)$ depends on g and decreases to 0 as g approaches 1. The factor $2G(g, NA)$ multiplies the depth of focus, z_f [cm], to yield the round-trip photon pathlength in the tissue, in which G depends on the effective numerical aperture (NA_{eff}) of the objective lens as light enters the sample. The calculation of pathlength augmentation factor, $G(g, NA)$, considered the refractive index of each type of clearing agent at the glass/sample interface. The axial extent of the focus is $\Delta z \approx 1.4\lambda/(NA_{eff})^2$, and the product $\mu_s \Delta z$ is the fraction of light reaching the focus that is scattered within the focus. A fraction $b(g, NA)$ of this scattered light is backscattered within the solid angle of collection

of the objective lens, where scatter collection efficiency, $b(g, NA)$, depends on g and the NA of the lens.The calculation of $b(g, NA)$ used the NA_{eff} appropriate for each type of clearing agent. Table 7.1 summarizes the values of parameters used in equation 7.5 as a function of the clearing agent.

Table 7.1: The refractive index of the clearing agent on the glass/sample interface affects the relationship ($\frac{\partial z_f}{\partial z'_f}$) between the true focus (z_f) and apparent focus (z'_f)

Sample	n	$\frac{\partial z_f}{\partial z'_f}$	NA	Δz	G	$b(g)$	$a(g)$
Water	1.33	1.000	0.9	8.43e-05	1.107	0.015	0.944
Skin(dermis)	1.38	1.055	0.867	9.08e-05	1.096	0.014	0.944
80% DMSO	1.45	1.161	0.826	1.00e-04	1.085	0.012	0.944
Glycerin	1.47	1.187	0.814	1.03e-04	1.082	0.012	0.944

A calibration constant ($CALIB$ $[Volts^{-1}]$) adjusted the magnitude of the raw data such that the resulting mean value of g for the control and saline-soaked samples matched the g of previous experiments, $g \approx 0.7$ for skin at 488 nm. In previous experiments, 100 nm-dia. polystyrene microspheres in soft agar gel at a 2% volume fraction were used to calibrate the system. The value of $CALIB$ was determined by measurements of a phantom consisting of polystyrene microspheres in water (yields $\mu_s = 57cm^{-1}$, $g = 0.112$ at 488 nm wavelength). The μ value did not need adjustment since it is a relative measurement; μ was in agreement with previous experiments.

7.3 Results

The skin samples were placed on a white surface with a black line and photograph were taken with a standard camera. The effect of the clearing agent was visualized by the visibility of the line beneath the samples. Figure 7.2 shows representative samples for the four tested conditions (control, and 1-hr exposure to saline, DMSO,

glycerin) before and after the exposure to clearing agent. The glycerin-exposed sample significantly clarified. The other samples showed little change.

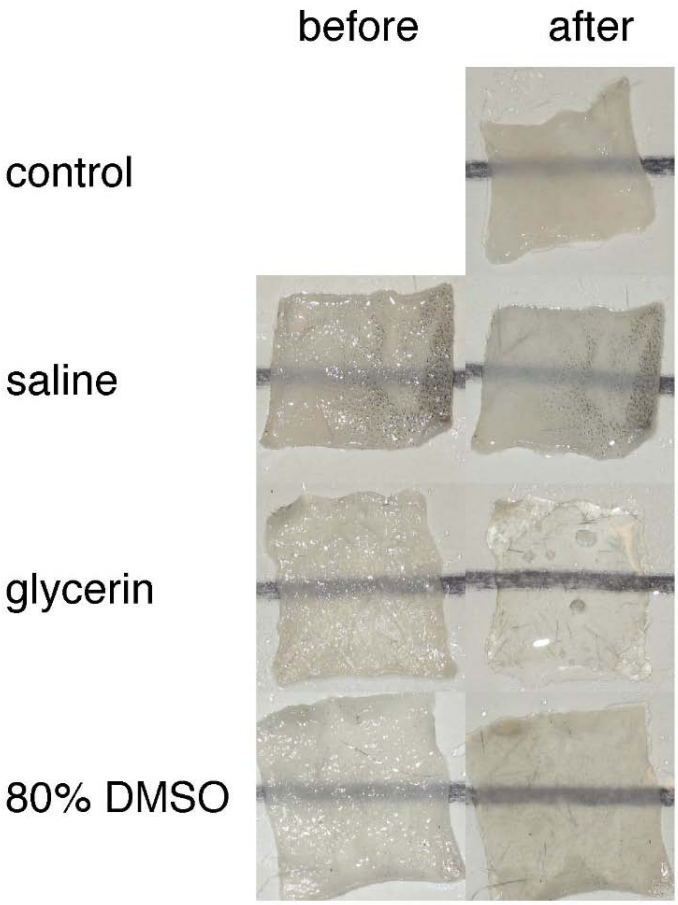

Figure 7.2: Images of skin tissue showing control sample, and before and after 1-hr treatment with saline, glycerin or 80% DMSO. The glycerin sample is strongly cleared. The 80% DMSO sample is partially cleared.

Figure 7.3 shows sagittal views of the skin samples, $R(z'_f, x)$ at y, expressed as the raw data log_{10}(Detector voltage). The control, saline- and DMSO-exposed samples presented stronger reflectivity than the glycerin-exposed samples that presented very low reflectivity.

Figure 7.4A shows the axial profiles of the detected reflectance, $R(z_f)$ at x,y, along with the exponential fits using equation 7.3, which are shown as dashed lines where the black dot indicates the value of ρ and the slope indicates the value of

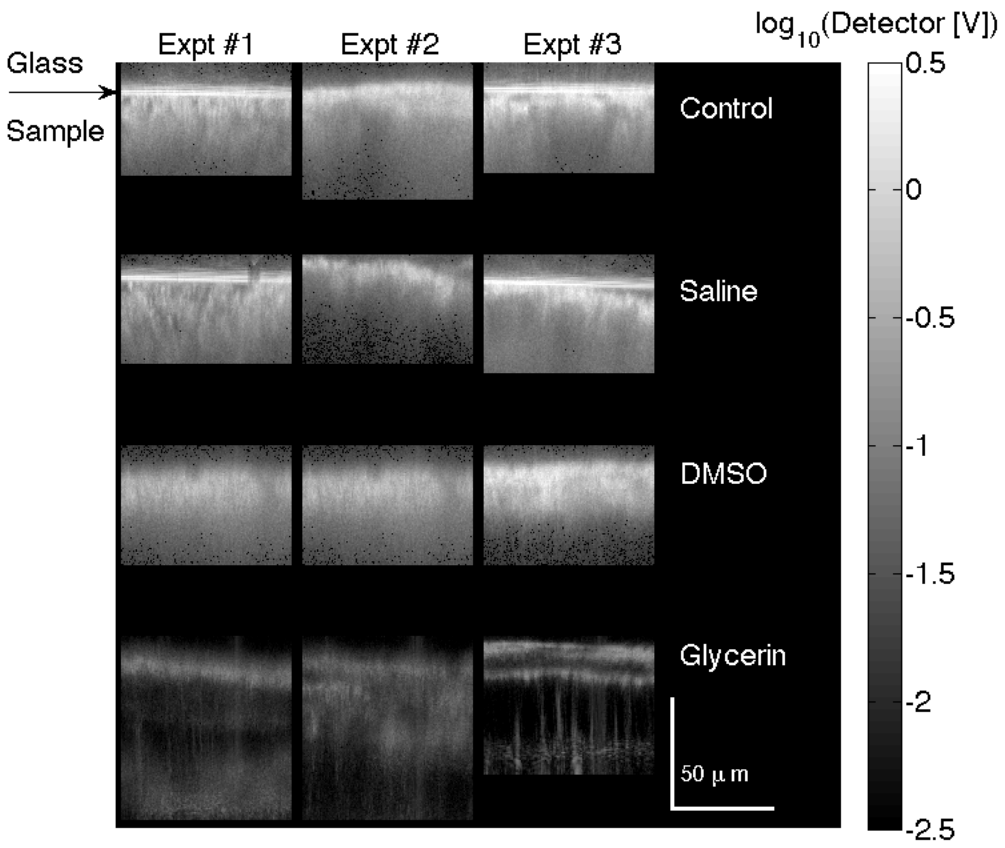

Figure 7.3: Sagittal views of the skin samples from three mice, showing the reflected signal, $R(z'_f, x)$, in volts [V] acquired by the microscope as a function of the apparent depth of focus (z'_f) and lateral position (x). The colorbar indicates the $\log_{10}$(Detector [V]). The top bright surface is the glass/sample interface (arrow). The signal decays as the microscope scans deeper into the tissue. The glycerin image is darker, indicating less reflectance from the glass/glycerin interface and from within the skin sample.

μ. The glycerin shows a much lower reflectivity ρ while the attenuation μ for all samples is similar. Figure 7.4B plots the μ vs ρ on a log-log scale, and superimposes the analysis grid of μ_s vs g based on equation 7.5. The plot suggests that glycerin has a greatly increase anisotropy of scattering (g) while its scattering coefficient (μ_s) is only slightly affected. The DMSO and saline may have had some slight effects of dermal properties, but the effects were not reliably reproducible in these experiments.

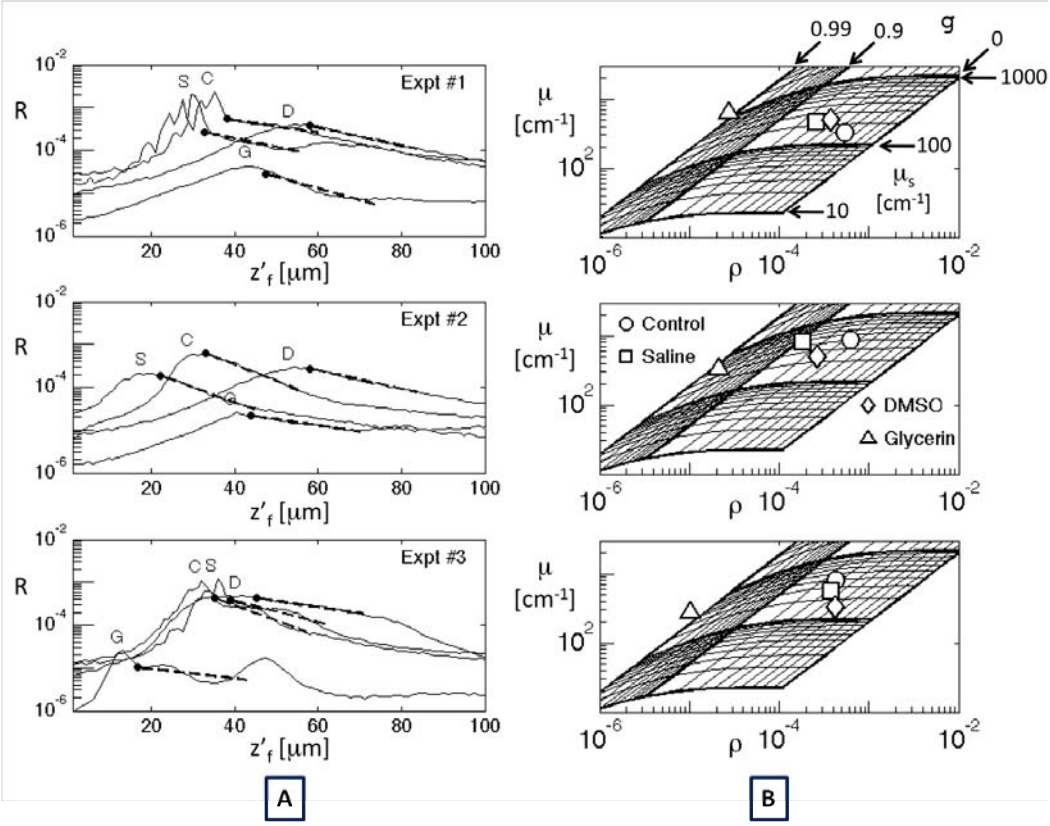

Figure 7.4: The experimental data, attenuation (μ) versus reflectivity (ρ), for three mice (labeled #1, #2 and #3) for the four conditions of control, and after 1-hr exposure to saline, glycerin or 80% DMSO. (A) Axial profiles. Dashed lines show region of fitting to specify μ, ρ. The black dot indicates ρ and the slope indicates μ. (B) Plots of μ vs ρ, with analysis grid μ_s,g superimposed. The glycerin caused a significant increase in g but little obvious change in μ_s. DMSO and saline may have had some slight effects, which were not reliably reproducible in these experiments.

7.4 Discussion

In these preliminary experiments, there was significant variability in the data. Nevertheless, there was a clear indication that glycerin increased the anisotropy (g) of scattering, while having little effect on the scattering coefficient itself (μ_s). To explain the optical clearing effect of glycerin on dermal scattering, the matching of refractive index between collagen fibers and surrounding medium seems the obvious explanation. A test of this hypothesis is presented in the following paragraphs.

The hypothesis is tested considering using Mie theory. Consider a solution of microspheres (diameter $D_o = 0.250\ \mu m$, volume fraction $v_f = 0.12$, $n_{med} = 1.33$, $n_{par} = 1.50$) that mimics the observed optical properties of skin ($\mu_s \approx 300 cm^{-1}, g \approx 0.70$, at 488 - nm wavelength) when using Mie theory. Now increase the refractive index of the medium, n_{med} from 1.33 to 1.47 in steps of 0.02. Also increase the size of the particle from D_o to $2D_o$, $4D_o$ and $8D_o$. For each case, use Mie theory to calculate μ_s and g, then equation 7.5 to calculate μ and ρ. Figure 7.5 shows the result. A bold-line grid is shown that indicates how the parameters μ, ρ and μ_s, g would vary as n_{med} and diameter are increased. The grid indicates that increasing n_{med} will cause μ_s to drop, but not strongly affect g. In contrast, increasing the particle diameter will cause g to increase but cause only a slight drop in μ_s.

The details of this latter effect on μ_s as n_{med} increases depends on the degree to which the particle refractive index, n_{par}, changes as it swells due to exposure to a clearing agent. In figure 7.5, the n_{par} was allowed to approach the refractive index of the surrounding n_{med} proportionately as its volume increased, as if the particle were becoming swollen by the clearing agent. But even if the n_{par} were kept constant during the change in particle diameter, a similar bold-line grid still occurs. The basic conclusion from the Mie theory simulation and the results is that a change in particle size can explain the significant drop in ρ and with little change in μ, corresponding to an increase in anisotropy g while μ_s is relatively stable. Glycerol was shown to decrease the collagen fiber diameter, with closely packed fibers [81]. Probably, closely packed collagen fibers were observed as increased particle size by rCSLM measurement.

In conclusion, this chapter describes the reflected light collected by a confocal microscope as the focus is scanned into freshly excised mouse dermis, for dermal samples that were exposed for 1 hr to saline, DMSO and glycerin, or not exposed as a control. The axial profiles of reflectance, $R(z_f)$, were analyzed by equation 7.3 to

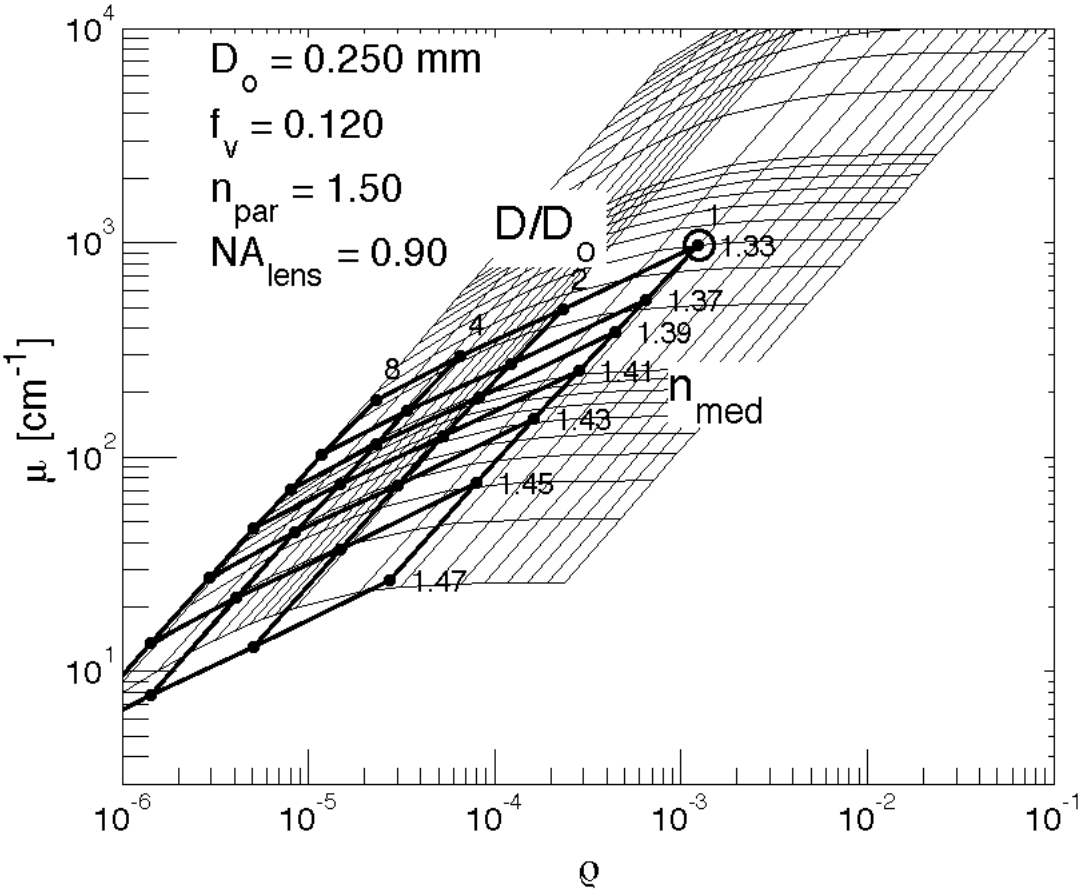

Figure 7.5: Mie theory approximation of expected changes in μ, ρ and μ_s, g for a solution of scattering particles, when the refractive index of the medium is changed and the size of the particles is changed. The starting point is an aqueous solution ($n_{med} = 1.33$) of spherical particles of diameter $D_o = 0.250\ \mu m$, refractive index $n_{par} = 1.50$, at a concentration of volume fraction $v_f = 0.12$. The wavelength is $0.488\ \mu m$. The numerical aperture of the lens is $NA = 0.90$. The bold lines show a grid where the n_{med} is varied as 1.33, 1.37, 1.39, 1.41, 1.43, 1.45 and 1.47, and the size of the particles is varied as $D_o, 2D_o, 4D_o and 8D_o$. This grid illustrates that changing only n_{med} will cause a drop in μ_s but not a change in g. The observed change in the anisotropy of skin scattering caused by glycerin is likely due to an increase in the size of collagen fibers.

yield the attenuation μ and reflectivity ρ, and by equation 7.5 to yield the scattering coefficient μ_s and anisotropy of scattering g. The glycerin sample showed a strong drop in ρ, corresponding to a significant increase in g, with little effect on μ_s. The clearing effect of glycerin appears to be due to a reduction in the angular deviation

of scattering (function of g), rather than a reduction in the frequency of scattering (function of μ_s). Simulations using Mie theory suggest that this increase in g with minor change in μ_s must involve an increase in the size of the scattering particles, which likely means a increase in the size of collagen fibers in dermis.

Chapter 8

Characterization of Osteogenesis Imperfecta with rCSLM

This chapter was co-authored by: Paul Campagnola and Steven L. Jacques. This chapter was published in 'Journal of Biomedical Optics' [5],

8.1 Introduction

There are many methods developed in the past few decades to determine optical properties of turbid media, like tissues, that depend on light diffusion. They include diffuse reflectance, diffuse transmission and reflectance as a function of source-detector distance [25, 29, 47]. These techniques can measure the absorption coefficient (μ_a) and the reduced scattering coefficient ($\mu_s' = \mu_s(1-g)$). But separating μ_s' into scattering coefficient (μ_s) and anisotropy of scattering (g) is difficult, unless a tissue sample is removed to allow other measurements, like collimated transmission or goniometry. Knowing both μ_s and g can characterize the ultrastructure of tissues that yields the scattering properties, i.e. the apparent particle size distribution like mitochondria, nuclei, lipid membranes, collagen, etc. More information from the μ_s and g of tissues may prove useful in monitoring the changes in ultrastructure due to different pathologies [22].

In this work a *reflectance-mode confocal scanning laser microscopy* (rCSLM)

was used to determine the optical properties of excised murine skin samples. Contrast in rCSLM is due to the scattering by the tissue ultrastructure, which enables non-invasive imaging of tissues without introducing external contrast agents. Collection of reflectance from the focus of a high-numerical-aperture lens is a function of the scattering properties of the tissue. The rCSLM provides a signature of the tissue scattering properties, which characterizes the ultrastructure. A simple analysis has being developed in our laboratory to extract optical properties (μ_s and g) from the confocal signal, $R(z)$, obtained as a function of the depth of the focus, z [82, 83].

Other groups have also studied the use of confocal reflectance, or optical coherence tomography (OCT) which is similar, as a function of the depth of the focus in order to determine scattering coefficient μ_s [22], and anisotropy g [17, 84]. However, these previous reports have not considered the contribution of photons that partially scatter but still reach the focus. This papers outlines the analysis that considers such photons when interpreting measurements to yield optical properties.

In this paper, optical measurements are used to sense a single gene defect by its effect on dermal scattering properties in a murine model. The mutation is a dominant negative gene defect that causes *Osteogenesis Imperfecta* (oim), also called brittle bone disease, which is caused by a defect in type I collagen structure and characterized by brittle bones prone to frequent fractures [17]. The gene defect also manifests as a change in dermal scattering, due to the failure of collagen fibrils to properly form and assemble into collagen fiber bundles. The structural consequences of this mutation have been studied using second harmonic generation imaging [85].

8.2 Methods

8.2.1 Animals

The optical study was conducted on murine skin samples from the University of Connecticut, where the mice carrying the *osteogenesis imperfecta* mutation were maintained in the B6C3Fe-a/a (C57BL/6JLe X C3HeB/FeJLe) hybrid background under approved animal care protocol. The animals were 3-4 months in age. Skin tissues were harvested from the thigh area immediately after euthanasia, then placed in saline and packed in ice for shipping. Samples were received at the Oregon Health & Science University within 24 hours and optical experiments were immediately conducted.

The three skin tissue samples were blindly labeled as #1, #2 and #3, and later revealed to be:

#1 = oim/oim (homozygous mutant)

#2 = oim/wt (heterozygous mutant)

#3 = wt/wt (wild type).

where 'oim' indicates *osteogenesis imperfecta mutation*. Histology of similar samples have been recently published, showing different fibrillar structure between the three skin types [85].

8.2.2 Experimental Protocol

The skin samples were placed epidermal surface down on a metal plate that was the size and shape of a standard microscope slide with a 2-mm diameter hole at its center. Tissues were coupled to the objective lens through this central hole by an aqueous saline solution. The microscope viewed the skin sample from below,

scanning from the epidermis up into the dermis. The z-axis stage stepped through 75 2-μm steps, and the x- and y-axis scanning mirrors captured a 512 x 512 pixel image at each depth of focus, at a 25 kHz pixel acquisition rate (a rather slow acquisition in this prototype system, requiring about 10 min to complete a 3D image). The x,y pixel size was 0.50 μm x 0.50 μm. Experiments were conducted at a room temperature of 22^oC.

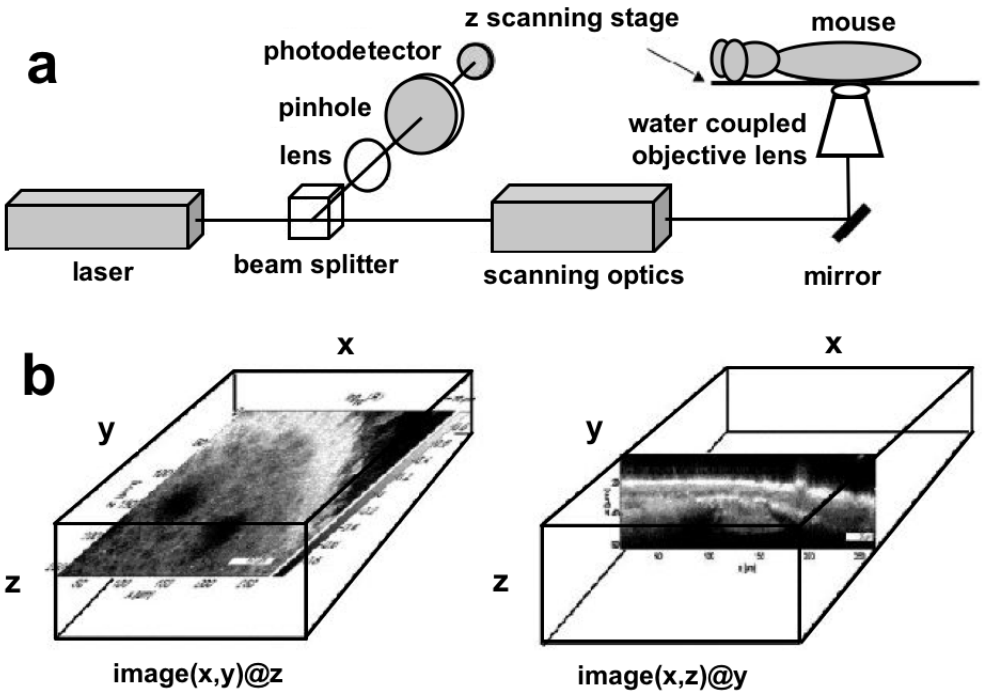

Figure 8.1: Experimental system, designed for *in vivo* imaging of mouse skin, was used to image *ex vivo* skin samples in this study. (a)The inverted microscope detects reflectance from the mouse. (b) 3D images are viewed en face as image(x,y)@z or transversely as image(x,z)@y.

8.2.3 Image Analysis

A 3D image data set, or image cube, was acquired for each of three sites on each of the two mutant samples, and on each of two sites for the wt/wt skin sample, for a total of eight image cubes. Data was recorded as $V(x, y, z)$ $[Volts]$ in the range

of 0 to 10 V. The pixel values for $V(z)$ were converted to reflectance units, $R(z)$ [dimensionless], by the expression:

$$R = \frac{R_{og}}{V_{og}} V \tag{8.1}$$

where V_{og} was the measurement of an oil-glass coverslip interface and R_{og} was the value $(\frac{n_1-n_2}{n_1+n_2})^2 = 4.056$ x 10^{-4}, where $n_1 = 1.46$ (oil) and $n_2 = 1.52$ (glass).

For each image cube, a set of 100 x 100 randomly chosen x,y locations were analyzed. About 60% of the locations were rejected for analysis because the skin surface was not centered within the z-axis field of view which jeopardized analysis, or there was a hair follicle or other surface abnormality. Typically about 4000 sites were found acceptable for analysis from each of the eight image cubes.

For each acceptable x,y location, the average of 100 $R(z)$ profiles over a 10 x 10 x,y pixel (5 μm x 5 μm) neighborhood centered around the x,y position of the chosen site was determined. The average $R(z)$ at each x,y position was analyzed within the combined epidermal and papillary dermis region and reticular dermal region of the skin, to specify the exponential decays in each region. The basic equation for decay was a simple exponential decay (Figure 8.2A) that was characterized by two parameters, ρ and μ, where ρ was the amplitude (called reflectivity) and μ was the exponential decay constant (called attenuation). Figure 8.2B show a typical average $R(z)$ profile. The analysis found the peak reflectance associated with the stratum corneum (sc) to identify the front surface, then moved 10 μm deeper to find the middle of the epidermis away from the strong influence of front surface. The papillary dermis began at 25 μm deeper than the front surface and the reticular dermis began 50 μm deeper than the front surface. The epidermis beyond 10 μm and the papillary dermis behaved similarly, and were quite variable. The typical value of attenuation μ was 100 cm^{-1}. The thickness

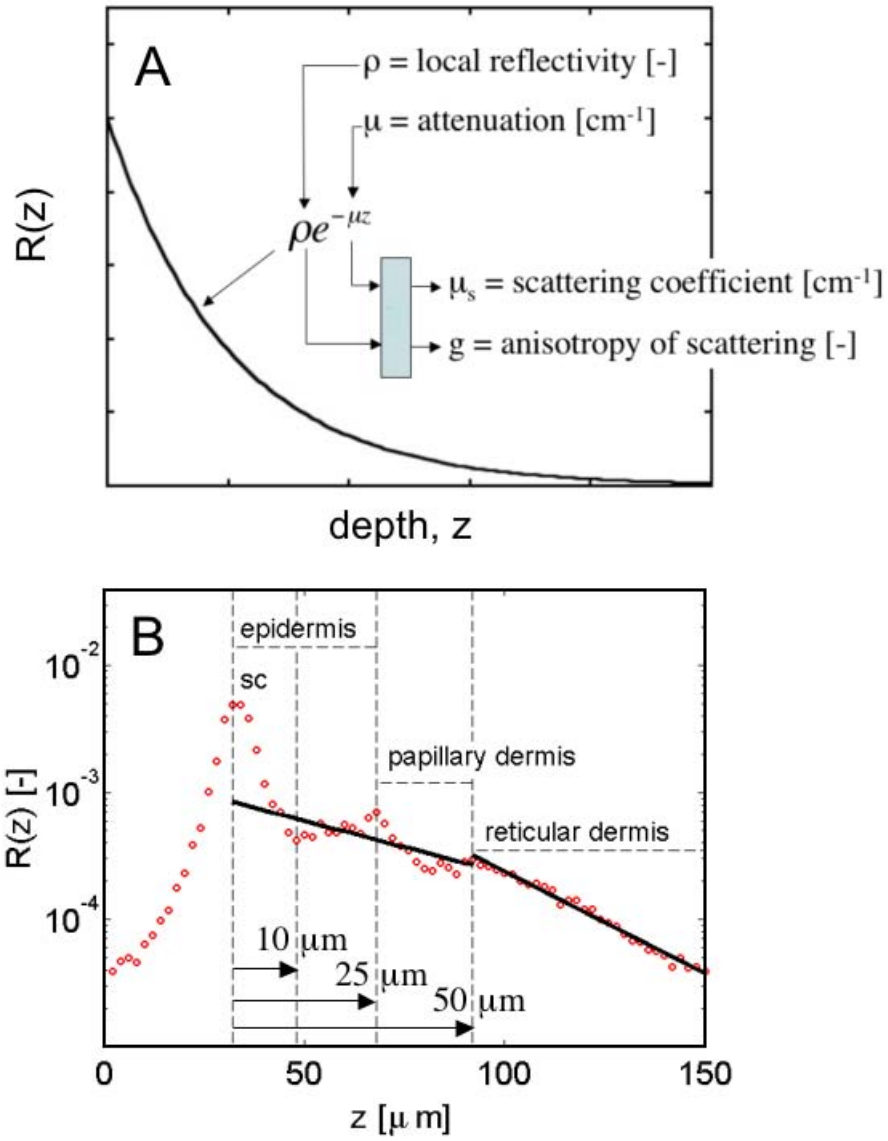

Figure 8.2: (A) As the focus of the microscope is scanned down into the tissue to a depth z, the reflected signal at the detector decays exponentially as $R(z) = \rho e^{-\mu z}$. The local reflectivity, ρ [dimensionless], and the attenuation, $\mu[cm^{-1}]$, are specified. (B) Typical axial profile $R(z)$ showing the regions associated with the stratum corneum (sc), the epidermis, the papillary dermis and the reticular dermis. The exponential decay in the reticular dermis, after correction for the average overlying attenuation of the epidermis and papillary dermis, yielded the ρ and μ of the reticular dermis, which are reported herein.

of the combined epidermis and papillary dermis was $L_{epi.pap} \approx 50\mu m$. Hence, the superficial attenuation by the combined epidermis and papillary dermis was

$T_{epi.pap} = e^{-\mu_{epi} L_{epi}} = e^{-(100cm^{-1})(0.0050cm)} = 0.61$. This paper reports the results of the reticular dermis, which provided less variable data and better analysis than the papillary dermis. The reticular μ and ρ were fit to the data at depths greater than 50 μm from the front surface, following the expression:

$$R(z) = T_{epi.pap}\, \rho\, e^{-\mu(z-z_o)} \tag{8.2}$$

where z_0 was the depth 50 μm from the front surface. The value of ρ was the reflectivity at $z = z_0$, based on fitting the data at $z > z_0$. The average value of $T_{epi.pap} = 0.61$ for all sites was used in the analysis, since attempting to use the local value of $T_{epi.pap}$ for each site introduced significant variability into the analysis. In summary, the ρ and μ for reticular dermis were determined after correcting for the average attenuation of overlying epidermis and papillary dermis.

8.2.4 Specifying Optical Properties

The optical properties were extracted from $R(z)$ by mapping the ρ and μ into the scattering coefficient (μ_s), and anisotropy of scattering (g), using the analysis described in chapter 3. Briefly the The value $\rho(\mu_s, g)$ is expressed as:

$$\rho\ = \mu_s\, \Delta z\, b(g, NA) \tag{8.3}$$

where $\Delta z = f\frac{1.4n\lambda}{NA^2}$ is the axial resolution of the confocal system from which light is backscattered to reach the detector through the pinhole. In these experiments, routine calibration was accomplished by imaging an oil-glass interface for use in equation 8.1. An alternative calibration used 0.1-μm-diameter polystyrene microspheres in a 2% agarose gel (150-μm thick, using glass coverslip as spacer). A collimated transmission measurement through the gel specified that μ_s equaled

96 cm^{-1}, which corresponded to a 0.034 volume fraction of microspheres if the microspheres behaved as predicted by Mie theory. Testing (not shown here) of sphere scattering versus sphere concentration confirmed that the spheres obeyed Mie theory at this concentration. The factor f was equal to 1.3, which allowed the μ_s and g predicted by Mie theory to match the experimental data. This need for a correction factor is attributed to the difficulties in using an oil-glass interface for calibration and/or to the possibility that the signal arises from a confocal volume whose axial extent exceeds the classical Δz. This issue is a topic of continued work, and only slightly affects the accuracy of the ρ values deduced in these experiments.

The scatter collection efficiency $b(g, NA)$ is the fraction of the scattered light that is backscattered within the collection solid angle of the objective lens and detected at the pinhole.

The attenuation μ is also a function of μ_s and g:

$$\mu = (\mu_s a(g) + \mu_a)2G \tag{8.4}$$

where scatter efficiency factor, $a(g)$, mitigates the effect of scattering to prevent transmission of photons to/from the focus; $a(g)$ depends on g and decreases to 0 as g approaches 1. The factor $2G(g, NA)$ multiplies the depth of focus, z_f [cm], to yield the round-trip photon pathlength in the tissue, in which G depends on the effective numerical aperture (NA_{eff}) of the objective lens as light enters the sample.

The value of μ_a for murine skin samples at a 488 nm wavelength was negligible; for example, a value of $\mu_a = 0.1cm^{-1}$ in the analysis yielded an attenuation of $e^{-(0.1cm^{-1})(0.0025cm)(2)(1.47)} = 0.9995$. Experiments on the system (not shown here) showed that the signal due to auto-fluorescence from the skin collected in the separate fluorescence channel at the spectral range of 500 - 610 nm is 3 orders of

magnitude less than the reflectance signal. Thus, the contribution of autofluorescence was not considered in the above analysis.

By using the above equations 8.3 and 8.4, the values of ρ and μ for different values of μ_s and g were calculated and plotted as a grid on the ρ versus μ graph (shown in figure 8.4). The experimentally determined data pair, ρ and μ, was also plotted and could be compared with the grid to specify the corresponding μ_s and g for each data pair. The magnitude of μ_s based on the confocal measurement of the spheres in gel matched the magnitude of μ_s specified by the separate collimated transmission measurement. In this manner, the method and analysis were calibrated.

8.3 Results

Figure 8.3a shows a typical image of a murine skin, portrayed as a cross-sectional view of $\log_{10}(R(z,x)@y)$ from the skin sample, a homozygous mutant. The various layers of the skin are labeled. The reflectance is plotted using a colorbar based on the $\log_{10}$(R). The water/stratum corneum interface shows brightly, the epidermis has a lower reflectance, and the dermis has a stronger reflectance than the epidermis. Between x = 150 and 200 μm, the edge of a hair follicle is seen, which disrupts the normal planar pattern of the skin. Figure 8.3b shows an en face image $\log_{10}[R(x,y,@z)]$, illustrating the change in collagen fibers bundles in the mutant.

Nine plots of ρ versus μ are shown in figure 8.4. Each column of three plots represents a different mouse skin sample except the upper plot in the first column, which shows the calibration and labels the $iso-\mu_s$ and $iso-g$ contours used in the figures. The first column shows the homozygous wildtype (wt/wt), the second column shows the heterozygous mutant (wt/oim), and the third column of the plots shows the homozygous mutant (oim/oim). Data are plotted as a grayscale encoded

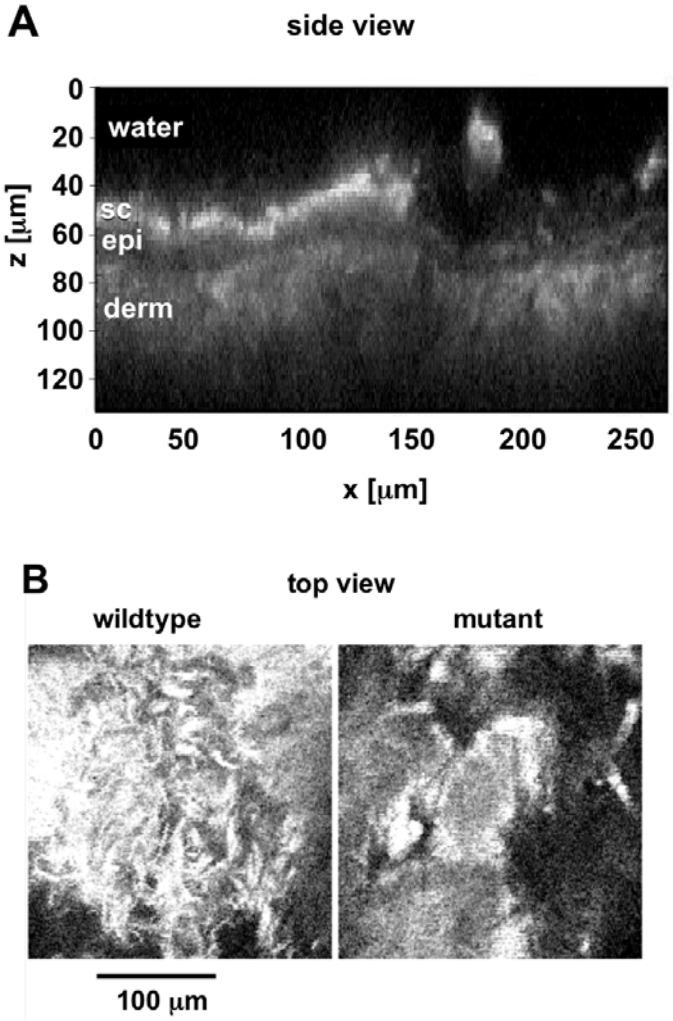

Figure 8.3: (A) Typical side view image of mouse skin (oim/oim mouse). The stratum corneum (sc), epidermis (epi) and dermis (derm) are distinguishable. The light is displayed as if incident from above through water, but experimentally the light was delivered from below. The epidermis scatters less than the water/sc boundary and the dermis. (B) Typical top view image of mouse skin, comparing a wild type (wt/wt) on the left and a mutant (oim/oim) on the right. The wildtype presents a fibrillar appearance due to well developed collagen fiber bundles, while the mutant presents a more homogeneous appearance. In both figures, the pixels display the logarithm of reflectance.

histogram on the grid. A dark color signifies a higher frequency of occurrence of a particular data pair. In columns 2 and 3, the mean value of the wildtype data is depicted as a circle for reference. The data lay approximately in the ranges

$50 < \mu_s < 125 cm^{-1}$ and 0.3 <g< 0.80. The variation in the data spreads in the plot as a coordinate increase in μ_s and decrease in g, which is considered in the discussion section. The value of g decreases with the presence of the *oim* mutation. The distribution of data points also seems to be narrower for the wildtype and broader for the mutant tissues. A subpopulation of values in one of the wildtype sites and several of the mutant sites, which is not yet understood.

The calibration plot (top left graph in figure 8.4) also plots the experimentally observed μ and ρ for polystyrene microspheres at 0.034 volume fraction (circle at $\mu_s = 93 cm^{-1}$, $g = 0.13$). The grid is aligned so that the prediction of Mie theory is aligned to exactly match this experimental measurement. As a test of the calibration, the μ_s specified by the collimated transmission measurement (square) is also shown. The circle within the square indicates that the collimated transmission measurement and the confocal measurement were in close agreement.

8.4 Discussion

An interesting feature of the experimental μ, ρ data in figure 8.4 is the characteristic spread of the data, in which the μ_s and g appear to vary in a coordinate manner. To clarify the nature of this variation, a simple exercise was conducted in which the analysis was applied to simulated data with added experimental variation. This exercise is shown in figure 8.5. Figure 8.5A shows a sampling of the wildtype and mutant data in the most dense portions of the histograms in figure 8.4, replotted as μ_s, g and $\mu_s(1-g)$, versus the reflectivity ρ. The values of μ_s and g for the wildtype were 74 cm^{-1} and 0.81, respectively. For the mutants, the values were 94 cm^{-1} and 0.46. As μ_s increased ρ increased. As g decreased and $(1-g)$ increased, ρ increased. As μ_s and $(1-g)$ increased—and therefore $\mu_s(1-g)$ increased—ρ increased. All these results were expected, but the coordinate variation in the x

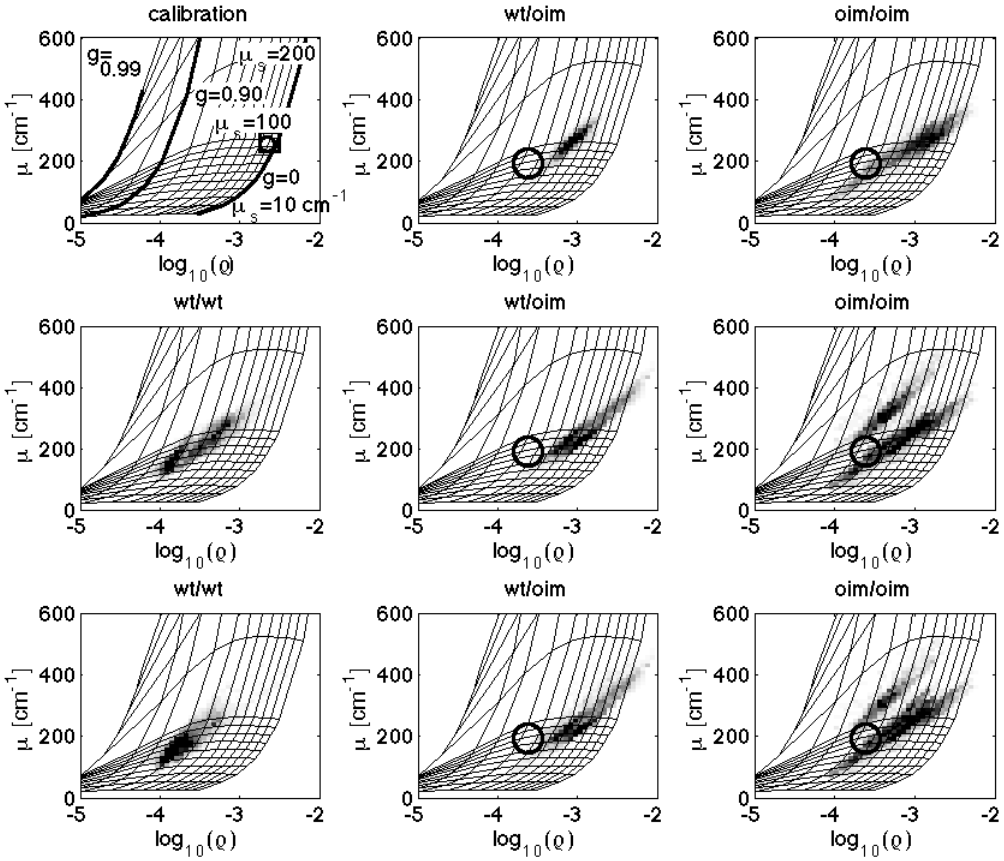

Figure 8.4: The plot of the experimentally determined μ and ρ data pairs superimposed on a grid of predicted values of μ and ρ for different values of μ_s and g. The distribution of data pairs for skin samples is represented by the grayscale 2-D histogram of μ versus ρ. The left panel shows the wild-type (wt/wt). The mean wildtype values are shown as circles in the center and right panels for reference. The center and right panels are the heterozygous mutants (wt/oim) and homozygous mutants (oim/oim), respectively. The data show a shift to the upper right towards lower g values and slightly higher μ_s values due to the mutation. The upper left panel shows the calibration and the labels for the other panels. The calibration using a confocal measurement of polystyrene microspheres (0.1-μm diameter, 0.034 volume fraction; solid circle) and a collimated transmission measurement (open square) are shown, and compare well. The grid is aligned with the confocal measurement of the microspheres.

and y values of these plots was also apparent. The central thick circles show the approximate peaks of the histograms for the wildtype and mutant. Figure 8.5B shows simulated data using the peak values of μ_s and g cited above for wildtype

and mutant. These μ_s and g values were used in equations 8.3 and 8.4 to yield μ and ρ, then used in equation 8.2 to yield $R(z)$. Then variation was added to $R(z)$, $R(z) \leftarrow exp(log(R(z)(1+err))$ where err = (2RND-1)x(0.40) and RND is a vector of random numbers between 0 and 1 such that each R(z) position received its own unique fluctuation. This procedure added ±40% variation to the simulated values of $log[R(z)]$. Such variation may simulate variation in the optical properties of the tissue or noise imposed by laser speckle. Finally, the $log[R(z)(1+err)]$ versus z was fit by a straight line with y-intercept $log(\rho)$ and slope $-\mu$. The resulting ρ and μ were converted to μ_s and g using the analysis grid shown in figure 8.4, and the values $\mu_s(1-g)$ were calculated. This procedure yielded figure 8.5B. The variation in the simulated results with added variation appeared similar to the variation seen in the experimental results. The source of variation is an ongoing topic of investigation.

From the data summarized in figure 8.5, the *oim* mutation appeared to decrease the anisotropy of scattering of the skin tissue, from 0.81 to 0.46, which corresponds to less forward-directed scattering, presumably due to the failure of fibrils to aggregate into fiber bundles as large as the wildtype. The smaller size scale of collagen fibers yielded more isotropic scattering. The scattering coefficient itself was only slightly increased by the mutation, from 74 to 94 cm^{-1}.

In summary, the rCSLM images allowed an assessment of the optical consequences of a single mutation that affected the collagen fibril assembly. The mutation caused a decrease in anisotropy g, with only a slight increase in the scattering coefficient μ_s. The distinct changes in μ_s and g could be separately determined. The behavior of an ensemble of local sites could be documented, and the statistical variation encountered could be considered.

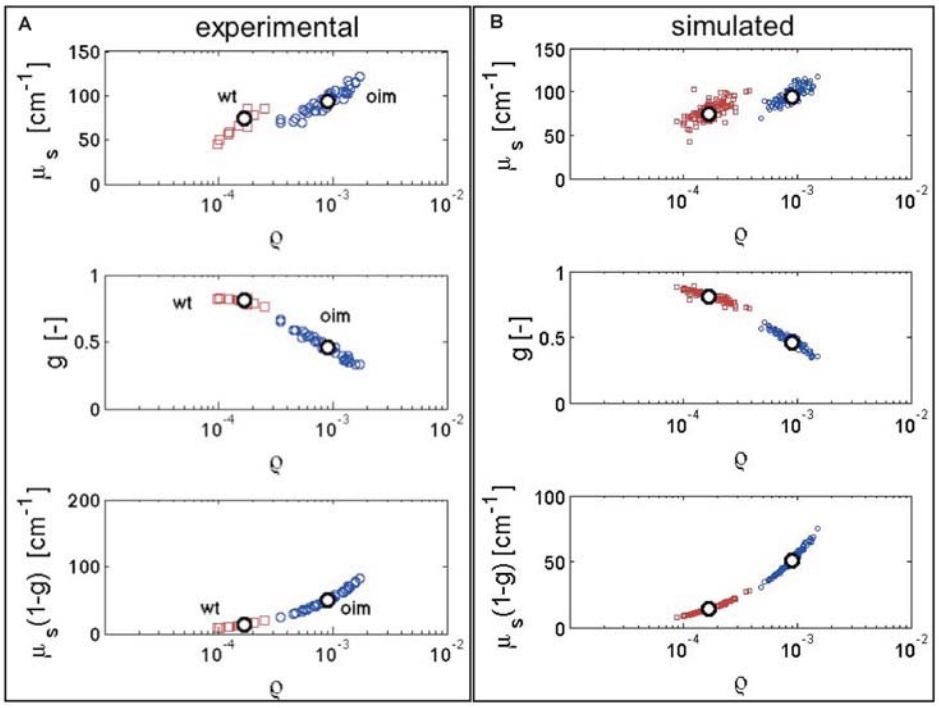

Figure 8.5: The effect of tissue variation on analysis. (A) Experimental data, showing the scattering coefficient, $\mu_s[cm^{-1}]$, anisotropy of scattering, g [dimensionless], and the reduced scattering coefficient, $\mu_s(1-g)[cm^{-1}]$, plotted versus the reflectivity ρ. The mutant (red squares) and oim data (blue circles) were sampled from figure 8.4. The central black circle in each data set is the approximate peak of distributed data. (B) Simulated data centered around the same peaks in the data but with random ± 40 % variation introduced into the function $\log[R(z)]$ prior to analysis, to simulate the fluctuation in optical density of the skin. The spread of the simulated and experimental data is similar, suggesting that the apparent coordinate variation in the μ and ρ data in figure 8.4 is the expected response to local fluctuations in the optical density of the tissue.

This work is preliminary in nature. These are our first studies with these wildtype and mutant skin samples. More work is needed before drawing firm conclusions about the effects of the mutant. However, this study illustrates the utility of the method and some of the considerations in applying the analysis.

Chapter 9

Conclusions

To date, confocal microscopy has been used primarily to generate three dimensional images of tissue in an effort to perform non-invasive histology [86–88]. This thesis couples the imaging capability of confocal microscopy with a light propagation model to quantify additional structural information about tissues. A method to measure optical properties from reflectance-mode confocal scanning laser microscopy (rCSLM) signals was developed in this thesis. The depth-dependent reflectance signal ($R(z)$) from rCSLM data was fit with a two parameter exponential function. The fit parameters describe the attenuation (μ) rate and the local reflectivity (ρ) of the rCSLM signal. The theoretical model described in this thesis maps the attenuation and reflectivity to optical properties of tissue: the scattering coefficient (μ_s) and the scattering anisotropy factor (g). This method was first validated on samples with known optical properties and then used to measure optical properties of tissues to follow structural changes induced by different biological mechanisms: 1.) the cataloging of optical properties of different murine organs, 2.) the use of optical clearing agents (OCA) to increase the transparency of tissues, and 3.) a gene mutation that alters collagen fiber bundle formation in murine models of *osteogenesis imperfecta*.

Optical properties measured by techniques that use diffusion theory to extract optical properties are used to determine the reduced scattering coefficient ($\mu_s\prime$) which is a lumped parameter of g and μ_s. The confocal optical geometry and the model presented in this thesis provides the unique opportunity to separately estimate μ_s and g. The signal in rCSLM is from single-scattered light, which depends on the magnitude of scattering (μ_s) and the directionality of scattering (g). As the directionality of scattering is lost in the diffusion regime, it is not possible to separate these two optical properties. The method was used with a custom built rCSLM system. However, this method can be implemented in any existing system without additional hardware provided the model parameters dependent on the system instrumentation are determined.

The theoretical model to specify optical properties of scattering from rCSLM presented in chapter 3 was validated on microsphere suspensions as presented in chapter 4. The volume fraction and size of the microspheres were adjusted to simulate the optical properties of tissues. The (μ, ρ) values extracted from the phantoms were mapped back to the optical properties determined by the combination of collimated transmission (to determine μ_s) and Mie theory (to determine g). The results show that the (μ, ρ) model was able to extract the correct values of g and μ_s in each phantom. There was a range of concentration values of the 0.1 μm sphere suspensions where the model predicted the optical properties within 5% error. The model under-estimated μ_s at lower concentrations and over-estimated at higher concentrations. The model estimated the changes in g due to the change in the diameter of the microspheres. The value of g estimated by the model was higher for larger diameter spheres, but the estimated values of μ_s were similar to collimated transmission measurement. The model was used to estimate the optical properties of the commercially available tissue phantoms: polyurethane phantoms (INO Biomimic$^{\text{TM}}$) and Spectralon$^{\text{TM}}$ reflectance standards described

in chapter 6. The phantoms were found to present background optical properties from the polyurethane matrix along with highly scattering TiO_2 particles. The Spectralon^{TM} phantoms were more dense in scattering, hence a higher μ_s than the polyurethane phantoms, and individual strongly scattering particles were present but less evident. Tissue simulating phantoms made from microsphere suspensions found to be best suited for calibration of confocal and OCT systems.

Optical properties of different murine tissues were measured by using rCSLM data and (μ, ρ) model. Freshly excised tissue was imaged by rCSLM and the depth-dependent signal was analyzed to extract optical properties. Five tissue types were measured: Brain white matter, brain gray matter, Liver, Muscle and Skin. The results show large variation due to the heterogeneity of the tissue ultrastructure. The variation for the Liver is low, as Liver a homogeneous tissue with hepatocytes. While the tissue with fibrillar (Muscle) and complex ultrastructure (Skin) more variation in the optical properties.

The effect of OCA in murine dermis was studied by applying the (μ, ρ) model. OCAs are chemical substances that make tissues appear semi-transparent. The optical model presented in this thesis was used to understand whether clearing was due to decrease in the scattering coefficient or the due to increase in scattering anisotropy. Our measurements revealed that glycerin significantly increased g of the dermis, with little change in μ_s which indicate that glycerin increases the size of the scattering constituents in the dermis probably by closely packing the collagen fibers together.

Lastly, the effect of a gene mutation on skin was investigated in a pilot study on the structural consequences of a genetic disorder called *osteogenesis imperfecta* (OI) that affects the ability of collagen fibrils to assemble into fiber bundles was studied. The effect of the gene mutation on the collagen matrix in mouse dermis was quantified by its effect on the optical properties. The scattering anisotropy

(g) decreased from 0.81 in wild type mice to 0.46 in mice with the mutation. The confocal based optical model provided a means to assess the structural changes in tissued due to pathological conditions non-invasively.

This thesis provides proof-of-principle that the optical properties of tissues can be quantified *in vivo*. The use of portable or fiber based confocal systems coupled with high speed data acquisition [66, 89, 90] would enable live imaging where optical properties of tissue can be measured and monitored under different physiological conditions.

The (μ, ρ) method provides a non-invasive technique to track structural changes in tissue *in vivo*. The changes can be tracked by monitoring the optical properties: μ_s and g or by monitoring the fitting parameters: μ and ρ. Levitz *et al.* [3, 23] used a similar model to non-destructively monitor the remodeling of collagen-gel by smooth muscle cells (SMCs) using OCT. The mechanism of gel compaction due to Matrix Metalloproteinases (MMPs) was quantitatively characterized by monitoring the scattering anisotropy (g). McLaughlin *et al.* [4] used the fitting parameter (μ, ρ) to improve contrast between malignant and healthy non-neoplastic tissue from OCT images.

Scattering of light by tissue is a function of ultra-structure of the tissue: size, shape and density of tissue scattering constituents like nuclei, mitochondria and structural proteins collagen, actin-myosin. Development of pathology in tissues is associated with structural changes that can be monitored non-invasively by tracking the changes in optical properties of tissue. Transition from dysplacia to carcinoma is associated with structural changes in the tissue that include: increased nucleus size, pleomorphism (changes in shape of nuclei), nuclear-to-cytoplasmic ratio, and decreased structural protein density. These changes alter the scattering properties of the tissue. Epithelial tissue scattering coefficients have been determined and used to differentiate normal versus cervical cancer tissue [22, 35]. The

technique described in this thesis may be applied to track the progression of cancer by non-invasive monitoring the structural changes through the contrast provided by optical properties as illustrated in OI study. This technique can be applied to study the effect of topical agents on epithelium, similar to OCA study. The structural changes in skin due to topical agents (like cosmetics that claim to alter collagen structure) can be characterized by *in vivo* monitoring of scattering properties of dermal collagen using rCSLM or OCT.

The method described to estimate optical properties from confocal signals does have its limitations. The theoretical model considers tissue as a collection of independent scatterers in a homogeneous matrix. The model ignores the structure factor of the tissues that accounts for interactions of scattered field by individual particles in a sample. In spite of this basic assumption, the optical properties of scattering can provide a fingerprint to the structure of the tissues (chapter 1). The model needed to account for the interference effects from scatterers at high concentration. An axial correction factor (f) was used to account for the difference in the theoretical axial resolution and the actual resolution of the rCSLM system used in the current work. Calibration measurements using microsphere tissue phantoms were used to determine f. Further studies are needed to account to determine the origins of this difference and address them.

Despite these limitations, the method described in this thesis can be used to estimate optical scattering properties of tissues. As scattering is dependent on the ultrastructure of the tissue, this technique provides can be used to non-invasively monitor changes in tissue structure. The method can be easily implemented on any reflectance confocal system available in the biomedical laboratories after calibrating for the instrument dependent parameters ($b(g, NA)$ and Δz).

References

[1] Daniel S Gareau. *In Vivo confocal microscopy in turbid media*. Ph.D Thesis, Oregon Health & Science University, Portland, OR, December 2006.

[2] Biomimic-optical phantoms. http://www.ino.ca/en-ca/achievements/description/project-p/optical-phantoms.html.

[3] David Levitz, Monica T. Hinds, Ardi Ardeshiri, Stephen R. Hanson, and Steven L. Jacques. Non-destructive label-free monitoring of collagen gel remodeling using optical coherence tomography. *Biomaterials*, 31(32):8210–8217, November 2010.

[4] Robert A. McLaughlin, Loretta Scolaro, Peter Robbins, Christobel Saunders, Steven L. Jacques, and David D. Sampson. Parametric imaging of cancer with optical coherence tomography. *Journal of Biomedical Optics*, 15(4):046029, 2010.

[5] Ravikant Samatham, Steven L. Jacques, and Paul Campagnola. Optical properties of mutant versus wild-type mouse skin measured by reflectance-mode confocal scanning laser microscopy (rCSLM). *Journal of Biomedical Optics*, 13(4):041309, 2008.

[6] Craig F. Bohren and Donald R. Huffman. *Absorption and Scattering of Light by Small Particles*. Publisher:Wiley-VCH, 1998.

[7] Xin Wang, Brian W. Pogue, Shudong Jiang, Xiaomei Song, Keith D. Paulsen, Christine Kogel, Steven P. Poplack, and Wendy A. Wells. Approximation of mie scattering parameters in near-infrared tomography of normal breast tissue in vivo. *Journal of Biomedical Optics*, 10(5):051704, 2005.

[8] D. Passos, J. C. Hebden, P. N. Pinto, and R. Guerra. Tissue phantom for optical diagnostics based on a suspension of microspheres with a fractal size distribution. *Journal of Biomedical Optics*, 10(6):064036, 2005.

[9] Steven L. Jacques. Fractal nature of light scattering in tissues. *Journal of Innovative Optical Health Sciences*, 04(01):1, 2011.

[10] Robert M. Pasternack, Jing-Yi Zheng, and Nada N. Boustany. Optical scatter changes at the onset of apoptosis are spatially associated with mitochondria. *Journal of Biomedical Optics*, 15(4):040504, 2010.

[11] Nada N. Boustany, Scot C. Kuo, and Nitish V. Thakor. Optical scatter imaging: subcellular morphometry in situ with Fourier filtering. *Optics Letters*, 26(14):1063–1065, July 2001.

[12] Jing-Yi Zheng, Robert M. Pasternack, and Nada N. Boustany. Optical scatter imaging with a digital micromirror device. *Optics Express*, 17(22):20401–20414, October 2009.

[13] M. Rajadhyaksha, R. G.B Langley, S. Gonzalez, M. White, J. M Zavislan, R. H Webb, and R. R Anderson. Clinical real-time confocal imaging of human skin and oral tissues in vivo. In *, IEEE Lasers and Electro-Optics Society Annual Meeting, 1997. LEOS '97 10th Annual Meeting. Conference Proceedings*, volume 1, pages 299–300 vol.1. IEEE, November 1997.

[14] Milind Rajadhyaksha, Melanie Grossman, Dina Esterowitz, Robert H. Webb,

and R. Rox Anderson. In vivo confocal scanning laser microscopy of human skin: Melanin provides strong contrast. *Journal of Investigative Dermatology*, 104(6):946–952, 1995.

[15] M Rajadhyaksha, S González, J M Zavislan, R R Anderson, and R H Webb. In vivo confocal scanning laser microscopy of human skin II: advances in instrumentation and comparison with histology. *The Journal of investigative dermatology*, 113(3):293–303, September 1999. PMID: 10469324.

[16] Daniel S Gareau, Glenn Merlino, Christopher Corless, Molly Kulesz-Martin, and Steven L Jacques. Noninvasive imaging of melanoma with reflectance mode confocal scanning laser microscopy in a murine model. *J Invest Dermatol*, 127(9):2184–2190, April 2007.

[17] Dirk Faber, Freek van der Meer, Maurice Aalders, and Ton van Leeuwen. Quantitative measurement of attenuation coefficients of weakly scattering media using optical coherence tomography. *Optics Express*, 12(19):4353–4365, 2004.

[18] L. T. Perelman, V. Backman, M. Wallace, G. Zonios, R. Manoharan, A. Nusrat, S. Shields, M. Seiler, C. Lima, T. Hamano, I. Itzkan, J. Van Dam, J. M. Crawford, and M. S. Feld. Observation of periodic fine structure in reflectance from biological tissue: A new technique for measuring nuclear size distribution. *Physical Review Letters*, 80(3):627, January 1998. Copyright (C) 2009 The American Physical Society; Please report any problems to prola@aps.org.

[19] Julia L Sandell and Timothy C Zhu. A review of in-vivo optical properties of human tissues and its impact on PDT. *Journal of Biophotonics*, 4(11-12):773–787, November 2011. PMID: 22167862.

[20] Robert J Hunter, Michael S Patterson, Thomas J Farrell, and Joseph E Hayward. Haemoglobin oxygenation of a two-layer tissue-simulating phantom from time-resolved reflectance: effect of top layer thickness. *Physics in Medicine and Biology*, 47(2):193, 2002.

[21] Andrew K. Dunn, Vincent P. Wallace, Mariah Coleno, Michael W. Berns, and Bruce J. Tromberg. Influence of optical properties on two-photon fluorescence imaging in turbid samples. *Applied Optics*, 39(7):1194–1201, March 2000.

[22] Tom Collier, Michele Follen, Anais Malpica, and Rebecca Richards-Kortum. Sources of scattering in cervical tissue: determination of the scattering coefficient by confocal microscopy. *Applied Optics*, 44(11):2072–2081, April 2005.

[23] David Levitz, Monica T Hinds, Niloy Choudhury, Noi T Tran, Stephen R Hanson, and Steven L Jacques. Quantitative characterization of developing collagen gels using optical coherence tomography. *Journal of Biomedical Optics*, 15(2):026019–026019–11, April 2010.

[24] Michael S. Patterson, B. Chance, and B. C. Wilson. Time resolved reflectance and transmittance for the non-invasive measurement of tissue optical properties. *Applied Optics*, 28(12):2331–2336, June 1989.

[25] B. C Wilson and S. L Jacques. Optical reflectance and transmittance of tissues: principles and applications. *IEEE Journal of Quantum Electronics*, 26(12):2186–2199, December 1990.

[26] T J Farrell, M S Patterson, and B Wilson. A diffusion theory model of spatially resolved, steady-state diffuse reflectance for the noninvasive determination of tissue optical properties in vivo. *Medical physics*, 19(4):879–888, August 1992. PMID: 1518476.

[27] Johannes Swartling, Jan S. Dam, and Stefan Andersson-Engels. Comparison of spatially and temporally resolved diffuse-reflectance measurement systems for determination of biomedical optical properties. *Applied Optics*, 42(22):4612–4620, 2003.

[28] Shao-Pow Lin, Lihong Wang, Steven L. Jacques, Frank K. Tittel, E. Sevick-Muraca, and Benaron. Measurement of absorption and scattering spectra with oblique incidence reflectometry. In *Biomedical Optical Spectroscopy and Diagnostics*, volume 3 of *OSA Trends in Optics and Photonics Series*, page AP1. Optical Society of America, March 1996.

[29] Shao-Pow Lin, Lihong Wang, Steven L. Jacques, and Frank K. Tittel. Measurement of tissue optical properties by the use of oblique-incidence optical fiber reflectometry. *Applied Optics*, 36(1):136–143, January 1997.

[30] George Zonios, Julie Bykowski, and Nikiforos Kollias. Skin melanin, hemoglobin, and light scattering properties can be quantitatively assessed in vivo using diffuse reflectance spectroscopy. *Journal of Investigative Dermatology*, 117(6):1452–1457, December 2001.

[31] Beop-Min Kim, Martin Ostermeyer, Steven L. Jacques, David A. Levy, Pradip Chakrabarti, Jorge H. Torres, Andrew C. von Eschenbach, Sohi Rastegar, Massoud Motamedi, E. Sevick-Muraca, and Benaron. In vivo optical property measurement using intraluminal fiber reflectometry: Optical properties of canine and human prostates. In *Biomedical Optical Spectroscopy and Diagnostics*, volume 3 of *OSA Trends in Optics and Photonics Series*, page AP3. Optical Society of America, March 1996.

[32] Steven L. Jacques. How tissue optics affect dosimetry of photodynamic therapy. *Journal of Biomedical Optics*, 15(5):051608–6, 2010.

[33] Judith R. Mourant, James P. Freyer, Andreas H. Hielscher, Angelia A. Eick, Dan Shen, and Tamara M. Johnson. Mechanisms of light scattering from biological cells relevant to noninvasive optical-tissue diagnostics. *Applied Optics*, 37(16):3586–3593, June 1998.

[34] Joseph M. Schmitt and Gitesh Kumar. Optical scattering properties of soft tissue: A discrete particle model. *Applied Optics*, 37(13):2788–2797, May 1998.

[35] T. Collier, D. Arifler, A. Malpica, M. Follen, and R. Richards-Kortum. Determination of epithelial tissue scattering coefficient using confocal microscopy. *IEEE Journal of Selected Topics in Quantum Electronics*, 9(2):307 – 313, April 2003.

[36] Ashley J. Welch and Martin J. C. van Gemert, editors. *Optical-Thermal Response of Laser-Irradiated Tissue*. Springer, 2nd ed. edition, February 2011.

[37] Michael Patterson, Brian Wilson, and Douglas Wyman. The propagation of optical radiation in tissue. II: optical properties of tissues and resulting fluence distributions. *Lasers in Medical Science*, 6(4):379–390, December 1991.

[38] Lihong V. Wang. Rapid modeling of diffuse reflectance of light in turbid slabs. *Journal of the Optical Society of America A*, 15(4):936–944, April 1998.

[39] Elena Salomatina, Brian Jiang, John Novak, and Anna N. Yaroslavsky. Optical properties of normal and cancerous human skin in the visible and near-infrared spectral range. *Journal of Biomedical Optics*, 11(6):064026, 2006.

[40] Steven L Jacques, C A Alter, and Scott A Prahl. Angular dependence of hene laser light scattering by human dermis. *Lasers in Life Sciences*, 1:309–334.

[41] Valery Tuchin. *Tissue Optics: Light Scattering Methods and Instruments for Medical Diagnosis, Second Edition*. SPIE Publications, 2nd edition, September 2007.

[42] Andrew Zardecki and Siegfried A. W. Gerstl. Multi-gaussian phase function model for off-axis laser beam scattering. *Applied Optics*, 26(15):3000–3004, August 1987.

[43] John W. Pickering, Scott A. Prahl, Niek van Wieringen, Johan F. Beek, Henricus J. C. M. Sterenborg, and Martin J. C. van Gemert. Double-integrating-sphere system for measuring the optical properties of tissue. *Applied Optics*, 32(4):399–410, February 1993.

[44] K. Giraev, N. Ashurbekov, and O. Kobzev. Optical characterization of biological tissues: determining absorption and scattering coefficients. *Technical Physics Letters*, 29(11):901–903, November 2003.

[45] Christian J. M. Moes, Martin J. C. van Gemert, Willem M. Star, Johannes P. A. Marijnissen, and Scott A. Prahl. Measurements and calculations of the energy fluence rate in a scattering and absorbing phantom at 633 nm. *Applied Optics*, 28(12):2292–2296, June 1989.

[46] Scott A. Prahl, Martin J. C. van Gemert, and Ashley J. Welch. Determining the optical properties of turbid media by using the adding-doubling method. *Applied Optics*, 32(4):559–568, February 1993.

[47] W. F Cheong, S. A Prahl, and A. J Welch. A review of the optical properties of biological tissues. *IEEE Journal of Quantum Electronics*, 26(12):2166–2185, December 1990.

[48] Valery V. Tuchin, Irina L. Maksimova, Dmitry A. Zimnyakov, Irina L. Kon,

Albert K. Mavlutov, and Alexey A. Mishin. Light propagation in tissues with controlled optical properties. In David A. Benaron, Britton Chance, and Gerhard J. Mueller, editors, *Photon Propagation in Tissues II*, volume 2925, pages 118–142, Vienna, Austria, December 1996. SPIE.

[49] Laurel R. Jones and Steven L. Jacques. Comparing 2-d screen projections to 1-d goniometric measurements in scattering studies of surface roughness. *Proceedings of SPIE*, 7175(1):71750E–71750E–9, February 2009.

[50] M. Minsky. Memoir on inventing the confocal scanning microscope. *Scanning*, 10(4):128–138, 1988.

[51] James Pawley, editor. *Handbook of Biological Confocal Microscopy*. Springer, 2nd edition, March 1995.

[52] Stephen W. Paddock. *Confocal Microscopy Methods and Protocols*. 1999.

[53] P. Corcuff, G. Gonnord, G. E. Pierard, and J. L. Leveque. In vivo confocal microscopy of human skin: A new design for cosmetology and dermatology. *Scanning*, 18(5):351–355, 1996.

[54] Salvador González, Milind Rajadhyaksha, and R. Rox Anderson. Non-invasive (Real-Time) imaging of histologic margin of a proliferative skin lesion in vivo. *Journal of Investigative Dermatology*, 111(3):538–539, 1998.

[55] Hester K Busam KJ. Detection of clinically amelanotic malignant melanoma and assessmentof its margins by in vivo confocal scanning laser microscopy. *Archives of Dermatology*, 137(7):923–929, July 2001.

[56] B Selkin, M Rajadhyaksha, S Gonzalez, and R G Langley. In vivo confocal microscopy in dermatology. *Dermatologic clinics*, 19(2):369–377, ix–x, April 2001. PMID: 11556245.

[57] Lucinda D. Swindle, Steven G. Thomas, Michael Freeman, and Peter M. Delaney. View of normal human skin in vivo as observed using fluorescent fiber-optic confocal microscopic imaging. *Journal of Investigative Dermatology*, 121(4):706–712, 2003.

[58] H D Cavanagh, W M Petroll, and J V Jester. The application of confocal microscopy to the study of living systems. *Neuroscience and biobehavioral reviews*, 17(4):483–498, 1993. PMID: 8309657.

[59] James V. Jester, Peter M. Andrews, W. Matthew Petroll, Michael A. Lemp, and H. Dwight Cavanagh. In vivo, real-time confocal imaging. *Journal of Electron Microscopy Technique*, 18(1):50–60, 1991.

[60] David M. Maurice. A scanning slit optical microscope. *Investigative Ophthalmology & Visual Science*, 13(12):1033–1037, December 1974.

[61] Gordon S. Kino and Timothy R. Corle. *Confocal Scanning Optical Microscopy and Related Imaging Systems*. Academic Press, August 1996.

[62] Colin L. Smithpeter, Andrew K. Dunn, A. J. Welch, and Rebecca Richards-Kortum. Penetration depth limits of in vivo confocal reflectance imaging. *Applied Optics*, 37(13):2749–2754, May 1998.

[63] Joseph A. Izatt, Michael R. Hee, Gabrielle M. Owen, Eric A. Swanson, and James G. Fujimoto. Optical coherence microscopy in scattering media. *Optics Letters*, 19(8):590–592, April 1994.

[64] D.R. Chou and A.P. Wax. Optical scattering of confocal laser scanning reflectance microscopy in turbid media. In *Conference on Lasers and Electro-Optics, 2005. (CLEO)*, volume 3, pages 1578 – 1580 Vol. 3, May 2005.

[65] Frederic Truffer. Determining optical properties with confocal microscopy in reflection and transmission mode. Master's thesis, Hochschule Ravensburg-Weingarten, Switzerland, 2008.

[66] Milind Rajadhyaksha, R. Rox Anderson, and Robert H. Webb. Video-rate confocal scanning laser microscope for imaging human tissues in vivo. *Applied Optics*, 38(10):2105–2115, April 1999.

[67] Brian W. Pogue and Michael S. Patterson. Review of tissue simulating phantoms for optical spectroscopy, imaging and dosimetry. *Journal of Biomedical Optics*, 11:041102, 2006.

[68] Mie scattering calculator. http://omlc.ogi.edu/calc/mie_calc.html.

[69] Yongji Fu. *Using optical methods to monitor and administer photodynamic therapy to oral bacteria*. Ph.D Thesis, Oregon Health & Science University, Portland, OR, March 2008.

[70] Steven L. Jacques, Bo Wang, and Ravikant Samatham. Reflectance confocal microscopy of optical phantoms. *Biomedical Optics Express*, 3(6):1162–1172, June 2012.

[71] Steven L. Jacques, David Levitz, Ravikant Samatham, Dan S. Gareau, Niloy Choudhury, and Frederic Truffer. Light scattering in confocal reflectance microscopy. In Adam Wax and Vadim Backman, editors, *Biomedical Applications of Light Scattering*, pages 171–190. McGraw Hill, 2005.

[72] Ravikant Samatham, Kevin G. Phillips, and Steven L. Jacques. Assessment of optical clearing agents using reflectance-mode confocal scanning laser microscopy. *Journal of Innovative Optical Health Sciences*, 03(03):183, 2010.

[73] Loretta Scolaro, Robert A. McLaughlin, Blake R. Klyen, Benjamin A. Wood, Peter D. Robbins, Christobel M. Saunders, Steven L. Jacques, and David D. Sampson. Parametric imaging of the local attenuation coefficient in human axillary lymph nodes assessed using optical coherence tomography. *Biomedical Optics Express*, 3(2):366–379, February 2012.

[74] Ravikant Samatham, David Levitz, Reid Fletcher, Yongji Fu, and Steven L. Jacques. Microscopic heterogeneity vs. macroscopic homogeneity in tissue phantoms using reflectance-mode confocal scanning laser microscopy. In *Proceedings of SPIE*, pages 68700H–68700H–7, San Jose, CA, USA, 2008.

[75] Theodore Moffitt, Yin-Chu Chen, and Scott A. Prahl. Preparation and characterization of polyurethane optical phantoms. *Journal of Biomedical Optics*, 11(4):041103, 2006.

[76] Kevin G. Phillips, Ravikant Samatham, Niloy Choudhury, James C. Gladish, Philippe Thuillier, and Steven L. Jacques. In vivo measurement of epidermal thickness changes associated with tumor promotion in murine models. *Journal of Biomedical Optics*, 15(4):041514, 2010.

[77] Ruikang K. Wang, Xiangqun Xu, Valery V. Tuchin, and James B. Elder. Concurrent enhancement of imaging depth and contrast for optical coherence tomography by hyperosmotic agents. *Journal of the Optical Society of America B*, 18(7):948–953, July 2001.

[78] Stacy R. Millon, Katherine M. Roldan-Perez, Kristin M. Riching, Gregory M. Palmer, and Nirmala Ramanujam. Effect of optical clearing agents on the in vivo optical properties of squamous epithelial tissue. *Lasers in Surgery and Medicine*, 38(10):920–927, 2006.

[79] R. G. LeBel and D. A. I. Goring. Density, viscosity, refractive index, and hygroscopicity of mixtures of water and dimethyl sulfoxide. *Journal of Chemical & Engineering Data*, 7(1):100–101, January 1962.

[80] List of refractive indices - wikipedia, the free encyclopedia. http://en.wikipedia.org/wiki/List_of_refractive_indices.

[81] X. Wen, Z. Maoy, Z. Han, V.V. Tuchin, and D. Zhu. In vivo skin optical clearing by glycerol solutions: Mechanism. *Journal of Biophotonics*, 3(1-2):44–52, 2010.

[82] S. Jacques, R. Samatham, N. Choudhury, and D. S. Gareau. Specifying tissue optical properties using axial dependence of confocal reflectance images: confocal scanning laser microscopy and optical coherence tomography. In *Proceedings of SPIE*, pages 64460N–64460N–5, San Jose, CA, USA, 2007.

[83] Steven L. Jacques, Ravikant Samatham, Niloy Choudhury, Yongji Fu, and David Levitz. Measuring tissue optical properties in vivo using reflectance-mode confocal microscopy and OCT. In *Proceedings of SPIE*, pages 68640B–68640B–8, San Jose, CA, USA, 2008.

[84] Antonella Forlino and Joan C. Marini. Osteogenesis imperfecta: Prospects for molecular therapeutics. *Molecular Genetics and Metabolism*, 71(1-2):225–232, September 2000.

[85] Oleg Nadiarnykh, Sergey Plotnikov, William A. Mohler, Ivo Kalajzic, Deborah Redford-Badwal, and Paul J. Campagnola. Second harmonic generation imaging microscopy studies of osteogenesis imperfecta. *Journal of Biomedical Optics*, 12:051805, 2007.

[86] Yogesh G. Patel, Kishwer S. Nehal, Iana Aranda, Yongbiao Li, Allan C.

Halpern, and Milind Rajadhyaksha. Confocal reflectance mosaicing of basal cell carcinomas in mohs surgical skin excisions. *Journal of Biomedical Optics*, 12(3):034027–10, May 2007.

[87] Daniel S. Gareau, Yongbiao Li, Billy Huang, Zach Eastman, Kishwer S. Nehal, and Milind Rajadhyaksha. Confocal mosaicing microscopy in mohs skin excisions: feasibility of rapid surgical pathology. *Journal of Biomedical Optics*, 13(5):054001–12, 2008.

[88] Daniel S. Gareau. Feasibility of digitally stained multimodal confocal mosaics to simulate histopathology. *Journal of Biomedical Optics*, 14(3):034050–5, May 2009.

[89] Ralf Wolleschensky, Bernhard Zimmermann, and Michael Kempe. High-speed confocal fluorescence imaging with a novel line scanning microscope. *Journal of Biomedical Optics*, 11(6):064011, 2006.

[90] Peter J. Dwyer, Charles A. DiMarzio, James M. Zavislan, William J. Fox, and Milind Rajadhyaksha. Confocal reflectance theta line scanning microscope for imaging human skin in vivo. *Optics Letters*, 31(7):942–944, April 2006.